9-2010

Characterization and Interactions of Ultrafast Surface Plasmon Pulses

Sibel Ebru Yalcin
University of Massachusetts Amherst, syalcin@physics.umass.edu

CHARACTERIZATION AND INTERACTIONS OF ULTRAFAST SURFACE PLASMON PULSES

A Dissertation Presented

by

SIBEL EBRU YALCIN

Submitted to the Graduate School of the
University of Massachusetts Amherst in partial fulfillment
of the requirements for the degree of

DOCTOR OF PHILOSOPHY

September 2010

Department of Physics

CHARACTERIZATION AND INTERACTIONS OF ULTRAFAST SURFACE PLASMON PULSES

A Dissertation Presented

by

SIBEL EBRU YALCIN

Approved as to style and content by:

_____
Marc Achermann, Chair

_____
Mark Tuominen, Member

_____
Lori S. Goldner, Member

_____
Michael Barnes, Member

_____
Donald Candela, Department Head,
Department of Physics

ACKNOWLEDGMENTS

Ph.D is a long marathon and I am happy that I was not alone. I would like to thank to everybody who supported me and stayed with me all the time.

First and foremost, I would like to thank my advisor Prof. Marc Achermann for his constant support and motivation during my Ph.D. education. The weekly discussions in the group meetings were the most valuable moments for me. I have learned four important things during my Ph.D:

1. Thinking hard before starting any action.
2. Doing literature search regularly.
3. Planning the experiment.
4. Analyzing the data.

I would like to thank my advisor Prof. Marc Achermann because of involving me such a distinguished project “building and operating heterodyne femtosecond photon scanning tunneling microscope (fsPSTM)”. This project made me realize that how much fun is actually working with a near-field optical microscope. I learned and experienced all the challenges in this work.

Secondly, I have special thanks our exchange student Kristina Meyer who made a significant contribution in the setting-up of the optical part of heterodyne fsPSTM and our undergraduate student Daniel Brosnan who involved in the building and software development part of the fsPSTM. I also would like to thank our undergraduate student David Oullette because of staying with me patiently during our troubleshooting period. Moreover, I am thankful to Taylor Esformes who took the SEM pictures of our near-field probe.

In addition, I would like to thank Prof. Niek Van Hulst and L. Kobus Kuipers because of their motivating comments about my research. I had a chance to meet with these two giant scientists in Gordon Plasmonics Conference, Waterville, 2010. It was the most amazing moment for me. Considering that they are the most established groups in heterodyne PSTM, their comments were very much valuable to me.

I also would like to thank Prof. Mark Tuominen and his student Huajie Ke because of fabricating SPP waveguide structures for near-field characterization. Prof. Thomas Russell and Soojin Park from Polymer Science and Engineering Department prepared hybrid gold NP/silver thin film structures using block-copolymer based self-assembly techniques. We are very much thankful to them. I also would like to thank Prof. Adrian Parsegian and Prof. Robert Krotkov because of their nice comments and their strong support on my research.

I am so much thankful to Prof. Mark Tuominen, Prof. Lori Goldner and Prof. Michael Barnes for being in my dissertation committee. I have special thanks for Prof. Lori Goldner because of supporting and motivating me all the time. Her expertise in near-field imaging is world known. Having her in my committee was a great pleasure and honor for me. The discussions that I have done with Prof. Lorenzo Sorbo helped me to pass my qualify exam. I am so much thankful to him because of giving me his valuable time.

I have shared incredible moments with my lab partners Yikuan Wang, Yanzhen Wang, Peter Mistark, Mahshid Pourmand, Mina Baghgar, Robert Boge and Boqian Yang. I thank them a lot and wish all the best for their future careers.

My master advisor, Prof. Levent Kurnaz from Bogazici University, supported and motivated me all the time. I am so much thankful to him all my life. I also would like to thank Prof. Salih Karaali from University of Istanbul who stimulated me to be a scientist.

In the end, I have special thanks to my friends Nikhil S. Malvankar and Ekundayo (Dayo) Shittu for being with me, supporting me and understanding me all the time. I hope all the best for their future careers. I am immensely thankful to my parents Husniye Yalcin and Omer Atilla Yalcin for supporting me all the time and giving me chance to go abroad to do Ph.D in physics. Of course, I didn't forget my smart engineer and sweet twin brother Sinan Eren Yalcin in my acknowledgment list. We came to the world together; we shared all the special moments together. I thank him so much because of being with me all the time. I wish him all the best and success for future.

ABSTRACT

CHARACTERIZATION AND INTERACTIONS OF ULTRAFAST SURFACE PLASMON PULSES

SEPTEMBER 2010

SIBEL EBRU YALCIN, B.S., UNIVERSITY OF ISTANBUL, TURKEY

M.S., BOGAZICI UNIVERSITY, ISTANBUL, TURKEY

Ph.D., UNIVERSITY OF MASSACHUSETTS AMHERST

Directed by: Professor Marc Achermann

Surface Plasmon Polaritons (SPPs) are considered to be attractive components for plasmonics and nanophotonic devices due to their sensitivity to interface changes, and their ability to guide and confine light beyond the diffraction limit. They have been utilized in SPP resonance sensors and near field imaging techniques and, more recently, SPP experiments to monitor and control ultrafast charge carrier and energy relaxation dynamics in thin films.

In this thesis, we discuss excitation and propagation properties of ultrafast SPPs on thin extended metal films and SPP waveguide structures. In addition, localized and propagating surface plasmon interactions in functional plasmonic nanostructures will also be addressed.

For the excitation studies of ultrafast SPPs, we have done detailed analysis of femtosecond surface plasmon pulse generation under resonant excitation condition using prism coupling technique. Our results show that photon-SPP coupling is a resonant process with a finite spectral bandwidth that causes spectral phase shift and narrowing of the SPP pulse spectrum. Both

effects result in temporal pulse broadening and, therefore, set a lower limit on the duration of ultrafast SPP pulses. These findings are necessary for the successful integration of plasmonic components into high-speed SPP circuits and time-resolved SPP sensors.

To demonstrate interactions between localized and propagating surface plasmons, we used block-copolymer based self assembly techniques to deposit long range ordered gold nanoparticle arrays onto silver thin films to fabricate composite nanoparticle thin film structures. We demonstrate that these gold nanoparticle arrays interact with SPPs that propagate at the film/nanoparticle interface and therefore, modify the dispersion relation of SPPs and lead to strong field localizations. These results are important and advantageous for plasmonic device applications.

For the propagation studies of ultrafast SPPs, we have designed and constructed a home-built femtosecond photon scanning tunneling microscope (fsPSTM) to visualize ultrafast SPPs in photonic devices based on metal nanostructures. Temporal and phase information have been obtained by incorporating the fsPSTM into one arm of a Mach-Zehnder interferometer, allowing heterodyne detection. Understanding plasmon propagation in metal nanostructures is a requirement for implementing such structures into opto-electronic and telecommunication technologies.

TABLE OF CONTENTS

Page

LIST OF FIGURES

CHAPTER 1

NANO-PHOTONICS

1.1 Introduction

The important milestone in the development of modern optical science and technology was the invention of the laser in 1960s. Lasers took important place in optoelectronics and fiber communication technologies because of their amplitude, phase, frequency and polarization tunability. On the other hand, crucial technological areas started to approach their fundamental physical limits. For a better integration it was advantageous to replace the electronic applications with much smaller nanometer (nm)-sized materials for future advanced photonic device applications. However, the size of these devices cannot be reduced beyond the diffraction limit as long as propagating light is used for their operation. Scientists had to go beyond the diffraction limit of light to open up a new field of optical science and technology. This field is called Nanophotonics or Nano-optics (*3*).

Nanophotonics is a research dedicated to study the light-matter interactions in nanometer scale where the physical, chemical or structural behavior of natural or artificial nanostructured matter controls the interactions (*4*). One of the sub-division of nanophotonics is mostly interested in light-metal interactions. This research field is called plasmonics, in which the manipulation of light at the nanoscale is studied by using the properties of surface plasmons arising from metal free-electron response. Several current technological

challenges may be overcome by utilizing the unique properties of surface plasmons (*5*).

1.2 Background

In general, collective free electron oscillations in metals are referred to as plasmons. In bulk metal, plasmons only exist as longitudinal waves and, therefore, cannot be directly excited by transverse optical waves (*6*). Solving Maxwell's equation for metal surface under appropriate boundary conditions reveals a solution, the surface plasmon polariton (SPP) that has both longitudinal and transverse components and propagates along the metal surface [Fig. 1.1 (a)] (*7*). That's why SPPs are also known as propagating surface plasmons. The z dependence of the field perpendicular to the interface is evanescent and decays exponentially with distance from the surface, demonstrating the bound, non-radiative nature of SPs (*8*). The decay length of the field into dielectric and metal are respectively δ_d and δ_m shown in Fig. 1.1 (b). (See eqns. 1a and 1b).

The decay rates are defined:

$$1/\delta_d = \frac{\omega}{c}\sqrt{-\frac{\varepsilon_d{}^2}{\varepsilon_d + \varepsilon_m}} \quad (1a) \quad \text{and} \quad 1/\delta_m = \frac{\omega}{c}\sqrt{-\frac{\varepsilon_m{}^2}{\varepsilon_d + \varepsilon_m}} \quad (1b)$$

Where ω is the frequency of light, c is the speed of light of $3\text{x}10^8$ m/sec; ε_m and ε_d are the dielectric functions of metal and dielectric.

These fields only extend a few 100 nm from the surface; therefore light can be confined beyond the diffraction limit.

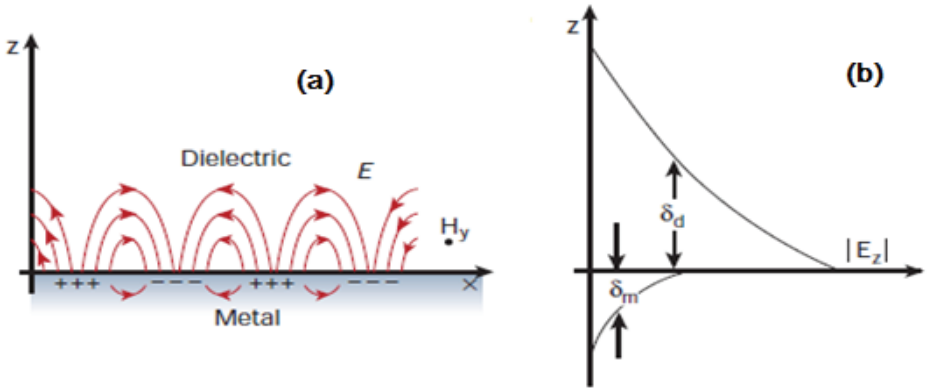

Figure 1.1: (a) SPs at the interface of a metal and a dielectric material. **(b)** Evanescent field in the z direction (*8*).

There is another kind of surface plasmon resonance known as localized surface plasmons (LSPs) in which charge density oscillations are confined to metallic nanostructures. Under resonant excitation conditions, SPs can strongly enhance electromagnetic fields. Such a field is very local, with a spatial extension on the order of the nanostructure curvature which gives the system ability to confine light beyond the diffraction limit (*8, 9*). This special confinement capability makes metallic nanostructures promising candidates for use in subwavelength photonic circuits (*10-14*) sensors (*15-17*), high-resolution microscopy (*18-22*), and bio-photonics (*15, 23-26*).

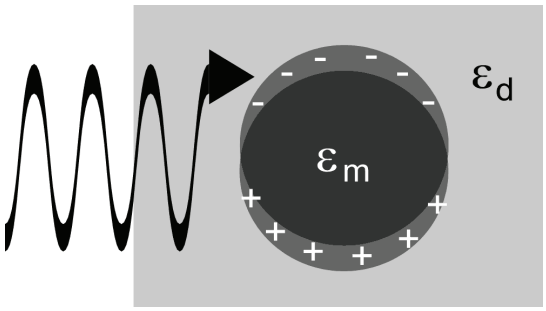

Figure 1.2: Free electron oscillation in a metallic nanoparticle embedded in a dielectric matrix excited through an external electro-magnetic wave (Image credit Marc Achermann).

1.3 Summary

In conclusion, SP resonances give us ability to generate strong and very well confined light fields to be functional in many nanophotonic and plasmonics applications.

CHAPTER 2

EXCITATION PROPERTIES OF ULTRAFAST SURFACE PLASMON PULSES USING PRISM COUPLING TECHNIQUE

We have done detailed analysis of femtosecond SPP pulse generation under resonant excitation condition (*27*). Using prism coupling technique we excite femtosecond SPP pulses at a gold/air interface with ultrafast laser pulses. We show that the photon-SPP coupling is a resonant process with a finite spectral bandwidth that causes a spectral phase shift and a narrowing of the SPP pulse spectrum. Both effects result in a temporal broadening and, therefore, set a lower limit on the duration of ultrafast SPP pulses with consequences for ultrafast SPP applications.

2.1 Coupling Light Waves to Surface Plasmons

The SPP is an electromagnetic wave that is bound to a metal/dielectric interface by coupling to the free electrons of the metal. Considering the simplest case of an SPP that propagates at a metal/dielectric interface with dielectric functions ε_m and ε_d, respectively, Maxwell's equations yield the SPP dispersion relation (*8*).

$$k_{SPP} = k_0 \sqrt{\frac{\varepsilon_d \varepsilon_m}{\varepsilon_d + \varepsilon_m}} \quad (2)$$

in which k_{SPP} and k_0 are the SPP and the free-space wave vectors, respectively. Equation (2) tells us that SPP wave vector k_{SPP} is larger than the wave vector in the dielectric medium. This has both advantageous and disadvantageous results.

Since the large k_{SPP} gives better confinement to the interface, it is very advantageous for new types of plasmonic circuits (*28*). The downside of the large k_{SPP} is that SPP excitation directly from the dielectric side of the interface is prohibited through momentum conservation. One way to compensate this momentum mismatch is using the most simple and widely known Kretschmann prism coupling technique to enhance the momentum of light (*29*). In this technique SPP excitation is achieved by sending p-polarized light through a high refractive index prism on the back side of a thin metal film and exciting the SPPs on the front side of the metal film, which faces a lower refractive index medium (Fig. 2.3). SPP excitation is a resonant process and occurs when the in-plane wave vector of the incident light within the prism matches k_{SPP} (Fig. 2.1).

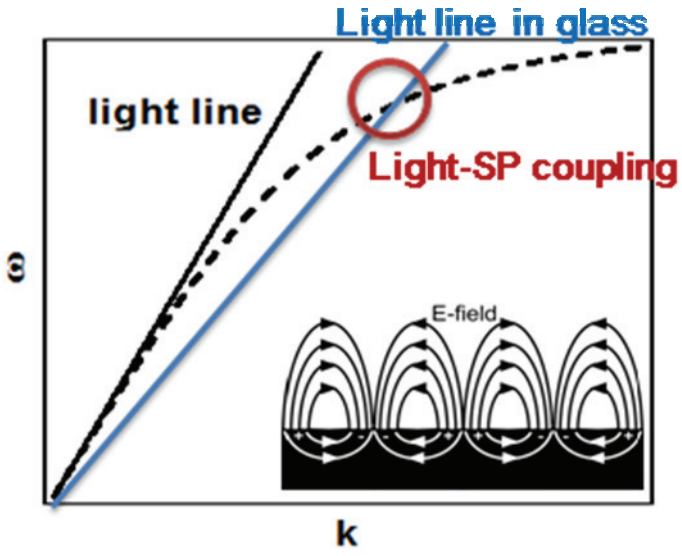

Figure 2.1: Dispersion relation of free propagating light (black line), and SPP (dashed curve) shows the momentum mismatch. Light-SPP coupling is possible by sending the light through a glass prism (blue line).

2.2 Ultrafast SPP Excitation Using Ultrafast Lasers

Ultrafast Surface Plasmon Pulse generation is achieved by using mode-locked ultrafast Ti:Sapphire pulsed oscillators. In general, pulsed lasers produces laser pulses with repetition rate. The lower the repetition rate the higher the pulse energy. Ti:Sapphire pulsed lasers have sub 25 fs pulse durations with 90 MHz repetition rates [Fig. 2.2 (a)]. Their peak power is more than 100 kW. The laser spectrum has tunability from 750 nm to 900 nm. The p-polarized laser pulses are close to bandwidth limited with a spectral full width at half maximum (FWHM) of 56 nm, centered about 820 nm [Fig. 2.2 (b)].

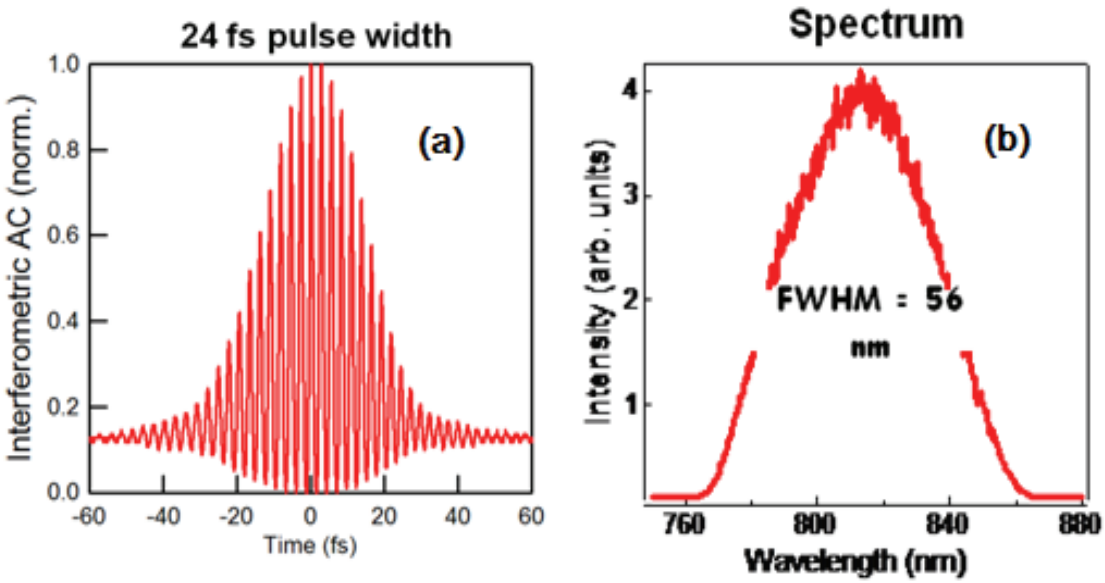

Figure 2.2: (a) Sub 25 fs pulse duration of ultrafast Ti:Sapphire laser. **(b)** Spectrum of a pulse has tunability from 750 to 900 nm.

2.3 The Effects of Resonantly Excited Ultrafast Surface Plasmon Pulses

2.3.1 Incomplete Coupling

We excite ultrafast SPP pulses by focusing ultrafast laser pulses on an appropriate metal film thickness (typically ~ 50 nm for gold and silver films in the visible and near-infrared wavelength range) by using prism coupling (see Fig. 2.3). The resonance condition for the coupling between photons and SPP in the prism configuration is:

$$n_{prism} \sin(\theta_{SPP}) = \sqrt{\frac{\varepsilon_d \varepsilon_m}{\varepsilon_d + \varepsilon_m}} \quad (3)$$

in which n_{prism} is the refractive index of the prism and θ_{SPP} is the coupling angle (see inset of Fig. 2.4). The strongly divergent laser beam is then analyzed with a pair of knife edges that provides a slit with adjustable width. Scanning the slit through the reflected, collimated beam allows us to monitor the Au film reflectance as a function of incidence angle.

In this configuration, the energy of the incident light can be converted very efficiently into SPPs. Such energy conversion appears as a reflectance close to zero at the resonance angle, θ_{SPP}. The resonant SPP excitation condition is found by tuning the incidence angle (corresponding to tuning the in-plane wave vector) of the ultrafast laser beam and measuring its reflected power.

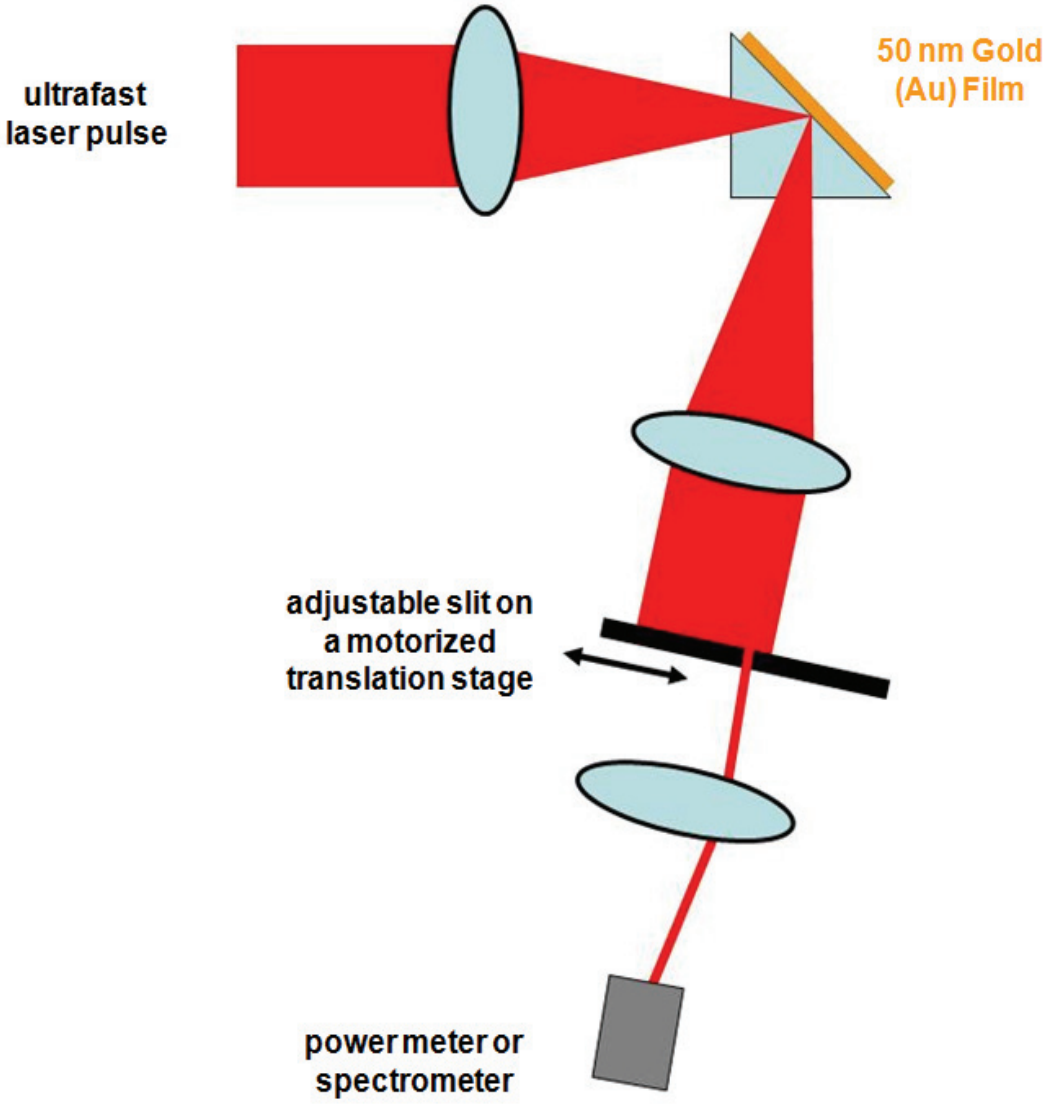

Figure 2.3: Schematic of the experimental setup to excite ultrafast SPPs.

The reflectivity drops at the coupling angle (Fig. 2.4); however, compared to calculations, the measured reflectance dip is less pronounced and suggest incomplete coupling between the femtosecond laser pulse and the SPP.

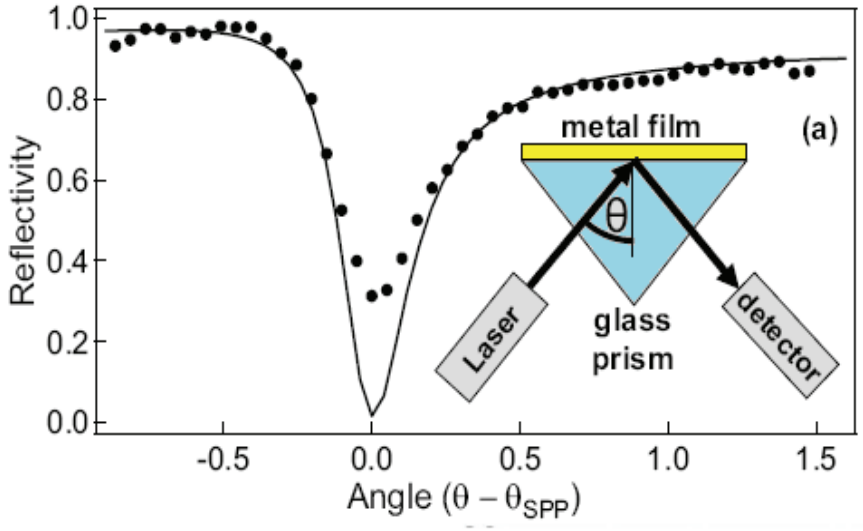

Figure 2.4: Calculated (See Ref. (*1*) for material parameters) (solid line) and measured (filled circles) reflectivity of a femtosecond laser pulse of a gold film in the vicinity of the SPP coupling angle $\theta_{SPP.}$ Inset: schematic of the prism configuration.

Since the coupling condition of equation (2) and the angle dependence of the reflectance are very sensitive to ε_d, this SPP prism configuration has been widely used for sensing (*15*) and, more recently, for studying ultrafast dynamics in thin films (*30*),(*28*).

2.3.2 Spectral Limitations of Ultrafast SPP Pulse Generation

The resonance condition for SPP excitation is not only apparent in the momentum space but also in the frequency space as a result of the frequency dependent dielectric functions. In Fig. 2.5 we show the calculated (see Ref. (*1*) for material parameters) and measured (using a tungsten halogen lamp) reflectance of a 50 nm thick gold film as a function of incidence angle and photon energy. For the calculations we considered n_{prism}=1.51 independent of the wavelength.

At a given excitation angle the reflectance drops within a finite photon energy range that defines the SPP coupling bandwidth. While for continuous wave applications this consideration has little relevance, it is expected that the broad spectrum of ultrafast pulses will be strongly affected by the finite spectral bandwidth of the resonant excitation process.

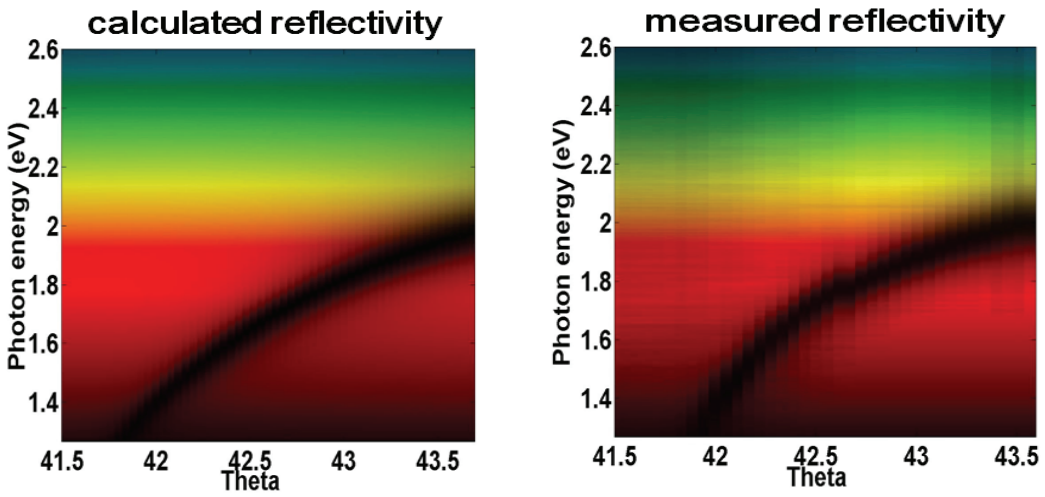

Figure 2.5: Calculated and measured reflectivity as a function of photon energy and incident angle. The colors correspond to true colors.

The spectrum of the reflected pulse at the optimal coupling angle is not only uniformly suppressed but also strongly modulated. The reflected spectrum of the excitation pulse at the optimal coupling angle θ_{SPP} shows a double peak (See Fig. 2.6), which tells that at a fixed incidence angle only a finite spectral bandwidth of the femtosecond laser pulses couples to the SPP. In addition, the spectrum of the reflected pulse depends strongly on the incidence angle. The missing part of the reflected spectrum that indicates SPP coupling moves to higher photon energies with increasing incidence angle (higher in-plane wave

vector). Such behavior is consistent with the dispersion relation of SPPs. (see eqn (2))

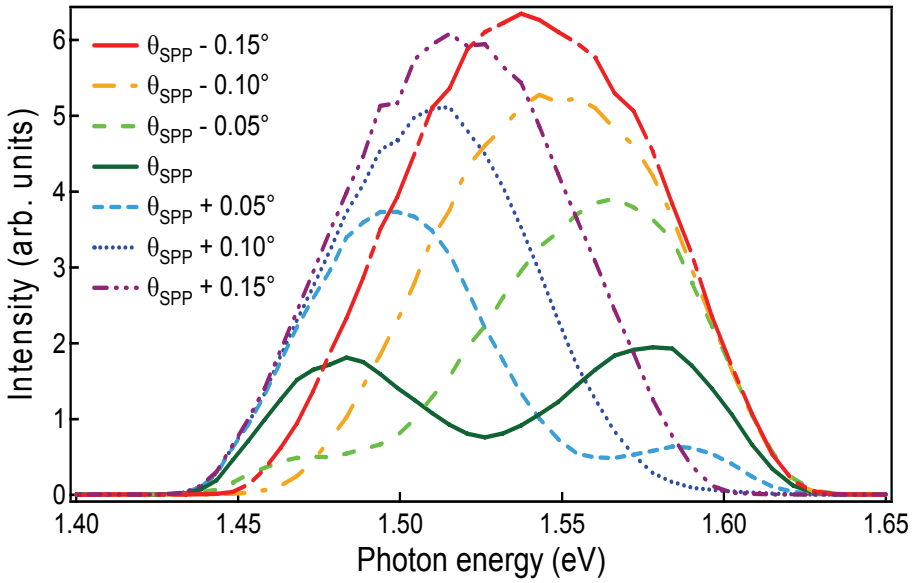

Figure 2.6: Spectra of reflected femtosecond laser pulses at different incidence angles.

2.3.3 The Narrowing of the SPP Pulse Spectrum

Since the Au film has a finite surface roughness, the SPP scatters into free space propagating light that we collected and analyzed. Assuming that the SPP scattering process varies only slightly over the wavelength range of interest, the scattered spectra represent the ultrafast SPP pulse spectra. The comparison of scattered SPP pulse spectrum and incident pulse spectrum results in scattered SPP spectrum is much narrower (22%) than the spectral width of the ultrafast laser pulse spectrum (see Fig. 2.7).

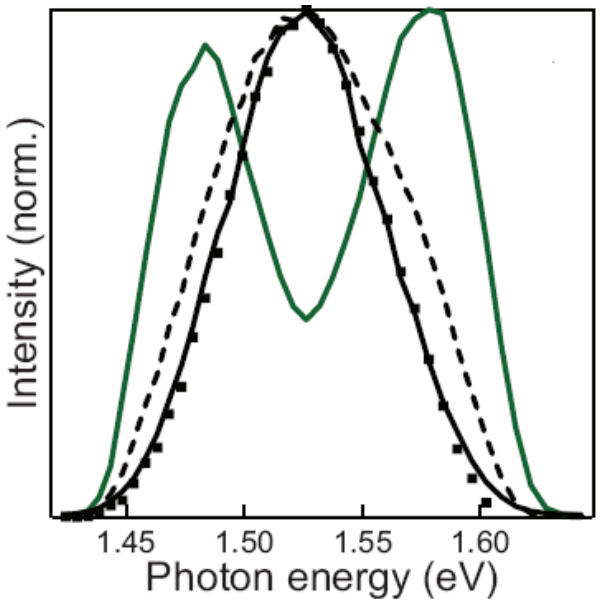

Figure 2.7: Comparison of scattered SPP pulse spectrum (black line), incident pulse spectrum (dashed line), reflected pulse spectrum at optimal SPP coupling angle (green line), and difference spectrum (square markers) between incident and reflected pulse spectra.

This is the direct consequence of the spectral filtering effect of the resonant coupling process. The scattered SPP spectrum matches closely to the difference spectrum of the incident and the reflected pulse spectra (in Fig. 2.7 the black squares), thus confirming the assumption that the reflectance dip is due to SPP coupling. It is noteworthy that the correspondence between the reflected and scattered SPP spectra illustrates nicely that the characteristics of the SPP and reflected excitation pulses are complementary and, therefore, reflected excitation pulses are well suited to analyze SPP pulses.

2.3.4 Temporal Limitations of Ultrafast SPP Pulse Generation

The spectral amplitude and phase modulations limit the duration of ultrafast SPP pulses and, in addition, affect the time resolution of pump-probe

experiments that utilize SPP excitation. To study the latter effect we determine the duration of the reflected pulse using the interferometric autocorrelation (IAC) technique. In Figs. 2.8 (a) and (b) we display the IAC of the reflected pulse under resonant SPP excitation and the IAC of the reference pulse under TIR condition

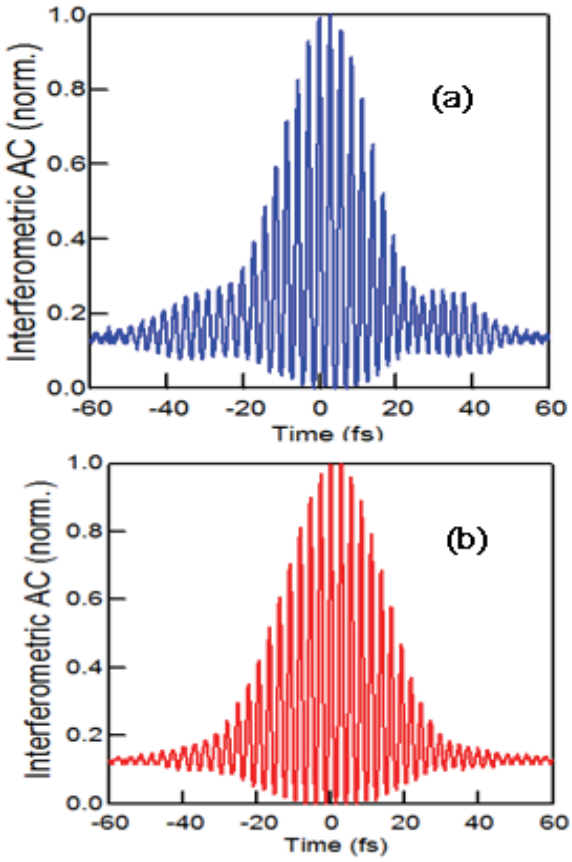

Figure 2.8: (a) IAC of the reflected pulse under SPP excitation condition, indicating strong satellite pulses. **(b)** IAC of the reference pulse taken in the TIR configuration.

The IAC of the reference pulse is the characteristic of a nearly bandwidth-limited pulse of sub 25 fs pulse duration. In contrast, the IAC of the reflected pulse under resonant SPP excitation shows a short central pulse and significant satellite pulses. The central pulse is slightly shorter than the reference pulse as a

result of the larger pulse spectrum; however, the short pulse duration comes at the expense of the significant satellite pulses that are a consequence of the resonant nature of the SPP excitation process. Such satellite pulses that extend beyond 50 fs have to be taken into account when analyzing ultrafast pump-probe measurements that employ the prism configuration.

2.4 Spectral Phase Shift Due to Resonant Excitation

Since ultrafast SPP pulse generation is a resonant process, we expect a spectral phase shift around the resonance frequency. To test this hypothesis we employ spectral interferometry to measure the phase of the reflected pulse that provides a good fingerprint of the SPP pulse (scattered SPP light cannot be used for phase measurements, since phase information is lost in the random scattering process). We let the reflected pulse interfere with a reference pulse that is split off of the excitation laser beam before the prism setup. From the interferogram (Fig. 2.9) and by using Fourier analysis we extract the phase difference between the reflected and reference pulse (*31*). The measured phase is the sum of the phase change induced by the SPP excitation and the phase contribution from the transmission of the pulse through the prism. To determine the latter phase we measure a second interferogram with the same prism setup but without a metal film (total internal reflection (TIR) configuration). The phase associated with the SPP pulse excitation (see Fig. 2.9) is then essentially the difference between the TIR phase and the SPP excitation phase. Around the SPP excitation photon energy we find a significant phase shift of

~π/2 within 50 meV. The spectral phase shift is characteristic of a resonant process and matches very well the calculated phase of the reflected electric field.

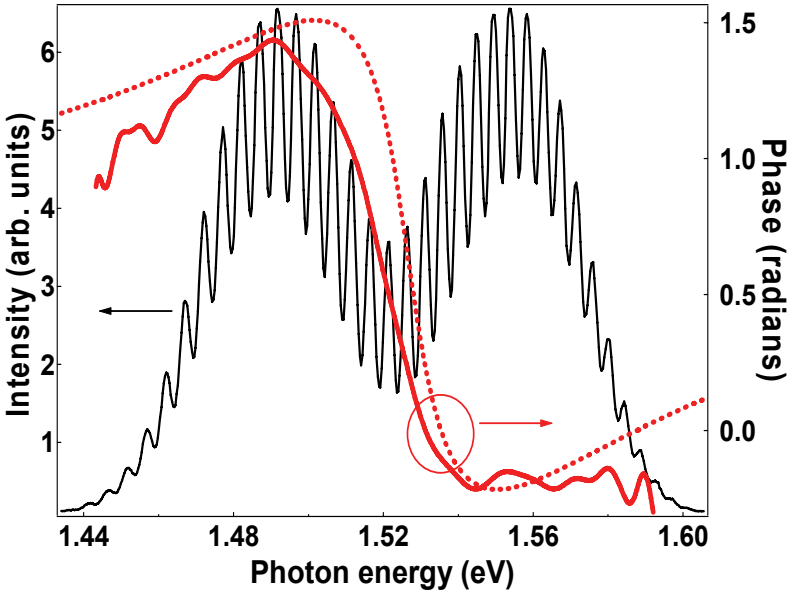

Figure 2.9: The measured phase (red solid line) of the reflected pulse at resonant SPP excitation is extracted by Fourier analysis from the spectral interferogram (black line). As a comparison we show the calculated phase of the reflected field (red dashed line).

2.5 Comparison of Gold and Silver Film

We have also repeated the same experiments for 50 nm thick silver (Ag) film. The spectral width of the SPP pulse is limited by the spectral bandwidth of the SPP prism coupling that we calculated as ~120 meV and ~40 meV for gold and silver thin films, respectively, in the near infrared wavelength range (Fig. 2.10).

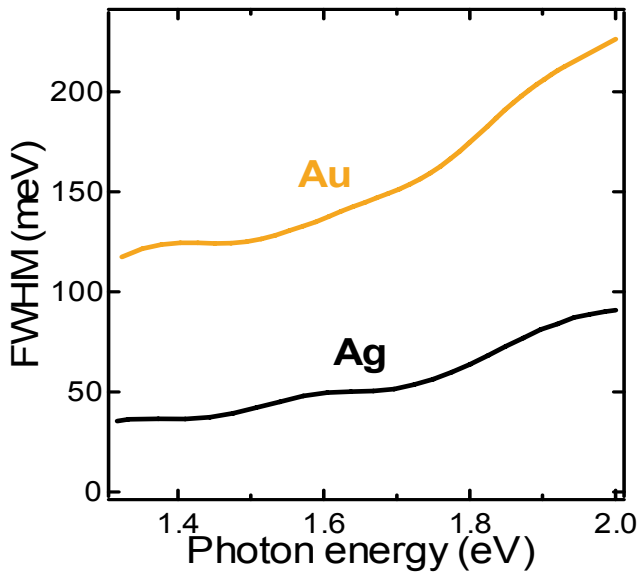

Figure 2.10: Spectral bandwidth (FWHM) of the SPP excitation by prism coupling for gold films (orange line) and silver films (black line).

The narrower bandwidth of silver films compared to gold films is attributed to lower losses (smaller imaginary part of the dielectric constant) and is consistent with a higher quality factor of the resonant excitation process in Ag films. Since the finite spectral bandwidth of the SPP coupling process limits the spectral width of the SPP pulses, it also sets a lower limit for the SPP pulse duration. The pulse duration limit is determined by the time-bandwidth product and is independent of the pulse duration of the excitation pulse. In case the entire spectral bandwidth is used for SPP excitation and a spectrally flat phase is considered, one would obtain a lower limit for SPP pulse durations of ~ 11 fs and ~ 33 fs for gold and silver films, respectively.

2.6 Summary

In conclusion, we have shown that the excitation of ultrafast SPP is strongly affected by the conventionally used prism coupling technique. This resonant excitation process causes spectral narrowing and phase shifts and leads to temporally broadened SPP pulses. Our discussion here is not restricted to the prism coupling technique, but is common to any SPP excitation process that uses resonant coupling between photons and surface plasmons. It has to be noted that both spectral narrowing and spectral phase shifts can, in principle, be compensated. The former effect can be avoided by using an excitation pulse with appropriate angle dispersion, and the latter effect by modulating the phase of the incident field using pulse shaping techniques. Such techniques have been previously suggested to manipulate plasmon fields in metal nanostructures (*32*).

2.7 Future Direction

2.7.1 Hybrid Plasmon-Exciton Interactions in Metal-Semiconductor Nanostructures

In this thesis, we focused on excitation analysis of SPPs on single component systems (only metal film). However, for real devices such as SPP switches and SPP amplifiers, dynamic and non-linear elements must be incorporated (*33*). In the continuing part of the project, one can study plasmon-exciton interactions in hybrid nanostructures to perform these challenging studies. Such heterostructured materials will exhibit enhanced functionalities because of the new coupled excitations due to plasmon-exciton attractions. It is

possible to manipulate and amplify surface plasmon polaritons (SPPs) by the ultrafast optical excitation of semiconductor nanocrystals (NCs) deposited on flat metal surfaces (*34*). Nanocrystals are attractive candidates for use in a variety of light-emitting technologies due to their high quantum yield. In semiconductor NCs, the bandgap changes by simply changing the particle size because of the effects of quantum confinement.

The most commonly used simplest experimental technique to study ultrafast electronic dynamics is pump-probe spectroscopy. In this technique, the sample is excited by a strong pump pulse, which causes a change of the absorption or reflection that is subsequently probed by a second, weak probe pulse (Fig. 2.11 (a)). The dynamics of the induced change is measured by changing the time delay between pump and probe pulses with a mechanical delay stage (Fig. 2.11 (b)).

The thickness of metal film is chosen to have the optimal resonant SPP coupling under momentum conservation conditions. Understanding the enhancement properties of these hybrid nanostructures will help us to implement them successfully to plasmonic devices such as light emitting and light harvesting devices, solar cells and sensors with enhanced sensitivity. Quantum confinement effect makes nanocrystals important candidates in light-emitting technologies.

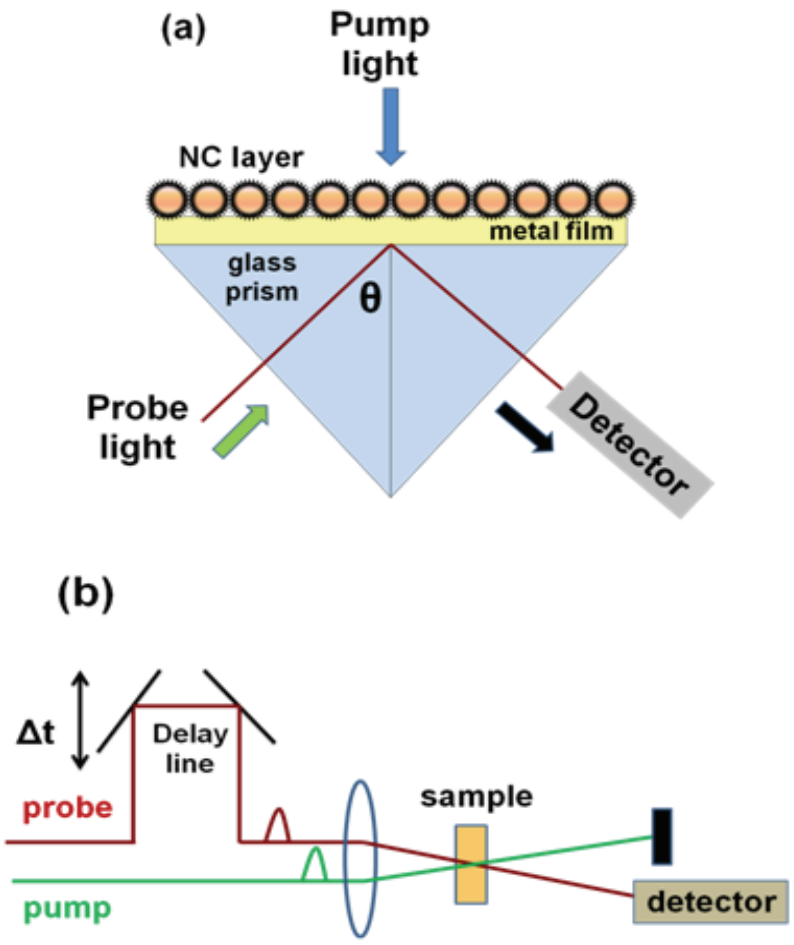

Figure 2.11: (a) Pump-probe setup to study NC-SPP excitation. **(b)** Schematic description of time delay between pump and probe arms.

2.7.2 Surface Plasmon Amplification Using Semiconductor Nanoparticles (NPs)

Concentrating all optical energy into with sub-wavelength regions is the main limitation for nano-optics researchers. This restriction stimulates scientists to look for a coherent, intense, ultrafast optical source, similar to laser but concentrated to nanoscale areas (*35*). In 2003, David Bergman and Mark

Stockman proposed such a source that is based on surface plasmons called **spaser** (short for **s**urface **p**lasmon **a**mplification by **s**timulated **e**mission of **r**adiation (*36*).

The spaser is known as the plasmonic correspondent of laser. In a spaser, SPs take the place of photons and nanoparticles behave as a resonant cavity to support the plasmonic modes. Similarly to a laser, the energy source for the spasing mechanism is an active (gain) medium that is excited externally which creates an electron-hole pairs (excitons). In a free NC, the excitons would recombine to form photons. However, when NC is sitting on the surface of resonant nanoparticle system, the excitonic recombination energy is transferred directly to the resonant SPs of the nanoparticle by doing a radiationless transition (*35*). Surface plasmons increase the transitions and system can overlap in a single SP mode in large numbers.

Once the spaser theory was introduced, many experimental groups started working on spaser to check the potential applicability of this new promising concept. One of the potential applications was nanoshell based spaser. Such nanoshells have been introduced by Naomi Halas and collaborators (*37*). Another spaser applications have been performed by Victor Klimov group by using nanocrystal quantum dots as a monolayer gain medium (*38*),(*39*),(*40*). Recently, the demonstration of nanolaser using the spaser idea is done by Mikhail Noginov and Ulrich Wiesner called spaser-based nanolaser (*41*).

Researchers have reported that it is also possible to amplify SPPs on planar metal film (*42*). In contrast to the spaser, SPPs on a flat metal surface

propagate freely and are not subjected to the cavity feedback necessary for lasing (spasing). SPP amplification can be achieved when the carrier population in the NCs is inverted which corresponds to more than one excited electron-hole pair per NC.

In conclusion, future experiments may involve exploring the possibility of using engineered hybrid devices to dynamically switch and amplify SPPs.

CHAPTER 3

LOCALIZED AND PROPAGATING SURFACE PLASMON INTERACTIONS IN FUNCTIONAL PLASMONIC NANOSTRUCTURES

Metallic nanostructures carry on the greatest potential for plasmonic device applications because of allowing light manipulation and amplification in nanometer scale. In addition, surface plasmons in metal nanostructures enable more sensitive photonic devices (*8*).

In chapter 2, we discussed and only focused on ultrafast propagating surface plasmons on thin extended metal films. In this chapter, we combine propagating surface plasmons with localized ones to study strong plasmonic interactions. For our purpose, we used block-copolymer based self assembly techniques to manufacture highly ordered gold nanoparticle arrays onto thin silver film to make composite nanoparticle thin film structures (*43*).

Experiments demonstrated that these block-copolymer-based nanostructures have strong plasmonic interactions between localized surface plasmons and SPPs that propagate at the film/nanoparticle interface, therefore, modify the dispersion relation of the SPPs by increasing the wave vector of the propagating surface plasmons. As larger wavevector corresponds to stronger field localizations (see eqn. (2)), these plasmonic nanostructures reveal great advantages for future plasmonic device applications and can serve as substrates for sensor applications or as templates for producing metamaterials with hyperbolic dispersion properties.

3.1 Block-Copolymer Based Self-Assembly Techniques

Since self-assembly of block-copolymers are cost effective, applicable to large surface area (*44-47*) and allows features size down to several nanometers, they are advantageous and more attractive in the fabrication of the metal nanostructures (*48-50*).

For the fabrication of the metal nanostructures, block-copolymer templates were prepared by Thomas Russell group from Polymer Science and Engineering Department at University of Massachusetts Amherst. Template preparations are done using spin-coating solutions of PS-b-P4VP diblock-copolymer in toluene/tetrahydrofuran (THF) (70/30, v/v) solutions onto silver thin films (Fig. 3.1). Highly ordered cylindirical P4VP microdomains oriented normal to the film surface were obtained by annealing in a saturated THF environment for 3 h. The solvent-annealed films were then immersed in a gold salt solution for 5 min to complex gold ions with the 4-vinylpyridine units. Oxygen plasma etching or sodium borohydrine ($NaBH_4$) was used to reduce the gold salt into gold nanoparticles (Fig. 3.2) (*43*).

Scanning force microscopy results revealed that these gold nanoparticle arrays have diameters ~17 nm, heights ~13 nm and center-to-center distance ~43 nm. These array dimensions correspond to a nanoparticle density of 6.2 x 10^{10} cm^{-2} and an area coverage of 14% (*43*).

Our hybrid LSP/SPP sample consists of ~50 nm thick silver films deposited by electron beam evaporation. Before depositing gold nanoparticles,

silicon oxide spacer layer is evaporated with different thicknesses onto silver film to control the interactions between localized and propagating SPs (Fig. 3.3).

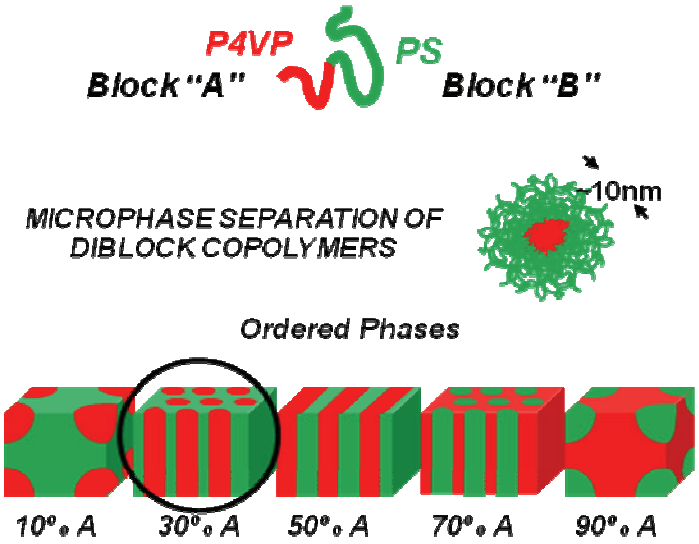

Figure 3.1: Self assembly of PS and P4VP polymers according to volume percentage. We are interested in the one that has 30% P4VP and 70% PS (*51*).

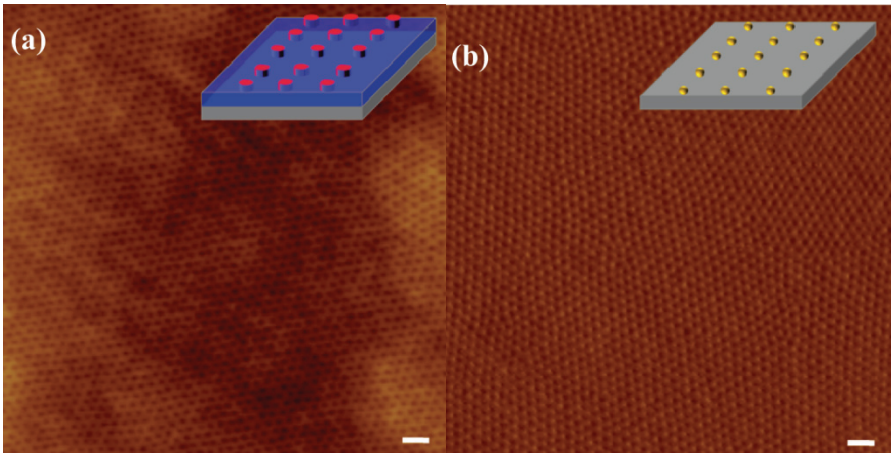

Figure 3.2: (a) SFM images of the solvent-annealed BCP template. **(b)** Gold nanoparticle array after removing the BCP template with oxygen plasma treatment. Scale bars are 100nm (SFM images are taken by Soojin Park).

3.2 Studying Plasmonic Properties of Block-Copolymer-Based Nanostructures

As we discussed in chapter 2, since the dispersion relation of SPP yields angle (momentum) and energy (frequency) dependent minima in the reflectivity, the simplest and most widely used standard way to measure the dispersion relation of the SPP is Kretschmann-Raether configuration (*27*). We focused p polarized white light to the back of the heterostructured sample and the reflectivity measurements are done under total internal reflection condition.

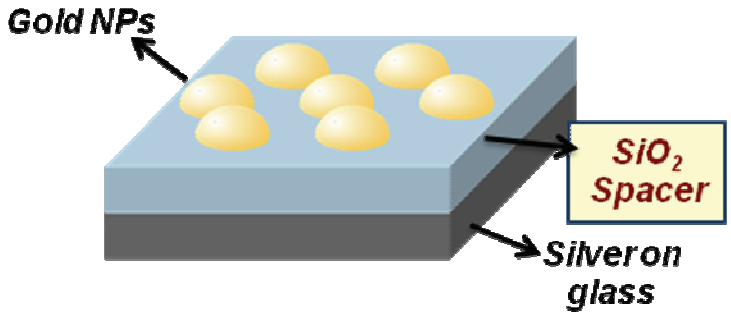

Figure 3.3: Schematic of hybrid Gold NPs/Silver thin film heterostructures with SiO_2 dielectric spacer layer with ~6 nm, ~10 nm and ~15 nm varying thicknesses.

Our measured results confirmed the theory by showing angle and wavelength dependent dip in the SPP reflectivity (Fig. 3.4 (a)). Experiments were repeated for heterostructured Au nanoparticle/Ag thin film composite samples with ~ 6 nm, ~ 10 nm, ~ 15 nm SiO_2 spacer layer thicknesses (Fig. 3.3). The measured and calculated dip in the reflectivity as a function of energy and angle is shown in Fig. 3.4. (b) and in Fig. 3.4. (c), respectively.

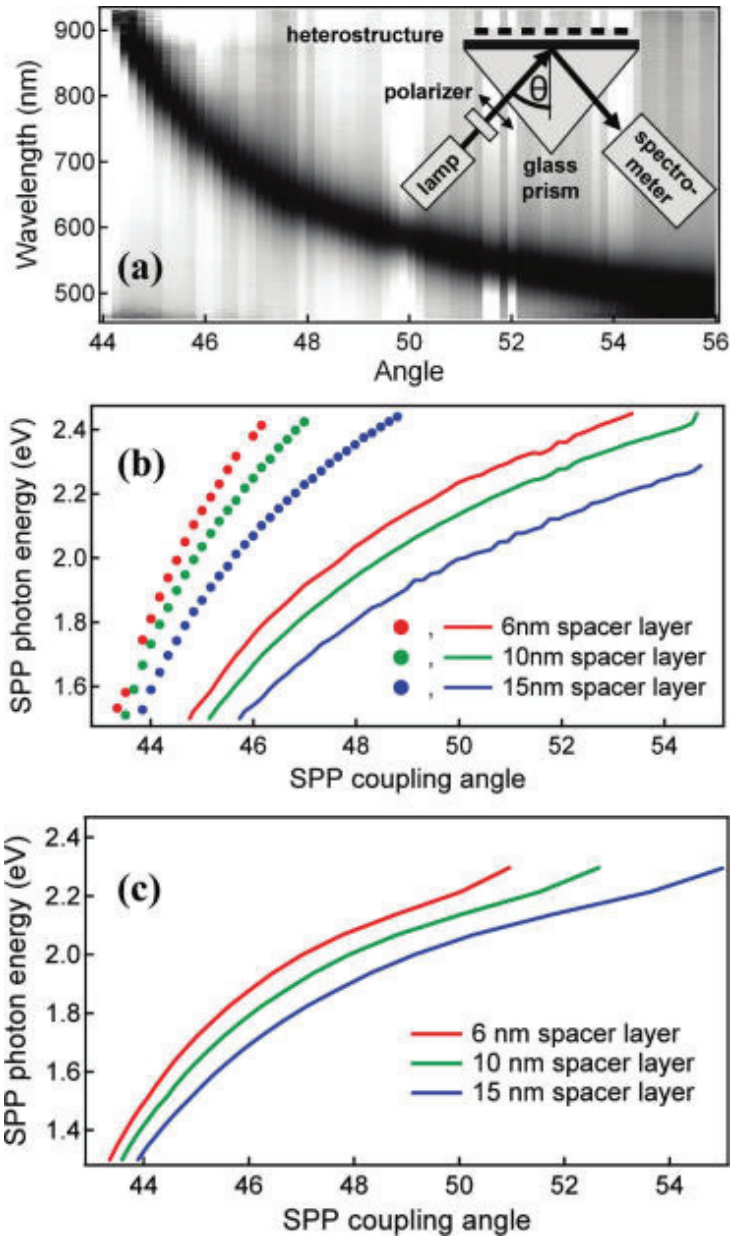

Figure 3.4: (a) Measured reflectivity of Au/Ag composite nanoparticle/thin film heterostructure with 15 nm silixon oxide spacer layer. **Inset:** Schematic of the experimental configuration. **(b)** Measured **(c)** Calculated SPP photon energy as a function of SPP coupling angle for spacer layers with thicknesses 6 nm (red), 10 nm (green), and 15nm (blue). The dotted lines in (b) are measured results from the control samples that have SiO_2 spacer layers on Ag thin film without Au NPs.

Moreover, we have performed the same experiments on control samples in the absence of Au nanoparticle arrays (see the dotted lines in Fig. 3.4 (b)). The control and hybrid samples show a clear difference at the SPP excitation angle for the same photon energy. Since the larger SPP excitation angle corresponds to larger wavevector, hybrid samples display stronger SPP excitation and field localization than control ones. Additionally, increasing the spacer layer thickness changes the effective dielectric constant between Au nanoarray on top of the silver film and leads to larger coupling angles and wave vectors (Fig. 3.4 (b)).

Consequently, the experiments with hybrid Au nanoarray/Ag thin film composite structure reveals strong plasmonic interactions between localized surface plasmons and SPPs that propagate at the film/nanoparticle interface, therefore, modify the dispersion relation of the SPPs by increasing the wave vector of the propagating surface plasmons.

To confirm our measurements, SPP dispersion relation is calculated for hybrid Au nanoparticle/Ag thin film heterostructure using multilayer system transfer matrix formalism. In our model, Au nanoparticle array layer is considered as a thickness 15 nm with oblate nanoparticles that occupy a volume fraction p (equal to the area density of the nanoarray) inside a matrix with dielectric constant ε_d. The effective dielectric function of ε_{eff} of this layer is calculated using Maxwell-Garnett effective medium theory (*52, 53*):

$$\frac{(\varepsilon_{eff} - \varepsilon_d)}{\varepsilon_d + L(\varepsilon_{eff} - \varepsilon_d)} = p\frac{(\varepsilon_m - \varepsilon_d)}{\varepsilon_d + L(\varepsilon_m - \varepsilon_d)} \qquad (4)$$

where L is the geometrical factor and ε_m is the dielectric function for gold NPs. If we extract $\varepsilon_{eff,}$ we get:

$$\varepsilon_{eff} = \varepsilon_d \frac{\varepsilon_d + L(\varepsilon_m - \varepsilon_d) p(1-L)(\varepsilon_m - \varepsilon_d)}{\varepsilon_d + L(\varepsilon_m - \varepsilon_d) - pL(\varepsilon_m - \varepsilon_d)} \quad (5)$$

Using SFM measurement results, we have approximated our gold nanoparticles as oblate ellipsoids with short and long-axes of 6.5 and 8.5 nm, respectively. Therefore, we have a/b=0.76 and we get L=0.41 geometrical factor value for electric field polarizations along the short axes (*54*), because the strongest electric field component of propagating surface plasmon is in the z direction. For volume fraction we have taken p=0.14 and ε_d=1. The calculated SPP resonance photon energy as a function of excitation angles for 6 nm, 10 nm and 15 nm is given in Fig. 3.4 (c).

The good agreement between the calculated and the measured results support our interpretation and model that the reason for the increased SPP wavevector is because of gold nanoparticle arrays. The reflectivity calculations are done by using multilayer transfer-matrix formalism (see below).

3.3 Multilayer Transfer-Matrix Method for Reflectivity Calculations

Recent progress in nano-engineering and nano-manufacturing presents new opportunities for plasmonics and photonics society. Especially multilayer designs are more promising for light manipulation and amplification. However,

calculating the propagation of electromagnetic (E&M) wave through many layers is cumbersome and complicated because of infinite number of reflections (Fig. 3.5). The best way to calculate the E&M wave propagation through multilayer systems is using Transfer-Matrix Formalism (TMF).

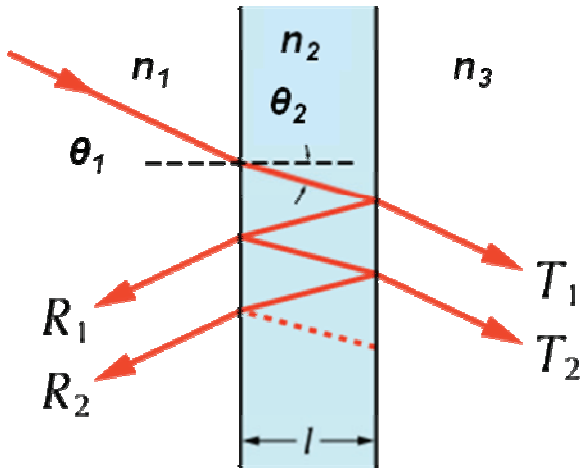

Figure 3.5: E&M wave propagation through multilayer system (adapted from wikipedia).

In TMF, every layer is represented by its own 2x2 system matrix. For the interface between material 1 and 2, we use Snell laws and consider the p-polarization condition in the definition of the system matrix.

$$M = \frac{n_2}{n_1}\frac{1}{1+r_{12}}\begin{pmatrix} 1 & r_{12} \\ r_{12} & 1 \end{pmatrix} \quad (6)$$

$$r_{12} = \frac{n_2 \cos\theta_1 - n_1 \cos\theta_2}{n_2 \cos\theta_1 + n_1 \cos\theta_2} \quad (7)$$

Absorption of the layer is defined with a absorption matrix N.

$$N = \begin{pmatrix} \alpha & 0 \\ 0 & \alpha^{-1} \end{pmatrix} \quad (8)$$

$$\alpha = e^{-ink_x l} = e^{-in\frac{2\pi}{\lambda}\cos\theta_2 l} \quad (9)$$

The formalism uses continuity conditions for the E-fields at the boundary from one layer to another layer.

$$E_{in} = \begin{pmatrix} E^{f}_{in} \\ E^{b}_{in} \end{pmatrix} = M_{tot} \begin{pmatrix} E^{f}_{out} \\ E^{b}_{out} \end{pmatrix} \quad (10)$$

The product of each system matrices gives one matrix that represents the multilayer system. It should be noted that in this symbolism, **f** corresponds to **"forward"** and **b** corresponds to **"backward"**.

$$M_{tot} = M_{0,1} N_1 M_{1,2} N_2 \ldots\ldots\ldots M_{(n-1),n} \quad (11)$$

$$\begin{pmatrix} E^{f}_{in} \\ E^{b}_{in} \end{pmatrix} = \begin{pmatrix} M^{00}_{tot} & M^{01}_{tot} \\ M^{10}_{tot} & M^{11}_{tot} \end{pmatrix} \begin{pmatrix} E^{f}_{out} \\ E^{b}_{out} = 0 \end{pmatrix} \quad (12)$$

The final matrix is used to extract the reflection R and transmission T coefficients.

$$R = \left| \frac{E^{b}_{in}}{E^{f}_{in}} \right|^2 = \left| \frac{M_{10}}{M_{00}} \right|^2 \quad (13)$$

$$T = \frac{n_n}{n_0}\left|\frac{E^f{}_{out}}{E^f{}_{in}}\right|^2 = \frac{n_n}{n_0}\left|\frac{1}{M_{00}}\right|^2 \quad (14)$$

3.4 Summary

We have studied LSP and SPP interactions in hybrid Au nanoparticle/Ag thin film heterostructures. Long range ordered gold nanoparticles were deposited on silver film by using diblock-copolymer self assembly techniques. Experiments demonstrated that these block-copolymer-based nanostructures have strong plasmonic interactions between localized surface plasmons and SPPs that propagate at the film/nanoparticle interface, therefore, modify the dispersion relation of the SPPs by increasing the wave vector of the propagating surface plasmons, leading to strong electric field enhancements. Therefore, these metal nanoarrays are promising candidates for plasmonic and photonics applications (*43*).

CHAPTER 4

BUILDING A NEAR-FIELD SCANNING OPTICAL MICROSCOPE TO VISUALIZE ULTRAFAST SURFACE PLASMON PULSES

Metallic nanostructures are considered to be attractive building blocks for optical circuits and telecommunication applications because of their ability to guide and confine light beyond the diffraction limit. Understanding plasmon propagation in metal nanostructures is an important prerequisite to implement such structures successfully into opto-electronics and plasmonic devices.

We have designed and constructed an exceptional instrument called femtosecond photon scanning tunneling microscope (fsPSTM), to investigate pulse propagation and associated dispersive properties of plasmonic structures. The fsPSTM is a unique instrument that combines femtosecond optical spectroscopy techniques with nanometer scale resolution of scanning probe microscopy tools (*55, 56*).

Temporal and phase information have been obtained by incorporating the fsPSTM into one arm of a Mach-Zehnder interferometer, allowing heterodyne detection. We have done successful tracking and imaging of 50 fs SPP pulses on metal thin films using home-built fsPSTM. Observing 50 fs pulse propagation using PSTM is an important accomplishment and will give us critical information to determine the dispersion properties of plasmonic structures.

4.1 Near-field Optics

Developments in nanoscience, biotechnology and photonics offer great challenges for the characterization and exploration of optical interactions on the nanoscale. By using conventional optical imaging, it is impossible to go such nanometer length scales because of the resolution limit of free propagating light. Near-field microscopy techniques have led to the development of the new area of research called near-field optics (*57*). In this technique, scientists use non-propagating, evanescent waves to go beyond the diffraction limit.

The first idea to circumvent the diffraction limit in order to obtain spatial resolution in the 100nm range was proposed in 1928 by E.H. Synge (*58*). However, because of the technological restrictions, the first near-field optical microscopes have been developed in 1984 at IBM (*59*) and at the Cornell University (*60*) independently. Both applications were based on aperture near-field optical microscope (NSOM) (*61*).

The basic principle of NSOM is based on having a sub-wavelength aperture at the tip apex and bringing the near-field probe significantly closer (tens of nm) to the surface of interest. In that case the size of features which can be imaged is limited primarily by the size of the aperture, not the wavelength of light (*62*). The achieved resolution is far better than conventional optical microscopes (~ 100 nm). The tip is raster scanned in close proximity over the sample to maintain a constant sample-tip separation using a feedback mechanism.

The most common NSOM operation modes are collection (Fig. 4.1(a)), illumination (Fig. 4.1(b)), collection/illumination (Fig. 4.1(c)), angled collection

(Fig. 4.1(d)), angled illumination (Fig. 4.1(e)) and total internal reflection (TIR) based collection (see Fig. 4.1(f)) (*2*).

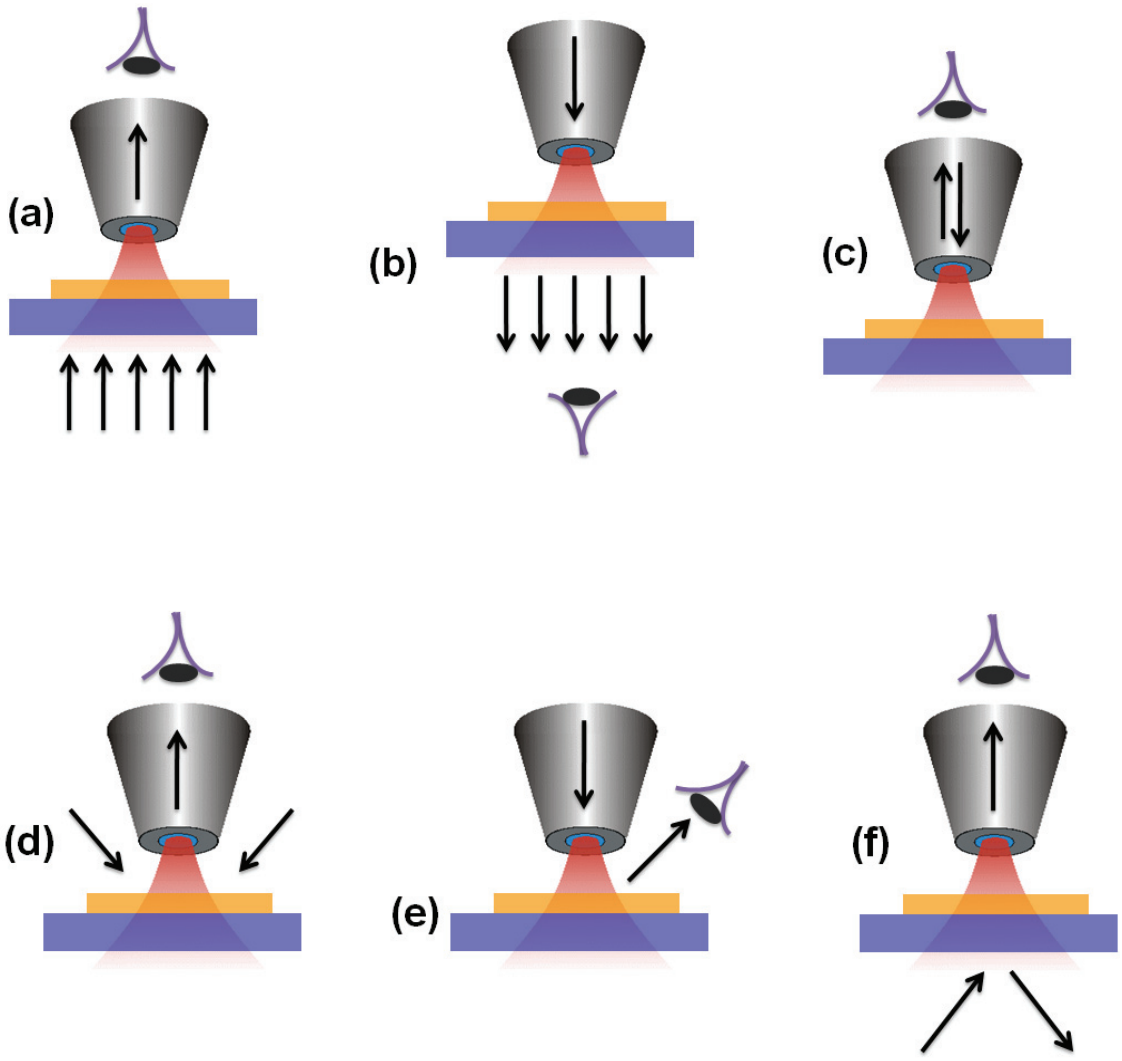

Figure 4.1: (a) Collection mode NSOM operation. **(b)** Illumination mode NSOM operation. **(c)** Collection and Illumination mode NSOM operation. **(d)** Angled collection mode NSOM operation. **(e)** Angled illumination mode NSOM operation. **(f)** Total Internal Reflection (TIR) based collection mode NSOM operation (Adapted from ref. (*2*)).

In the near-field illumination mode, the light emerging from the aperture is scattered or transmitted by the surface and detected in the far-field with a photodetector. In the near-field collection mode, the light from the surface is coupled to the tip and then detected by the far-field detector.

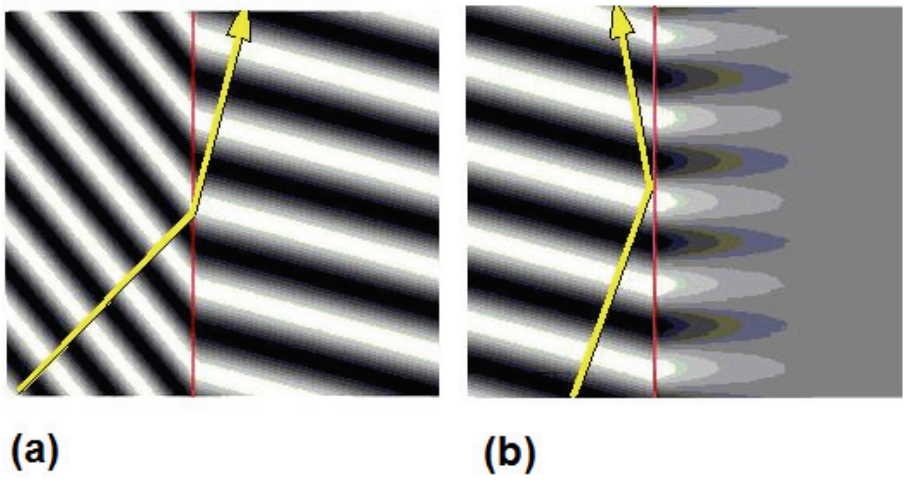

Figure 4.2: **(a)** Refracted wave at the boundary **(b)** Evanescent wave at TIR boundary (source is wikipedia)

In the total internal reflection (TIR) based NSOM applications, incident light is reflected from the surface of a glass prism with an angle greater than the critical angle (Fig. 4.2 (b)). In this geometry, although the light is totally reflected back into the initial medium, the electromagnetic field associated with the light wave continues through the boundary to the other side of the medium. This bound, refractive wave is called “evanescent wave” and decays exponentially in the direction perpendicular to the surface. When the near-field probe is brought to be in contact with the evanescent wave, the probe disturbs this bound wave and converts the bound modes to propagating modes through the tip. Therefore

we can have near-field images with high optical resolution, which allows us to go beyond the diffraction limit.

The power and beauty of the NSOM is having topography and optical images at the same time during the raster scan.

4.2 Design, Development and Instrumentation of Femtosecond Photon Scanning Tunneling Microscope (fsPSTM)

To study ultrafast surface plasmon pulse propagation, we used a new form of NSOM, so called femtosecond photon scanning tunneling microscope (fsPSTM) [(*63*)]. In principle, it is possible to build a fsPSTM by slightly modifying the commercially available near-field scanning optical microscope (NSOM). However, the versatility of commercial instruments is often limited and it is not easy to modify them for non-standard configurations. Therefore, we designed and constructed a home-built version of fsPSTM to use for our specific purpose. Our design is much more economical and easily maintainable compared to commercial PSTMs.

In this microscopy technique, the evanescent field of an electro-magnetic wave that propagates inside a photonic/plasmonic structure couples to a near-field optical probe (collection mode) that is held a few nanometers above the surface (Fig. 4.3). A small fraction of the propagating wave can be extracted from the structure and sent to a detector. While scanning the tip over the surface at a constant tip-to-sample distance, the intensity distribution of the propagating wave

in combination with the topography of the sample is recorded with high, typically 100 nm, spatial resolution.

In addition to the amplitude distribution of the electric field, the phase and the time evolution of an SP pulse that is launched by a femtosecond laser pulse can be spatially resolved interferometrically mixing the extracted pulse with a reference pulse that is split from the same laser source. A variable time delay line within the reference branch of the setup allows for mapping SP pulses that propagate within the photonic/plasmonic structure. The phase of the propagating pulse is obtained with a heterodyne-detection scheme.

In the design period of the fsPSTM, we have divided the whole system into five subsystems and worked on construction, development and testing of every subsystem independently. At the end, they have been integrated and tested together to complete the whole system. The important subsystems that we had to deal with separately were (*64*):

1) The Distance Feedback Control
2) X-Y-Z Nanopositioner Control
3) Sample Position Control and View
4) Near-field Tip Preparation
5) Hardware/Software Response and Control System

4.2.1 The Distance Feedback Control

In near-field microscopy, one of the most important concerns is keeping the tip in the near-field region, on the order of tens of nanometers away from the

surface. Having constant tip-sample separation during the raster scan is also another essential and challenging issue. Since the geometry of the surface changes drastically, the tip should be aware of and react in a quick way to the height changes. Therefore, we need to have a distance dependent feedback loop to maintain constant tip-sample distance. There are two main feedback mechanisms used in NSOM operations:

1. Normal force feedback
2. Shear-force feedback

Normal force feedback in NSOM works similar to the standard feedback mechanism used in Atomic Force Microscopes (AFM). In this feedback technique, cantilevered tip is attached to a piezo element, driven with a sinusoidal voltage that leads to the oscillation of the tip perpendicular to the surface (See Fig. 4.3 (c)). At the resonance frequency of the oscillation, the amplitude increases drastically. The oscillation of the tip gets damped, when the tip is very close to the sample due to the acting normal forces between the tip and the surface. Generally laser monitored cantilever tips are used for this feedback mechanism.

In the shear-force feedback, straight tips are attached to piezo element which is driven mechanically parallel to the surface. In this feedback system, since the oscillation of the tip is parallel to the surface, the forces that are used as a feedback mechanism are shear or lateral forces. When the tip is very close to the surface, these lateral forces act strongly between the probe and the surface, therefore oscillation of the tip gets damped. Shear force feedback can

be used by focusing a laser on the tip and looking at the reflection of the laser at the photodiode (Fig. 4.3 (a)).

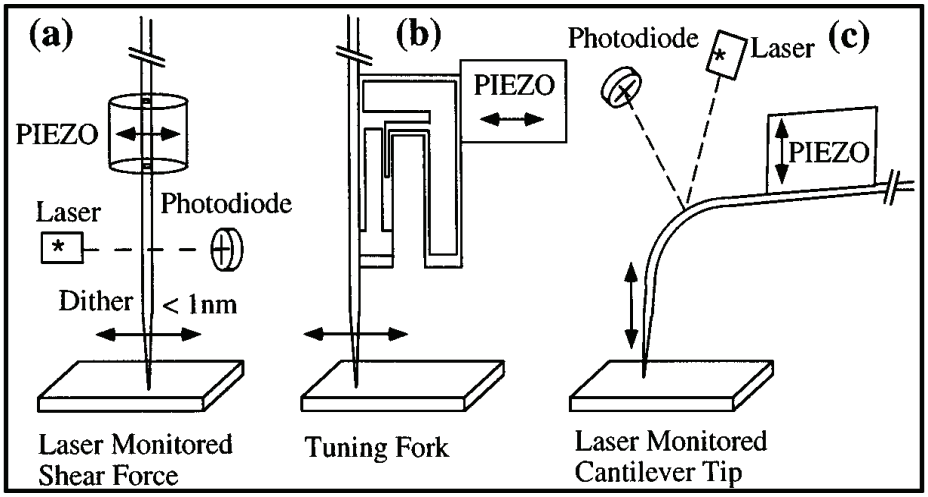

Figure 4.3: (a) Laser monitored shear-force feedback **(b)** Tuning fork based shear-force feedback **(c)** Laser monitored cantilever tip shear-force feedback (*65*).

Quartz tuning forks can be used efficiently as a piezoelectric element to have a more sensitive feedback mechanism (Fig 4.3 (b)). In our NSOM design we have used tuning fork based shear-force feedback mechanism. The tuning forks (Digikey, part no: 535-9034-ND) used in our system have a resonance frequency around 32.768 kHz. They are commercially available with an aluminum tube enclosure. In order to use, aluminum tube protection must be broken gently by crashing the casing base (Fig. 4.4).

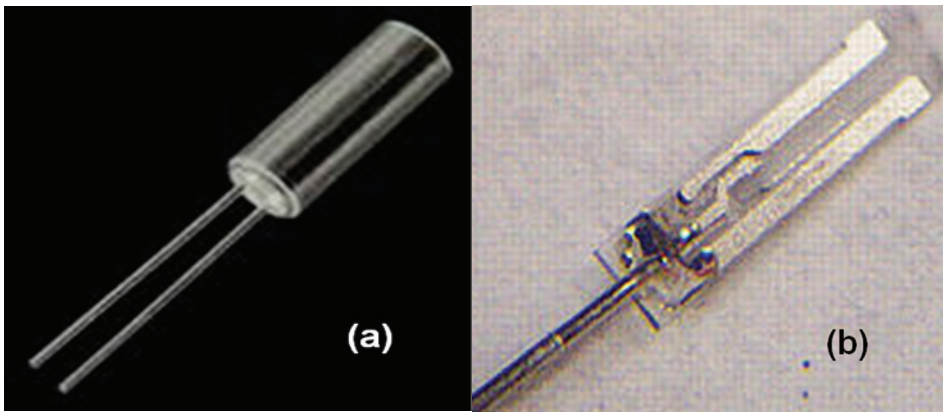

Figure 4.4: Quartz tuning forks **(a)** with aluminum protection capsule. (Source Digikey) **(b)** after removing the capsule. (Source Pacific Northwest National Lab.)

The near-field tip is glued to one leg of a tuning-fork that is mounted on a dithering piezo (Fig. 4.5). Function generator (Stanford Research Systems DS-335) is used to drive the dither-piezo by applying sinusoidal voltage. The dither-piezo leads to an oscillation of the tip apex with amplitude of around 5 nm. The movement of the tip is converted into a voltage signal by the small piezo-electric tuning fork. Using a lock-in amplifier at the driver frequency, the amplitude of the oscillation is extracted. As the fiber is brought to within roughly 15 nm of the surface, the oscillation is damped due to shear forces that act between the tip and the sample. When the tip-sample separation goes to zero, the tip amplitude becomes zero. Therefore, by maintaining a constant oscillation amplitude of the near-field tip, a constant tip-sample separation is obtained.

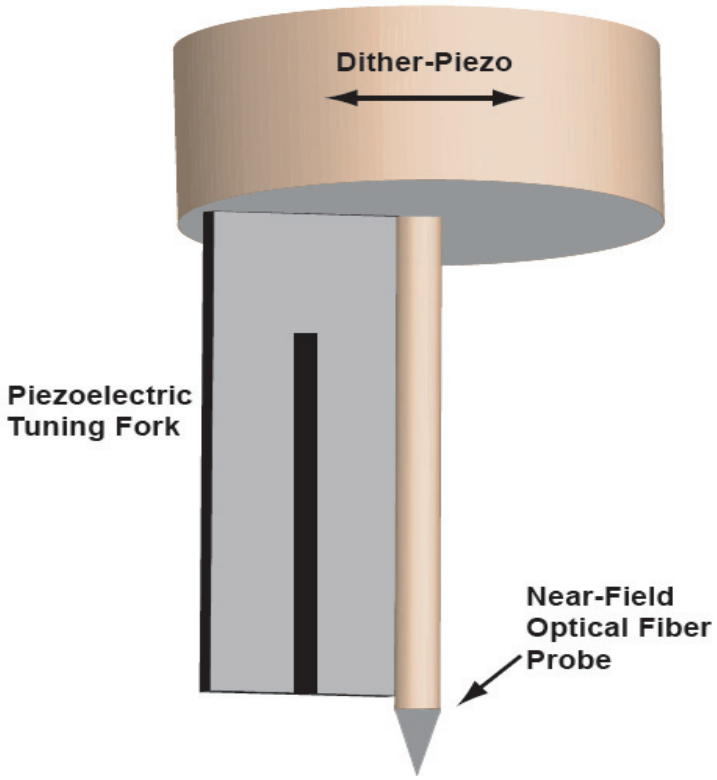

Figure 4.5: Dither-piezo that carries the near-field probe and tuning fork assembly. Shear-force is used to provide the feedback information.

The tuning fork has a length around 5 mm. The conductive leads of the tuning forks are at the end of the legs. We have designed two special teflon parts (disk and cap) to attach the tuning fork and tip system to the piezo tube (*64*). The tip and tuning fork system are attached to a specially designed easily removable teflon disk (See Fig. 4.6).

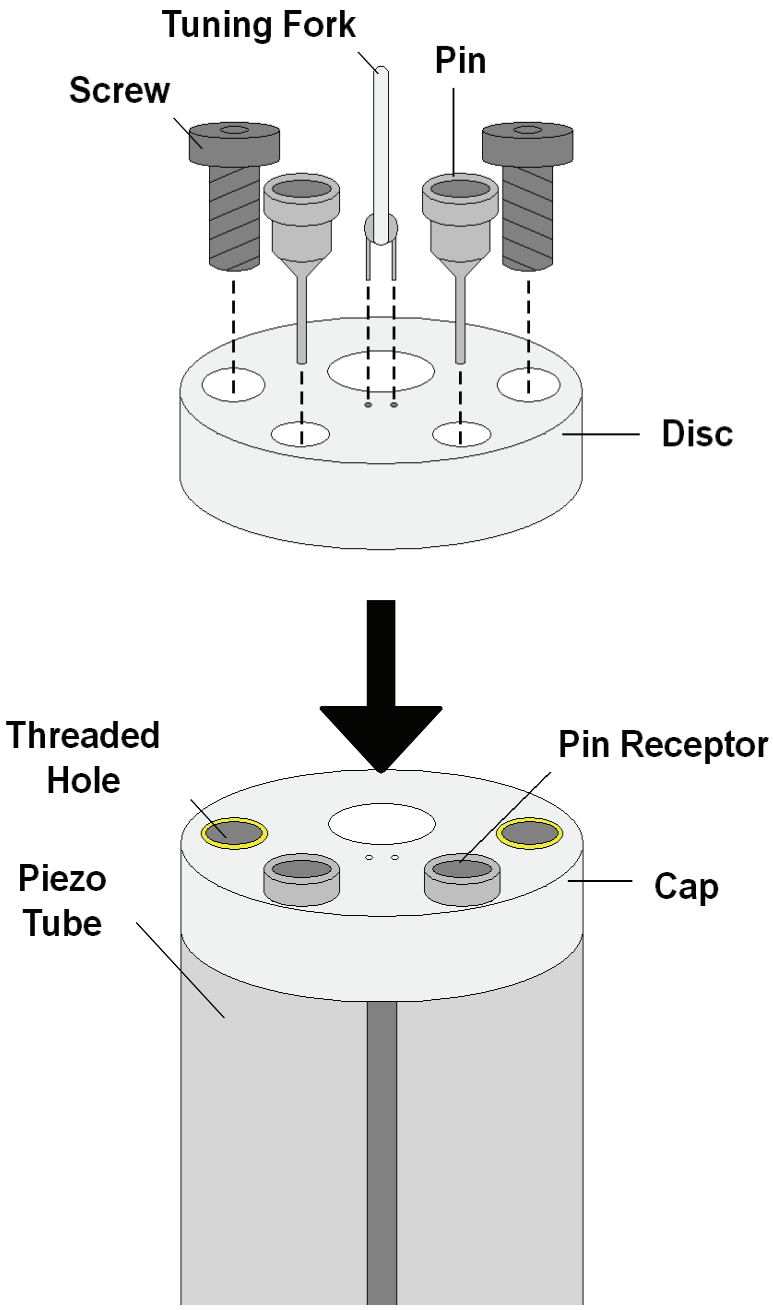

Figure 4.6: Schematic of the cap, disk and dither piezo tube assembly. Teflon disc holds the piezolecetric tuning fork and the near-field probe. Disc is attached to teflon cap with side screw (*66*) (Image credit David Oullette).

The disk has small diameter holes to hold the tuning fork leads, much bigger special central hole which is perfectly aligned to the one leg of the tuning

fork to easily glue the near-field probe on it and other holes for screws and pins (*66*). Once the tuning fork is glued to the disk, silver paint is used to make electrical connections between the each conductive leg of tuning forks and the pins on the teflon disk. After the gluing and silver paint application process, the caps are kept in a safe box to protect them from any possible damage (Fig. 4.7).

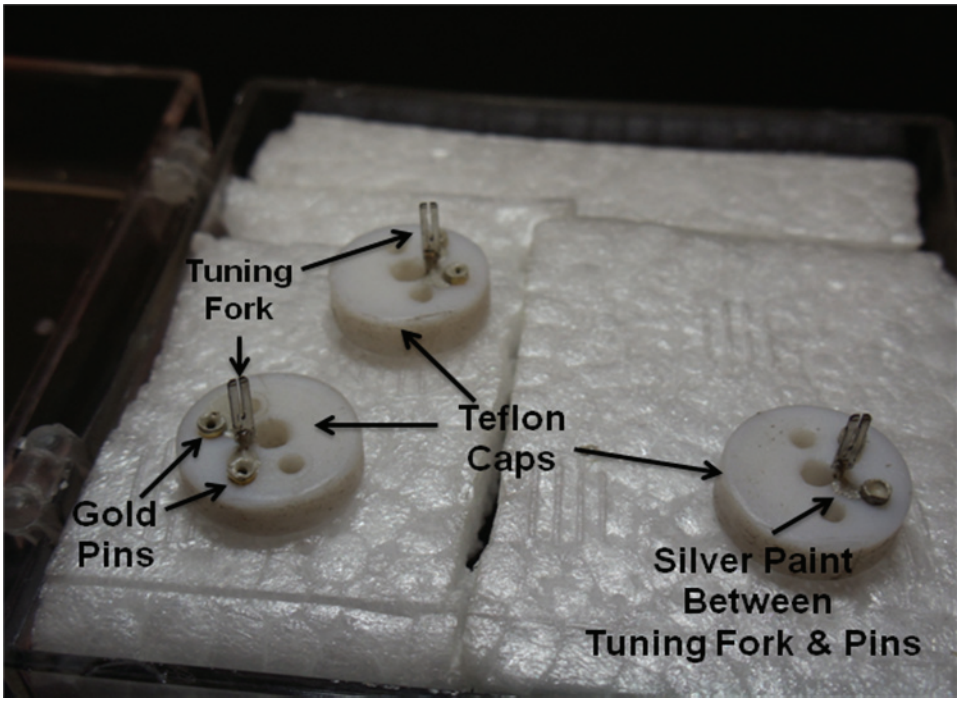

Figure 4.7: Teflon caps in their closed box.

When the silver paint dries, it is important to make a conductivity test to find out the conductivity resistance between the each tuning fork legs and the corresponding pins. Since the tuning fork is not conductive, there should not be any connection across the legs of the tuning forks. If an electrical connection

exists between the legs of the tuning forks, any conductive material is removed using an acetone (*64*).

We have designed another teflon cap and mounted to the dithering piezo tube (Fig. 4.6). The cap has pin receivers and threaded holes for the screws. The pin receivers are soldered to the BNC connector which goes to the lock-in input. Therefore, when we attach the teflon disk to the teflon cap on the tube, the voltage of the BNC represents the voltage across the tuning fork.

4.2.2 X-Y-Z Nanopositioner Control

In our fsPSTM, we keep the sample fixed and move the tip over the sample surface because tip scanning microscope makes our experiments much easier than sample scanning microscope design. To control the motion of the tip, we have used three axis nanopositioner stage (Mad City Labs Nano-T222) which can move 200 μm in x and y directions and 20 μm in z direction (Fig. 4.8).

The main step in the scanning part is mounting the dithering piezo that carry the piezoelectric tuning fork and tip assembly carefully on the nanopositioner. This must be done in a way that allows the tip and tuning fork to approach the surface vertically. We have designed an aluminum base to attach the dithering piezo (See Fig. 4.9 and Fig. 4.10). The design is done in a special way that it points vertically down towards the sample and allows clearance from the cutoff opening for the output wires and optical fiber attached the tuning fork. The screw holes were drilled on the base so that the aluminum base can be screwed easily to the nanopositioner stage (*64*).

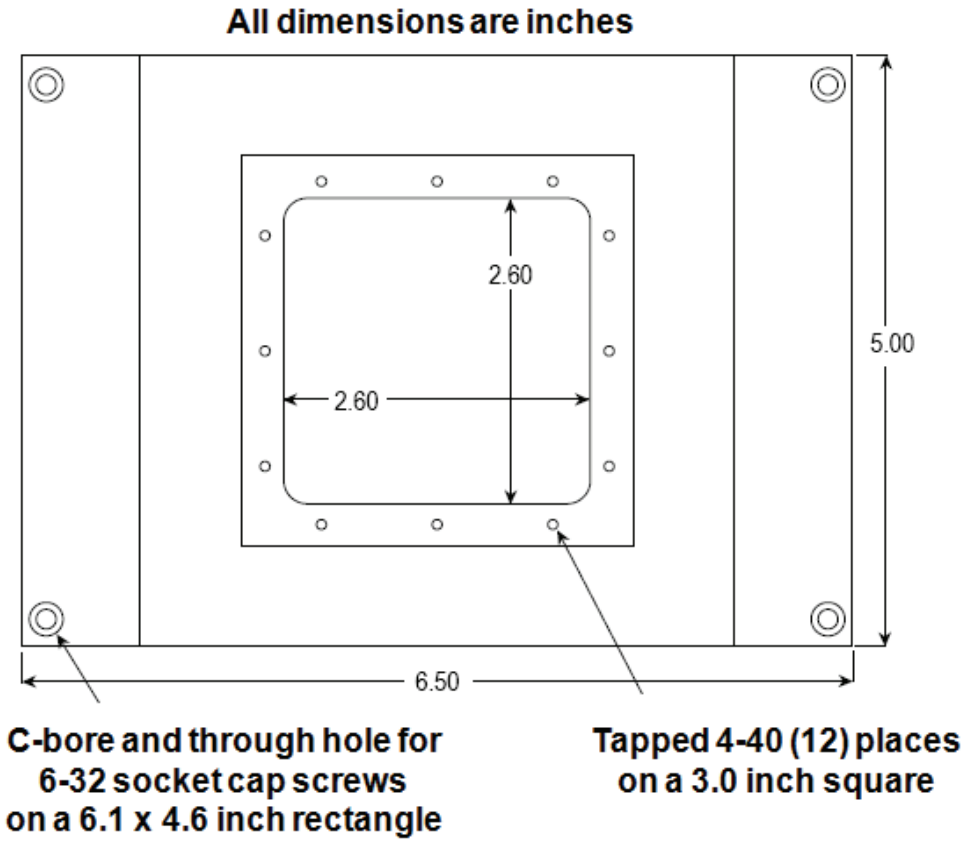

Figure 4.8: T-222 three axis nanopositioner with central holes (*67*).

The stage can be operated with 16 bit USB NanoDrive. The operation can be done using closed loop or open loop cycles. In the case of closed loop, the capacitor inside the stage allows a correction to the movement. In the open loop operation, the correction loop is deactivated so that an outside control loop can be used (*64*).

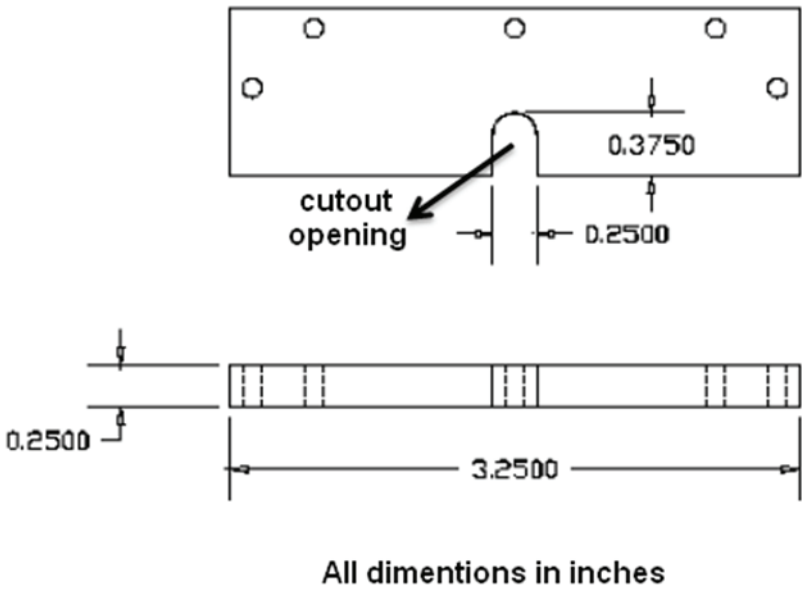

Figure 4.9: Aluminum mount for dither piezo with mounting holes and cutoff opening which allows the wires and fiber to pass through (*64*) (Image credit Daniel Brosnan).

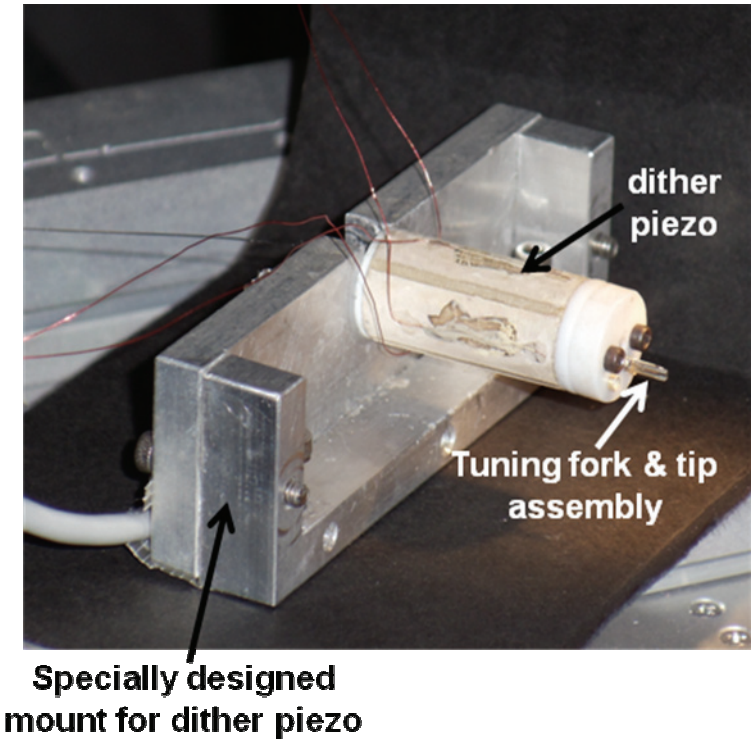

Figure 4.10: The picture of dithering piezo tube of fsPSTM.

4.2.3 Sample Position Control and View

For our design fsPSTM, we illuminate 826 nm, 50 fs, Ti:Sapphire pulsed laser to the metal surface by using total internal reflection geometry to excite ultrafast surface plasmon polaritons and we couple the evanescent wave of SPPs to the near-field probe. Therefore the samples sit on top of a one inch prism (See Fig. 4.11 (a)). In order to mount the prism with the face up, an aluminum right angle cradle was designed and mounted on a standard optical post. The optical post is attached to 2 axis translation stage (two single axis translation stages on top of and perpendicular to each other) (*64*).

The entire sample positioning system sits on a Thorlabs LJ750 compact lab jack, which provides vertical translation to the prism and sample system (Fig. 4.11 (b)). Therefore, we can have 3-axis control for the sample movement. All of the positioning systems are necessary to have a mobile prism and sample system which can move independently than near-field probe.

The coarse approach to the surface is done by using an optical microscope that has stereo zoom between 0.8X to 4X (See Fig. 4.22). The important trick is to be able to see the reflection of the near-field tip on the surface of the metal film. In the case of thin extended metal film, tip reflection is prominent enough to see clearly. If the sample geometry is more complicated than metal film, seeing the reflection of the tip over the sample surface might be hard.

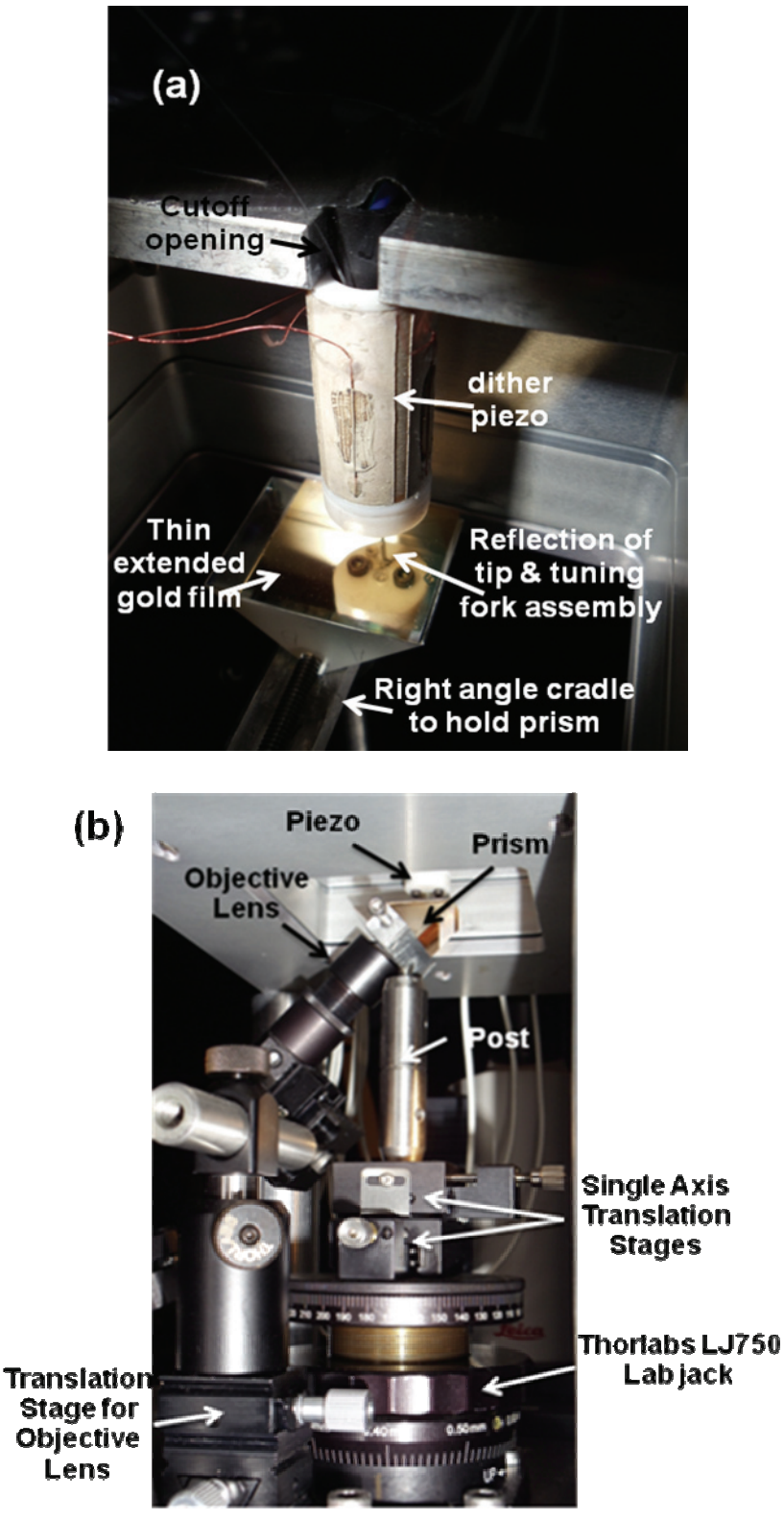

Figure 4.11: The picture of **(a**) dither piezo which is attached to Al mount, and also gold film and prism **(b)** Thorlabs LJ 750 lab jack with 2-axis positioner.

4.2.4 Near-Field Tip Preparation

As a local probe, we use optical near-field tips that are pulled by a Sutter P-97 micropipette puller (Fig. 4.12). The tips have been produced from Thorlabs 780HP single mode optical fiber that has operation wavelength between 780-970nm.

Figure 4.12: P-97 micropipette puller has been used to prepare near-field tips (Sutter Instrument Corporation).

The optical fiber is stripped from the center around 1cm by using micro-strip from Micro Electronics Inc. and then the stripped part is heated and pulled using micropipette puller. The machine heats the glass with a filament and during the heating, glass fiber gets thinner and softer. As a final step, the machine mechanically pulls the glass apart, allowing two sharp tips at the end.

The heating and pulling parameters are important to have nicer shaped, symmetric near-field probes at each pulling. Especially the opening cone angle of the tip is highly critical to have better coupling through the probe. The outer surface also plays a crucial role in the topography resolution of the image.

Because of all these reasons, we needed to find out the best input parameters for the best near-field probe fabrication.

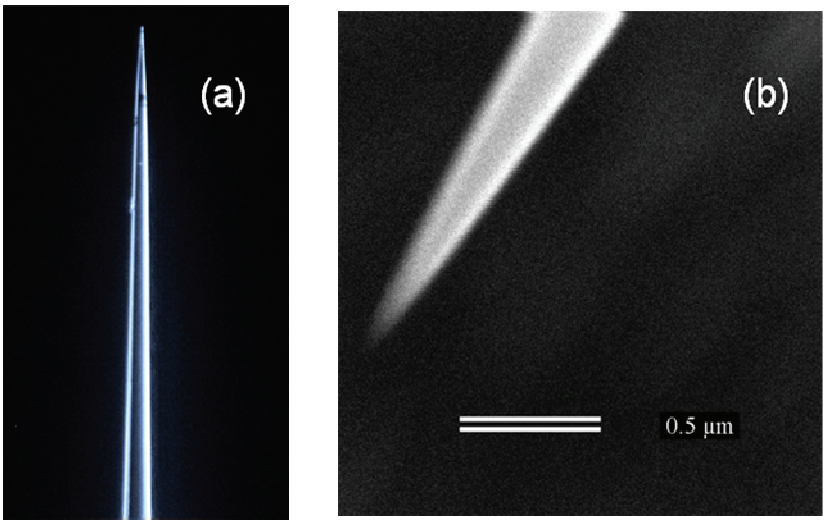

Figure 4.13: (a) Optical microscope image of our near-field tip at 32X magnification (*64*) (Microscope image is taken by Daniel Brosnan). **(b)** SEM picture of ~ 100 nm wide near-field tip used in our experiment (SEM image is taken by Taylor Esformes).

We have done many test pullings by using different heat and pulling parameters. After every test trials, the shape of the probes has been checked under optical and scanning electron microscopes to have a reasonable idea about the shape of the tip (Fig 4.13). Since the size of the aperture determines roughly the spatial resolution that can be obtained in two-dimensional scans, many topography and optical test scans have been also performed simultaneously by using these produced near-field tips to decide the best and efficient near-field probes (See Fig. 5.3, 5.4 and 5.7).

The tip is carefully attached to the one leg of the tuning fork with the help of a translation stage (Fig. 4.14) and an optical microscope (Fig. 4.15).

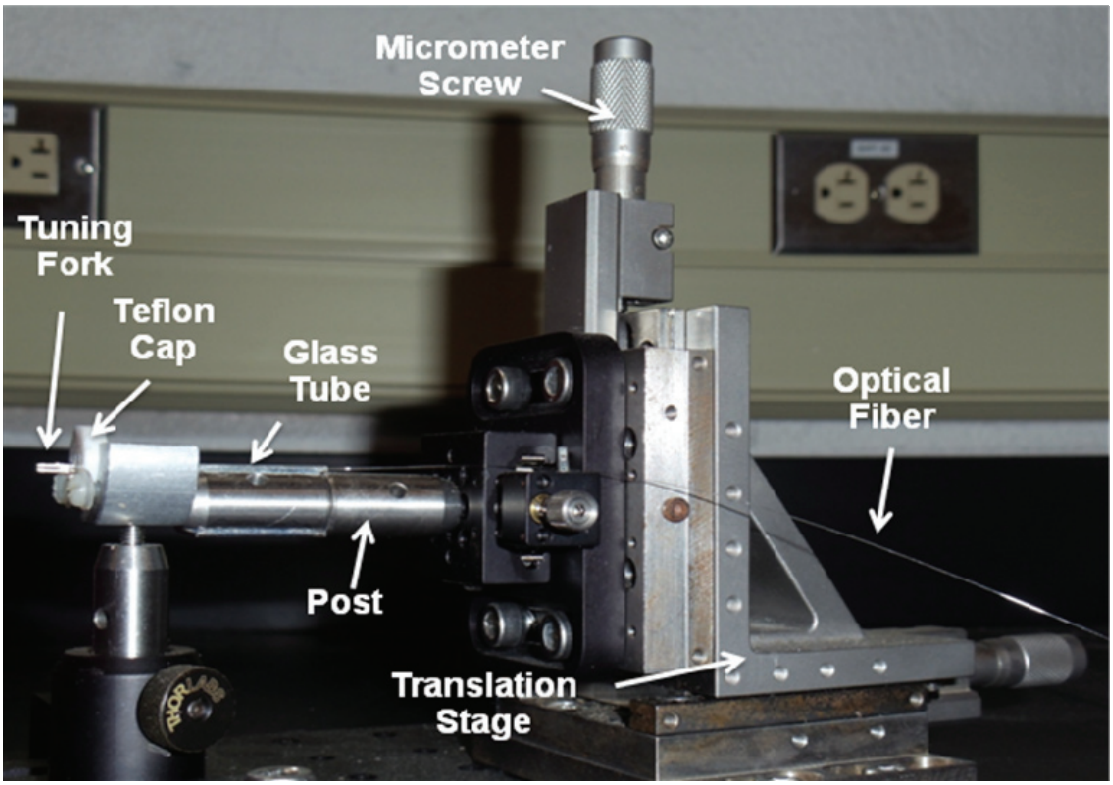

Figure 4.14: The translation stage set-up to attach the near-field fiber probe to the tuning fork.

For this procedure we use three axis translation stage and a post attached to the front of translation stage (*66*). A glass tube is glued to the top of that post, used to align the optical fiber tip through the central hole of the disk. The super glue is applied to the top of the tuning fork and the tip is lowered very slowly and gently until the two surfaces touch each other.

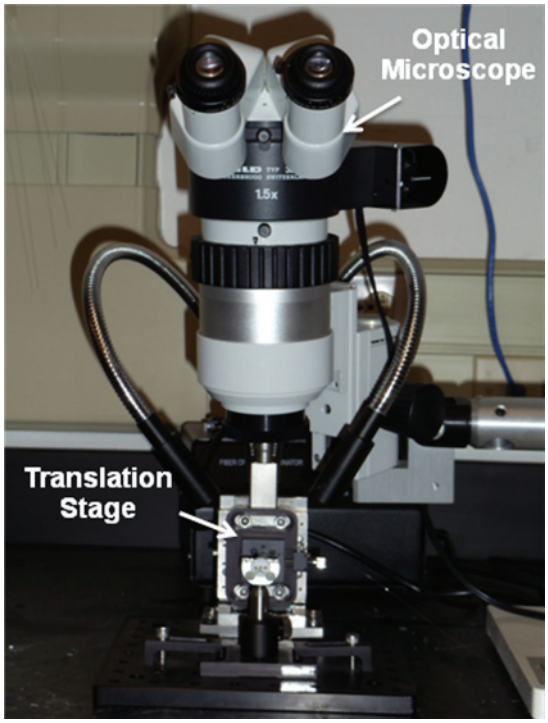

Figure 4.15: Optical microscope is used to glue the tip on the tuning fork.

The tip protrusion from the end of the tuning fork is also another important point to have a better resolution in the NSOM images (See Fig. 4.16).

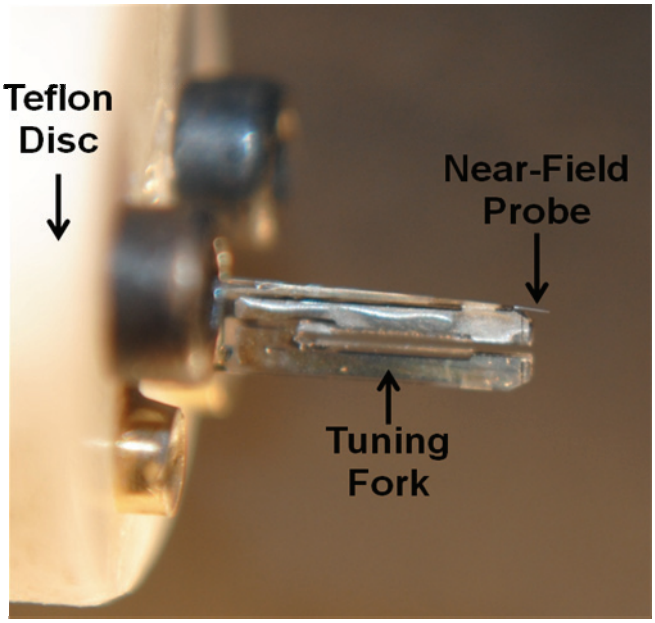

Figure 4.16: The near-field probe is glued to one leg of tuning fork.

Once the gluing process is done, we have to wait one day until the tip is strongly attached to the leg of the tuning fork.

4.2.5 Hardware/Software Response and Control System

One of the most crucial and challenging part in the design and operation part of fsPSTM was the hardware and software response and control system. National Instruments (NI) LabVIEW programming environment is used to build the software that controls the instruments (analog and digital lock-in amplifiers, NanoDrive, tip and tuning fork oscillator and z-axis motion of the nanopositioner). The data from the various instruments are sent to computer using National Instruments PCI DAQ card (model NI-PCI-6010) (Fig. 4.17).

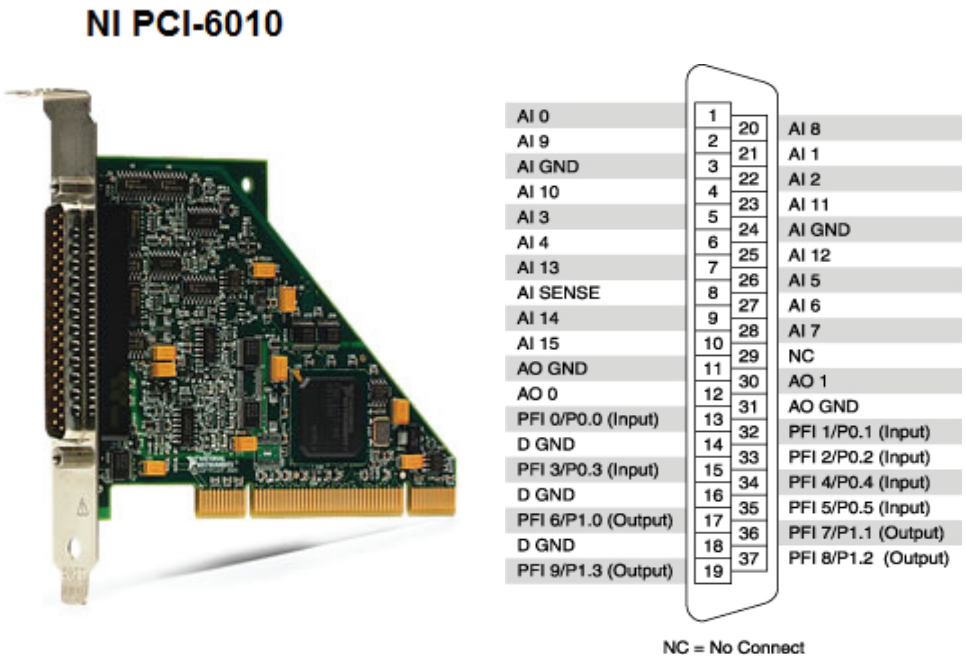

Figure 4.17: PCI DAQ card. AI connections are analog input. AO connections are analog output (*68*).

The card has several analog input and output channels, as well as digital channels which can acquire digital data or a square wave clock pulse, and a pair of channels which can generate a high frequency square wave clock pulse. The output of the analog lock-in amplifier for the tuning fork resonance amplitude is connected to analog input channel zero, with the associated ground tied to the analog channel ground. Analog input channel 1 and 7 are configured to accept another analog stream, expected to accommodate light intensity and phase data (*64*). To maintain constant tip-sample separation and a raster scan with point-by-point data acquisition Proportional-Integral-Derivative (PID) control settings are used to maintain constant tip-sample separation during the raster scan with a point-by-point data acquisition. These procedures are handled by separate procedure loops within the control program, and executed in parallel (*64*).

2 different programs have been written to implement a point by point scan of a line either in the x direction or in the y direction (Fig. 4.18 (a) and (b)).

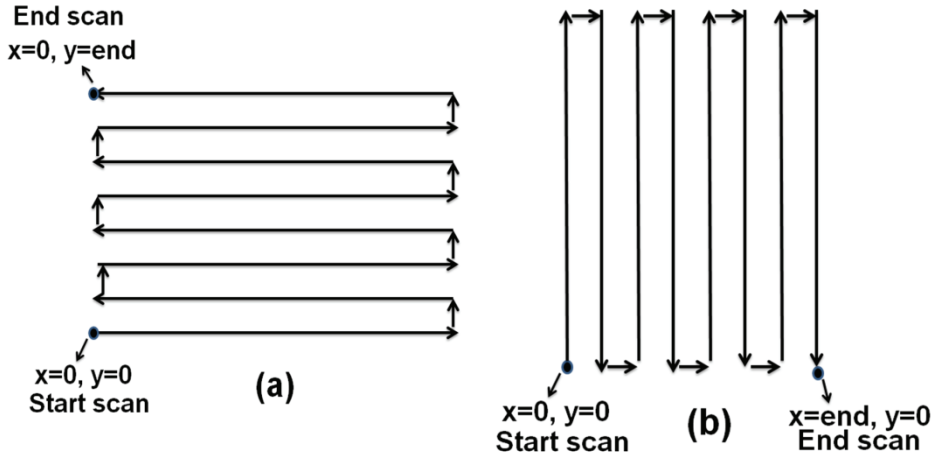

Figure 4.18: (a) Line scan along the x-direction. **(b)** Line scan along the y-direction.

During the scan, the values of position (topography scan), error, intensity (optical scan) and phase are arrayed with the position values and displayed in four graphs which are updated live, line by line. The same data is exported to a text file and each scan is saved in a separate text file (*64*).

The programs are written in a way that the tip scans the surface along the +x (the scan going from left to right only) and –x (the scan going from right to left only) directions (Fig. 4.18 (a)). If the line scan is along the y-direction (Fig. 4.18 (b)), then the data is written both for +y (the scan going from down to up only) and –y (the scan going from up to down only) scans. Of course at the end of the whole scan, labview shows both the scans together.

Depending on the symmetry of the tip and the tilt of the surface, both scans do not always perfectly overlap (Fig. 4.19). Therefore, we would like to have them splitted apart. For this procedure, we use Matlab to split the data and call the splitted ones even and odd scans.

Figure 4.19 shows the topography scan of 100 nm SiO_2 discs on Si base (Ted Pella HS-100MG). More detailed topography results will be given in the next chapter. Here we would like to emphasize the scan properties. Even-odd scan corresponds to the scans taken when the tip was moving from left to right and from right to left together. We have also shown just even and just odd scans in figure 4.19. When the tip starts scanning the surface, it first moves along the +x direction (left to right). Just odd or even rows were taken to split the data to only one direction scans.

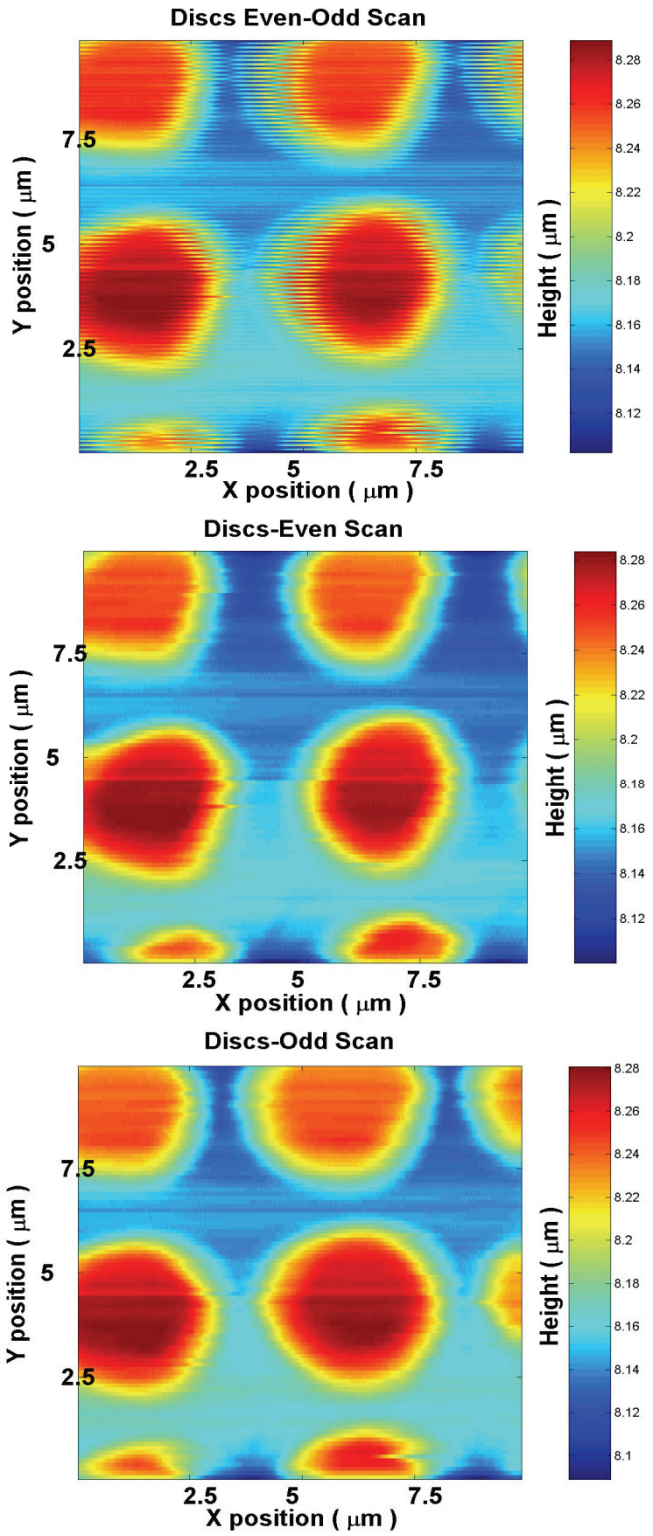

Figure 4.19: Topography scan for SiO_2 discs that have 5 μm pitch and 100 nm height. There is clear difference between even-odd scan, just even scan and just odd scan.

Therefore, at the end we have odd scans which correspond to only the movement of tip from left to right and even scans which correspond to only the movement of tip from right to left (Fig. 4.19). Slowing down the tip during the raster scan improves the scan quality and the resolution of the image. The surface tilt is also another problem to be handled. We have written our own program to correct the surface of the tilt by using rotation matrix concept.

4.3 Heterodyne Detection Scheme

The performance of the PSTM is extremely enhanced by adding the capability to detect time evolution and phase changes. The temporal and phase information can be obtained by incorporating the PSTM into a one arm of a Mach-Zehnder-type interferometer which enables heterodyne detection (*55, 56, 69-71*).

Heterodyne detection has ability to suppress the background signal and enhance the detection sensitivity of the interference signal (*72, 73*). To extract the phase of the SPP, we use acousto-optic modulator (AOM) in both arms. Basically, the AOM adds a constant to the frequency so that the outgoing light is frequency shifted. Then we employ heterodyne detection scheme in combination with a two-channel lock-in amplifier (See Fig. 4.20). For this experiment, since we are using ultrashort (50 fs) laser pulses to excite SPPs, one of the significant steps in the building period of the set-up is actually managing the pre-compensation of the dispersion caused by AOMs and near-field optical fiber. After calculating the dispersion caused by AOMs and near-field optical fiber, we

have used two prisms and a mirror which corresponds to four-prism compressor to have the negative dispersion (*74*). We have also included the same amount of single mode fiber in the reference arm to compensate the dispersion caused by near-field optical fiber (*75*). In addition, symmetric AOM configuration has been chosen specifically to have a balanced dispersion in both arms (*76*).

In this work we are interested in tracking and imaging of 50 fs SPP pulse propagation on metal thin films. The first idea and demonstration of mapping and tracking femtosecond pulse propagation in photonic structures have been released by Niek Van Hulst and Kobus Kuipers group from University of Twente using a time-resolved photon scanning tunneling microscope (PSTM) to determine phase and group velocities of femtosecond pulses in an optical waveguide (*55, 77*). For this experiment Ti:Sapphire pulsed laser with a pulse duration 300±20 fs was used. The same technique has been used by Kuipers group from Amolf Institute to directly show the existence of slow light in photonic crystal waveguides (*69*). The same group also studied ultrafast SPP propagation on a SPP waveguide (*56*) structures. For SPP propagation studies they have used Ti:Sapphire pulsed laser with a pulse duration 120 fs. Although conceptually very similar, an ultrafast PSTM has never been used to track 50 fs SPP pulses in photonic nanostructures due to the challenging nature of the experiment. Since shorter pulse corresponds to broader spectrum, dispersion compensation becomes an important issue. However, observing a 50 fs pulse propagation using PSTM is an important accomplishment and will give us critical information to determine the dispersion properties of plasmonic structures.

In our experimental set-up, the output of a 50 fs Ti:Sapphire pulsed laser (KM Labs) is divide into two beams by a beam splitter. One of the arms is called reference arm and the other one is called signal arm. A mechanical time delay stage is included in the reference arm. Inside the reference and signal arms, the two AOMs are incorporated. We drive both the AOMs at sound frequency ω_{AOM}=40 MHz. However, in the signal arm we add an additional $\Delta\omega$=20 KHz frequency more than reference arm (Fig. 4.20).

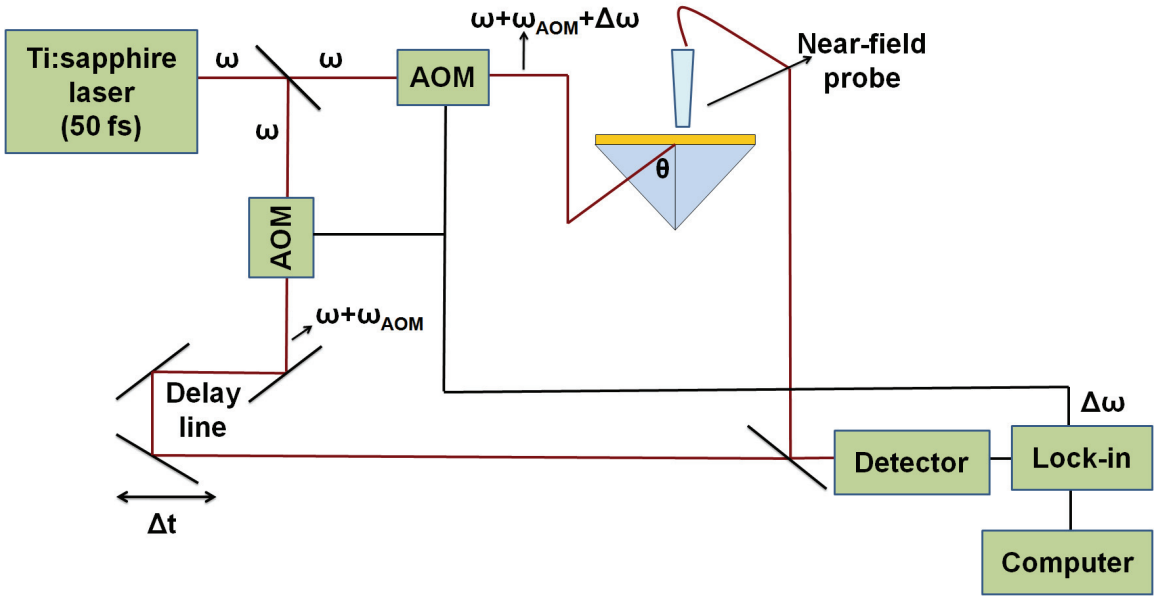

Figure 4.20: Heterodyne detection scheme. AOMs are driven by Dual Channel Frequency Driver with ω_{AOM}=40 MHz. The reference arm has frequency $\omega_{ref}=\omega+\omega_{AOM}$ where ω is the frequency of laser. Since we want frequency difference between both arms, we drive the signal AOM in a way that it has $\omega_{SP}=\omega+\omega_{AOM}+\Delta\omega$, where $\Delta\omega$=20 KHz. The net effect is that the signal beam has a frequency which is 20 KHz larger than the reference frequency.

The signal beam excites the SP pulses on a metal surface in a prism configuration. The SP pulse is picked up by an optical near-field fiber which can move in the x, y and z directions. Using the feedback loop to scan the tip over the

structure at a constant tip-to-sample distance, the intensity distribution of the propagating wave and the topography of the sample are recorded with high, typically 100 nm, spatial resolution. In addition, interferometrically mixing the extracted pulse with the reference one, allows tracking the phase and the time evolution of the SP pulses. Therefore, the light from the reference arm and signal arm are interferometrically mixed and the interference signal is collected by using a detector. The detector sends the signal to lock-in which process and send it to the computer. As a conclusion, the combination of modulation and lock-in technique allows simultaneous acquisition of phase and amplitude of the SP field. The propagation of the SP pulse is visualized by scanning the near-field probe at different time delays Δt (*56*).

Electric fields are described by the following equations:

$$E_{ref} = E_{ref}(t)\, e^{i\left[w_{ref} t - kx_{ref} + \phi_{ref}\right]} \quad (15a)$$

$$E_{SP} = E_{SP}(x, y, (t-\tau))\, e^{i\left[w_{SP}(t-\tau) - kx_{SP} + \phi_{SP}(x,y)\right]} \quad (15b)$$

$$w_{ref} = w + w_{AOM} \quad (16a)$$

$$w_{SP} = w + w_{AOM} + \Delta w \quad (16b)$$

$$\text{Where } w_{AOM} = 40\,\text{MHz} \text{ and } \Delta w = 20\,\text{KHz}$$

$$x_{SP} = x_{ref} + \Delta x \quad (17)$$

$$E_{SP} = E_{SP}(x, y, (t-\tau))\, e^{i[(w_{ref} + \Delta w)(t-\tau) - k(x_{ref} + \Delta x) + \phi_{SP}(x,y)]} \quad (18)$$

$$\phi_{rel} = \phi_{ref} - \phi_{SP}(x,y) \quad (19)$$

$\phi_{rel}(x,y)$ is the relative phase difference between the reference arm and the signal arm.

$$E_{SP} = C * E_{SP}(x,y,(t-\tau))\, e^{i\left[w_{ref} t - kx_{ref} + \phi_{ref}\right]} \times e^{i\left[\Delta w t - k\Delta x - \phi_{rel}(x,y)\right]} \quad (20)$$

where $C = e^{-i[(w_{ref} + \Delta w)\tau]}$ is a constant;

The measured lock-in signal is the product of the electric fields of reference and signal arm.

$$I = \left|E_{ref} + E_{SP}\right|^2 = I_{ref} + I_{SP} + E_{ref}E_{SP}^{*} + E_{SP}E_{ref}^{*} \quad (21)$$

$$I = I_{ref} + I_{SP} + 2E_{ref}E_{SP}\cos\left[k\Delta x - \Delta w t + \phi_{rel}(x,y)\right] \quad (22)$$

Essentially, lock-in amplifier takes the Fourier Transform (FT) of the detector output signal. In that case the first two terms cancel out and the output of the lock-in will be sensitive only to the cross term and the detected signal will depend on Δω (see eqns. 23 and 24) (*56*). From there, we can easily extract the amplitude and phase information of SP pulses.

$$I_1(x,y) \propto \cos(\phi_{rel}(x,y)) \int_0^T E_{ref(t)} E_{SP}(x,y,t-\tau)dt \quad (23)$$

$$I_2(x,y) \propto \sin(\phi_{rel}(x,y)) \int_0^T E_{ref(t)} E_{SP}(x,y,t-\tau)dt \quad (24)$$

Here T is the time constant for the lock-in. We are using $\Delta\omega$=20 kHz as a reference frequency which corresponds to 5×10^{-5} second for our experiment. We have chosen T=100 msec=10^{-1} sec and it is much bigger than 5×10^{-5} sec.

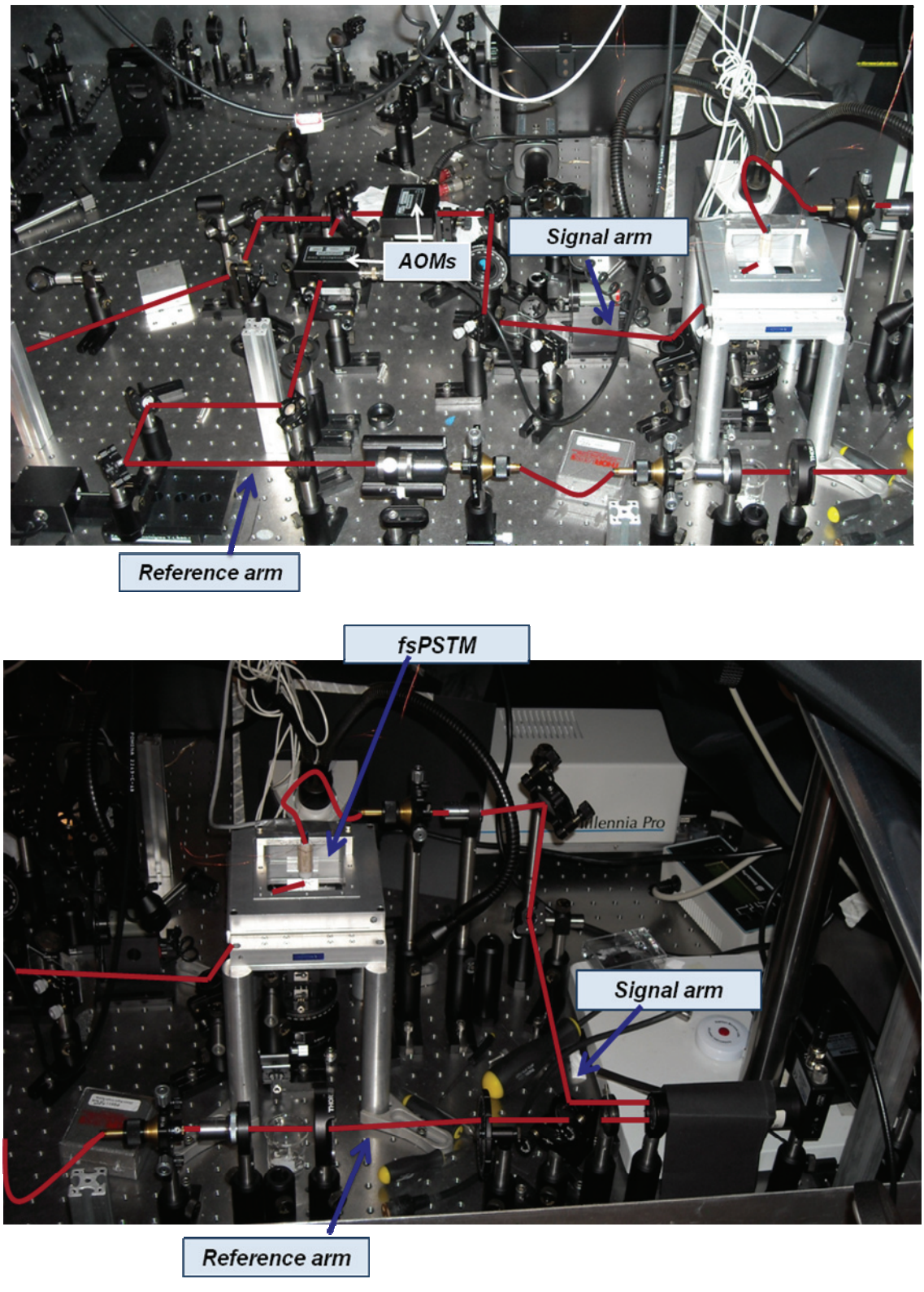

Figure 4.21: Heterodyne detection system with fsPSTM.

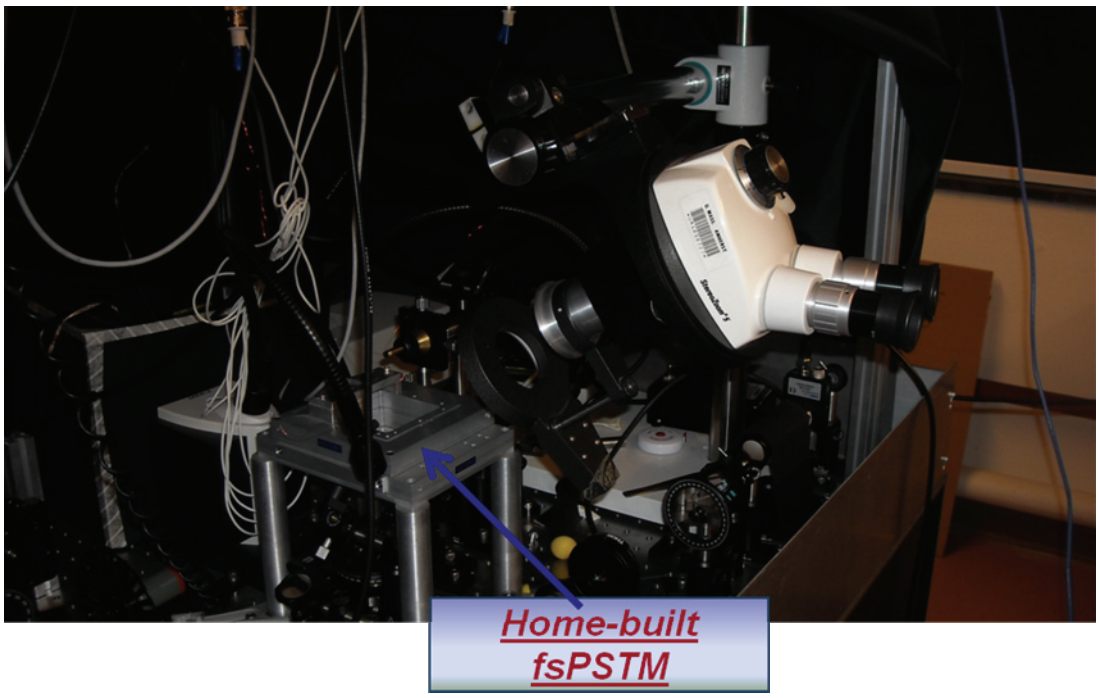

Figure 4.22: Home-built fsPSTM.

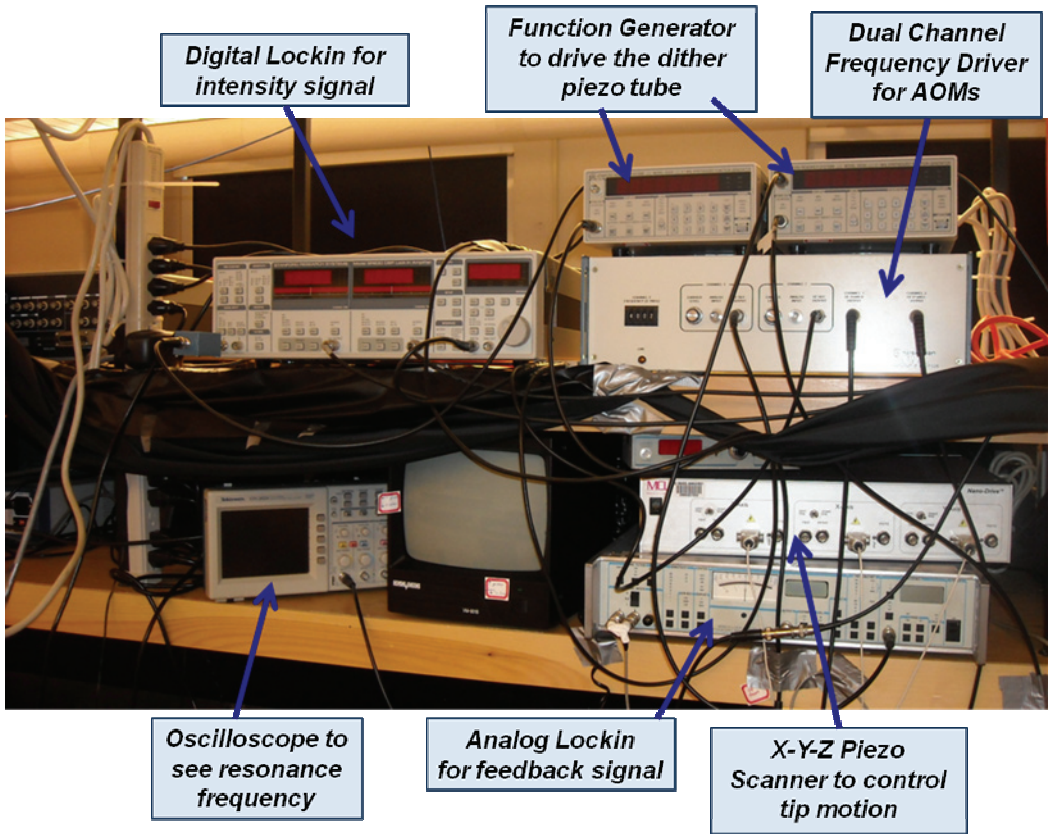

Figure 4.23: The necessary electronics to run the fsPSTM.

4.4 Stabilizing the Microscope and the Signal

Another challenging part of the complete set-up is stabilizing the signal and phase against the air drift and vibrational effects. The set-up environment plays a crucial role in the signal quality of the experiment. Since we are extracting the light coupled to near-field tip, we do not want to have amplitude changes in the detected signal. To get rid of the air drift, we have covered the complete setup with boxes made out of Perspex. These boxes are useful to protect the interferometer against drafts and improve the stability of the signal and the phase. To control the damping caused by optical table, we have built the set-up on Newport Stabilizer High Performance Laminar Flow Isolator. Additionally, the whole set-up and microscope have been specifically built in the basement of the physics department at University of Massachusetts Amherst to reduce the effects of vibrations on the experiment.

4.5 Summary

We have built a new, modified form of NSOM known as fsPSTM to study the propagation and dispersion properties of ultrafast 50 fs surface plasmon pulses in photonic structures. Incorporating the fsPSTM into a Mach-Zehnder interferometer, allowing heterodyne detection system, we are able to get amplitude and phase information of SPP pulses in space and time.

Despite the beauty of the experiment and the valued information that can be obtained by it, there are only a few time-resolved PSTMs in operation worldwide to study light propagation in photonics and plasmonic structures. The

outstanding groups that are recently working on heterodyne time-resolved PSTM are:

1. The group of Prof. Dr. Niek Van Hulst from ICFO Barcelona, Spain.
2. The group of Prof. Dr. L. (Kobus) Kuipers at FOM Institute AMOLF, Amsterdam, Netherlands.
3. The group of Prof. Dr. Yeshaiahu Fainman at University of California, San Diego
4. The group of Prof. Dr. Jennifer Herek and Dr. Herman Offerhaus from University of Twente, Netherlands.

The reason for the few number of operating time-resolved PSTMs in the whole plasmonics field is because of the complexity of the experiment which requires expertise in different fields such as near-fields, optics and electronics. Noise and drift are the most challenging problems for this kind of set-up. Especially working with 50 fs laser pulses makes the experiment much more challenging because of dispersion effects.

Our fsPSTM is one of a few time-resolved PSTMs that has been built and used in the plasmonics research field to visualize ultrafast surface plasmon pulses in photonic nanostructures.

CHAPTER 5

TESTING THE FEMTOSECOND PHOTON SCANNING TUNNELING MICROSCOBE (fsPSTM)

5.1 Results for Topography Images

After developing the fsPSTM, many test scans were performed by using HS-Series AFM calibration sample to check the z-axis feedback system and to get topography images. The HS-series sample has SiO_2 structures with 100 nm height on Si base (see Fig. 5.1). Arrays of structures with different shape and pitch are integrated on the chip. The larger square of 1 x 1mm^2 contains square discs and holes with a 10μm pitch. The smaller center square of 500 x 500 μm^2 contains circular discs and holes as well as lines in both X- and Y-direction with a 5 μm pitch (Fig. 5.2).

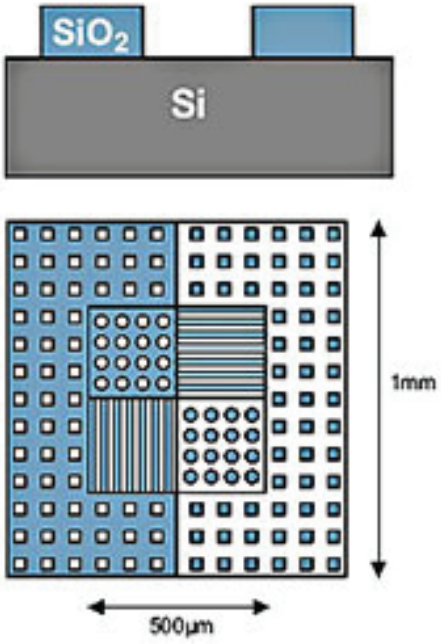

Figure 5.1: HS-Series AFM calibration sample. (source Ted Pella Inc.)

We scanned the holes and discs of smaller center square by doing 10 μm x 10 μm scan in X- and Y- direction. From Fig. 5.3 and Fig. 5.4, we can see 5 μm pitch between holes and discs.

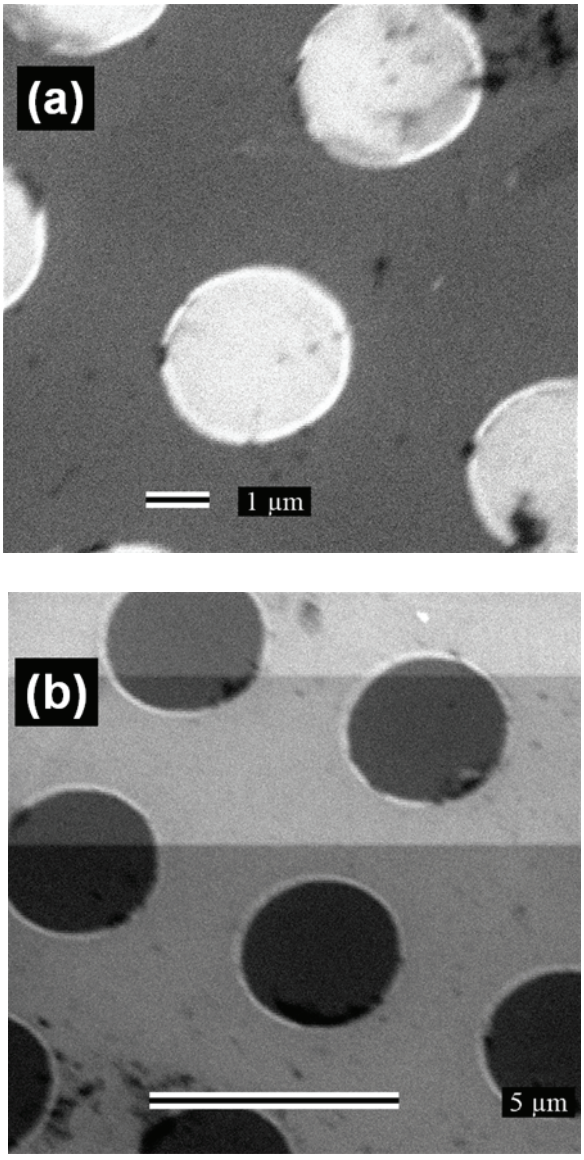

Figure 5.2: SEM images of SiO_2 **(a)** disc and **(b)** holes on Si base. The pitch between two following holes and discs is ~ 5 μm and the size of the holes and discs is ~ 3 μm.

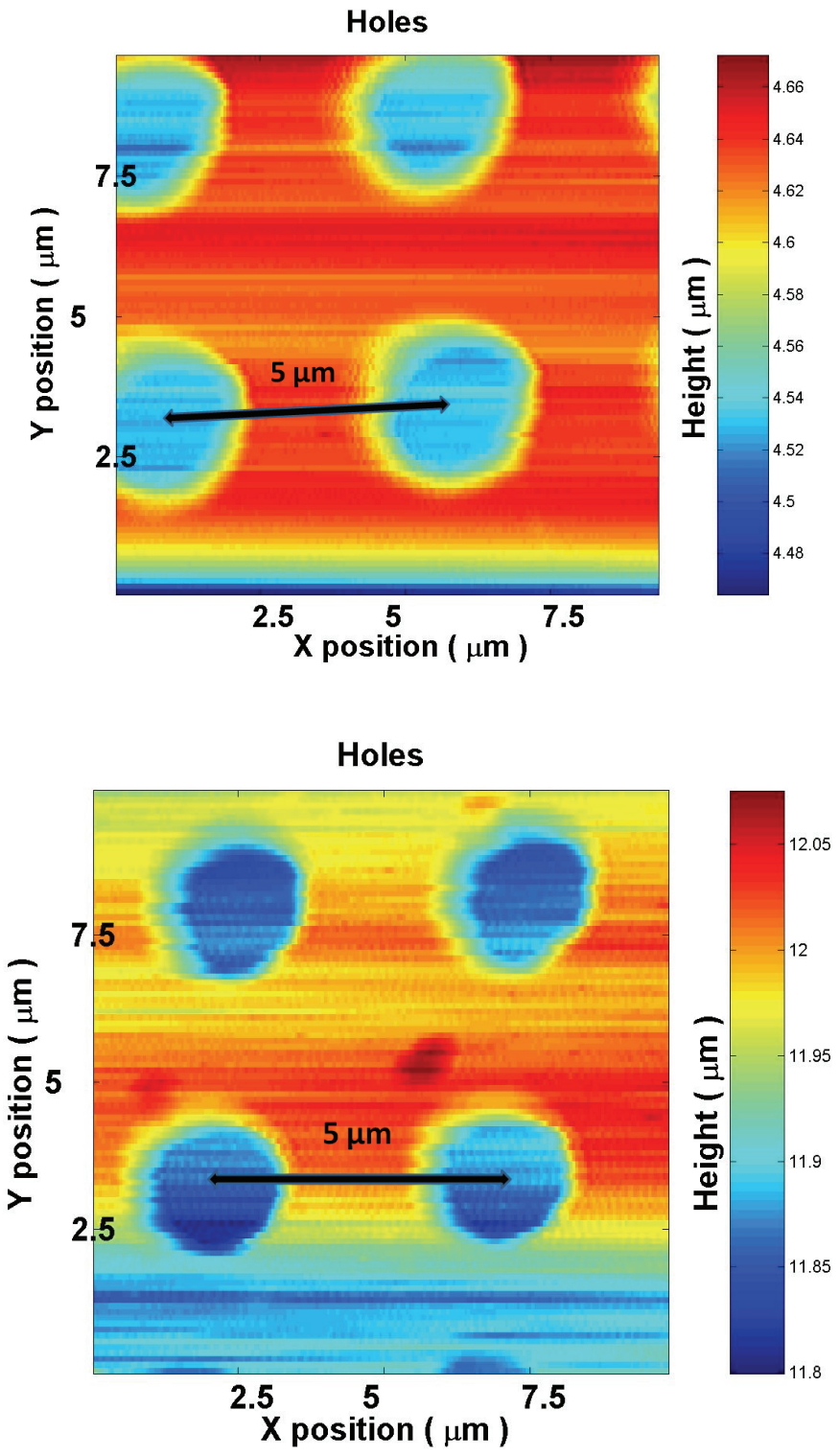

Figure 5.3: Topography images of SiO_2 holes on Si base taken by fsPSTM.

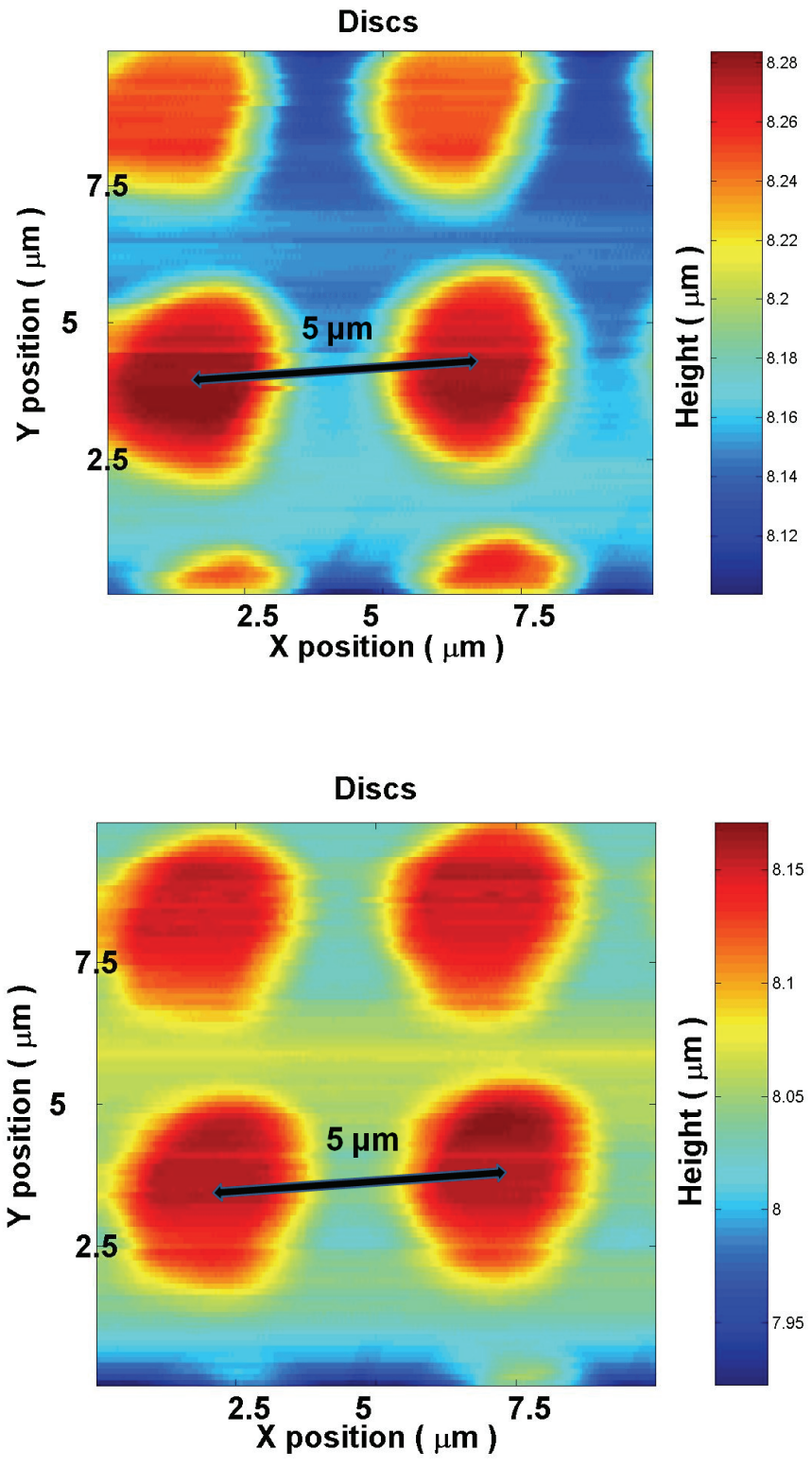

Figure 5.4: Topography images of SiO_2 discs on Si base taken by fsPSTM.

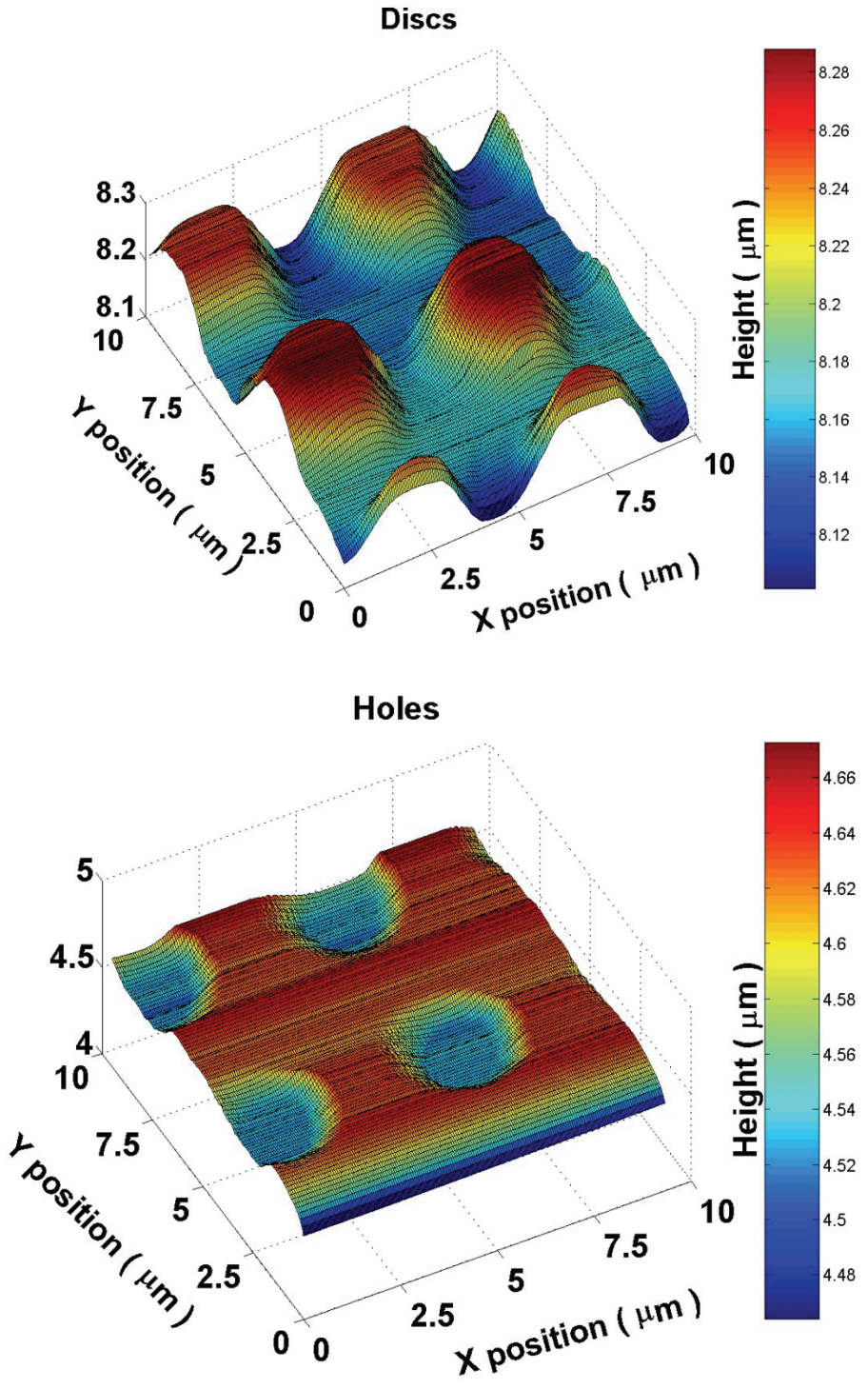

Figure 5.5: 3-dimensional topography images of SiO_2 discs and holes on Si base (data is taken by fsPSTM).

The height of discs and holes can be seen from Fig. 5.5. However, to see the step height clearly in scan results, the data is analyzed by taking the cross section of the images. From Fig. 5.6, we can clearly see ~ 110 nm step height. It also gives us idea about the pitch between the two following holes and discs (~ 5 μm).

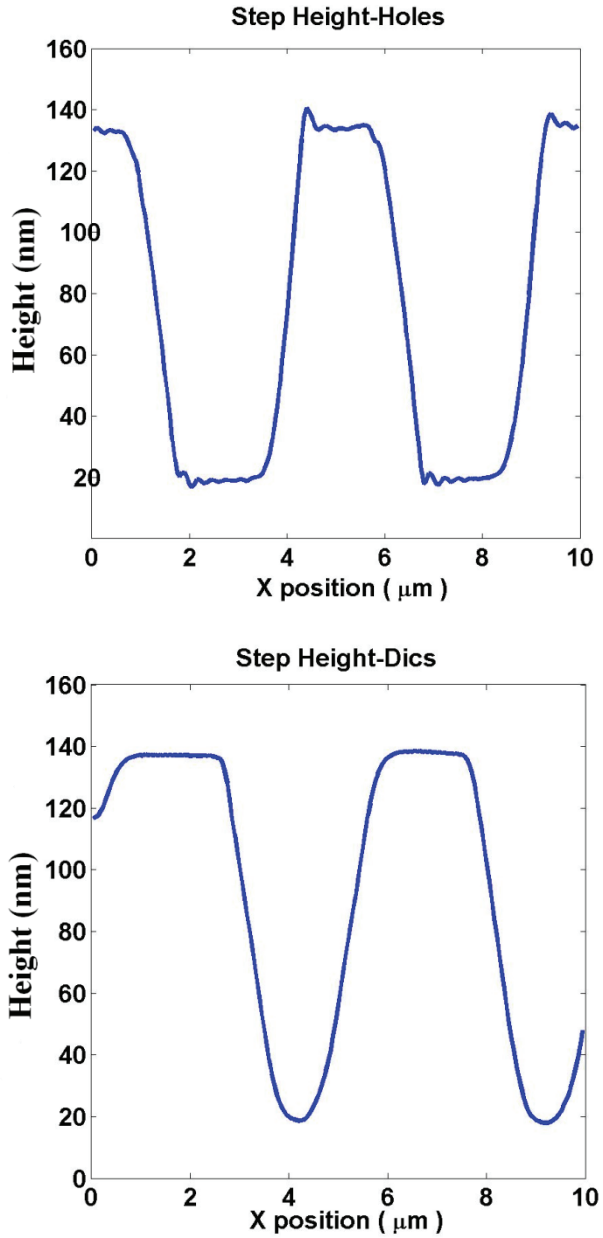

Figure 5.6: The step height of our scan results.

Although SiO_2 discs and holes on the AFM sample have the same diameter (~ 3 μm), fsPSTM topography scans reveal the diameter of the discs bigger than the diameter of the holes (Fig 5.3 and 5.4) because of the finite size of the near-field probe.

We have also done characterizations on SPP waveguides; therefore we have done topography scans on gold SPP waveguide structures as well (Fig. 5.7). SPP waveguide fabrication is done by Mark T. Tuominen group in Department of Physics at University of Massachusetts Amherst.

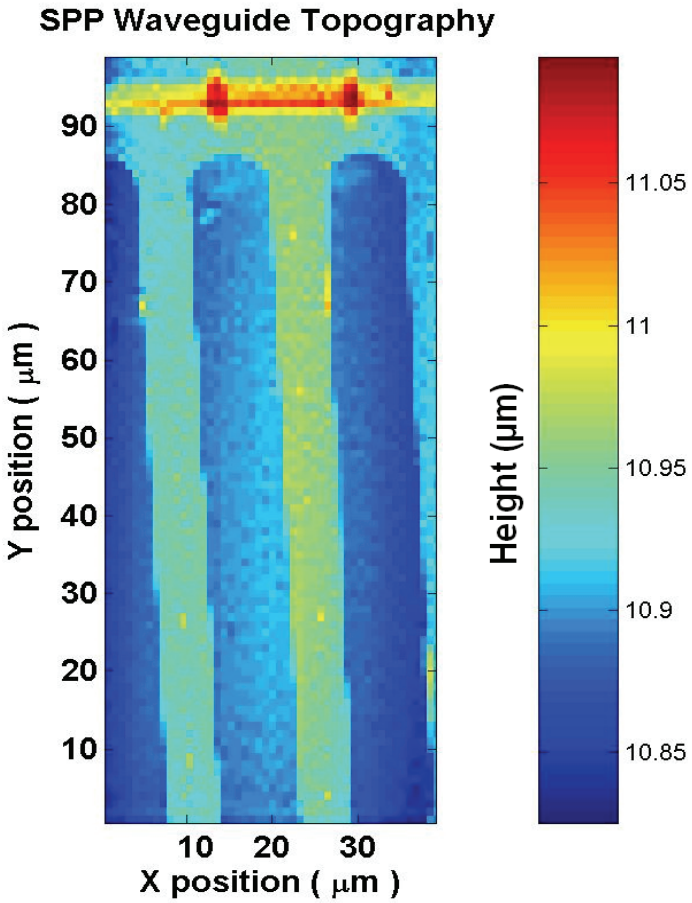

Figure 5.7: Topography images of ~ 40 nm thick and ~ 6 μm wide, gold SPP waveguides.

5.2 Results for Optical Images

After the test scans for topography of the sample, we moved on to our actual experiments, tracking and imaging of 50 fs SPP pulses on ~ 50 nm gold thin films by performing 100 μm x 100 μm scans in X- and Y- direction to get optical images. Before performing the time-resolved measurements, we have done time averaged NSOM scan by blocking the reference arm and just using signal arm (no interference). A mechanical chopper in the signal arm is used to modulate the signal for lock-in detection. At the end of this experiment, we captured the laser spot with a size ~ 100 μm on our sample (Fig. 5.8).

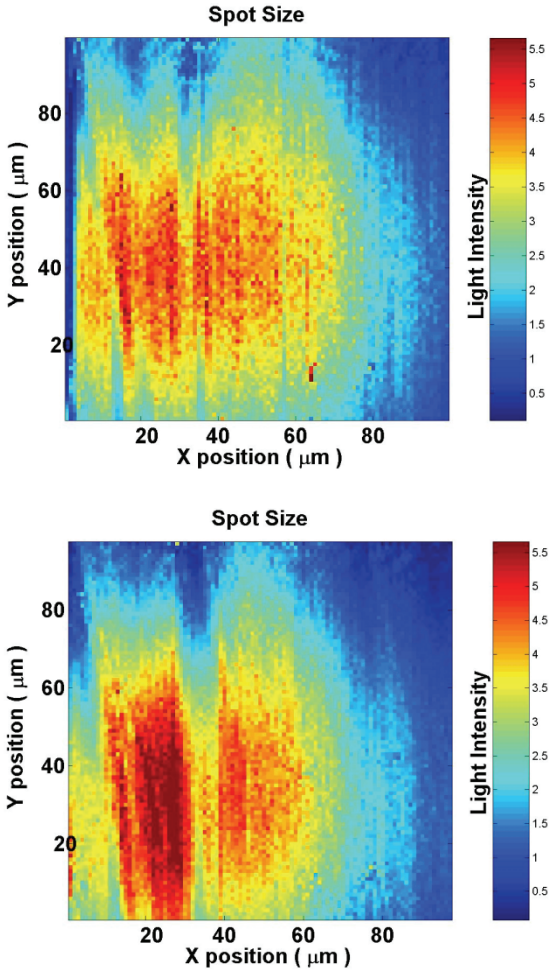

Figure 5.8: Time averaged NSOM scan. The spot has a size ~ 100 μm.

Although we worked on our objective lens (focal length=30 mm) to focus the beam much smaller size, using one inch prism resulted in a limited working distance (See Fig. 5.9), therefore, it was not simply possible to improve the spot size to much smaller, desired value ~ 20 μm.

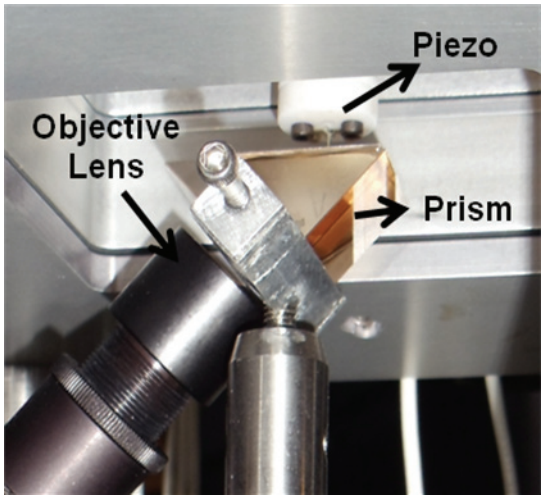

Figure 5.9: The limited working distance around the prism.

For extended thin film characterizations, having a large spot was not creating a big problem; therefore we preferred to keep the set-up as it is until finishing the characterizations on gold extended film. However, for SPP waveguide studies, we are aware that it is very important to have a well focused laser spot just outside of the funnels to excite the SPPs and guide those using SPP waveguides. Our time averaged images taken for SPP waveguides revealed beating effect because of large spot (Fig. 5.10).

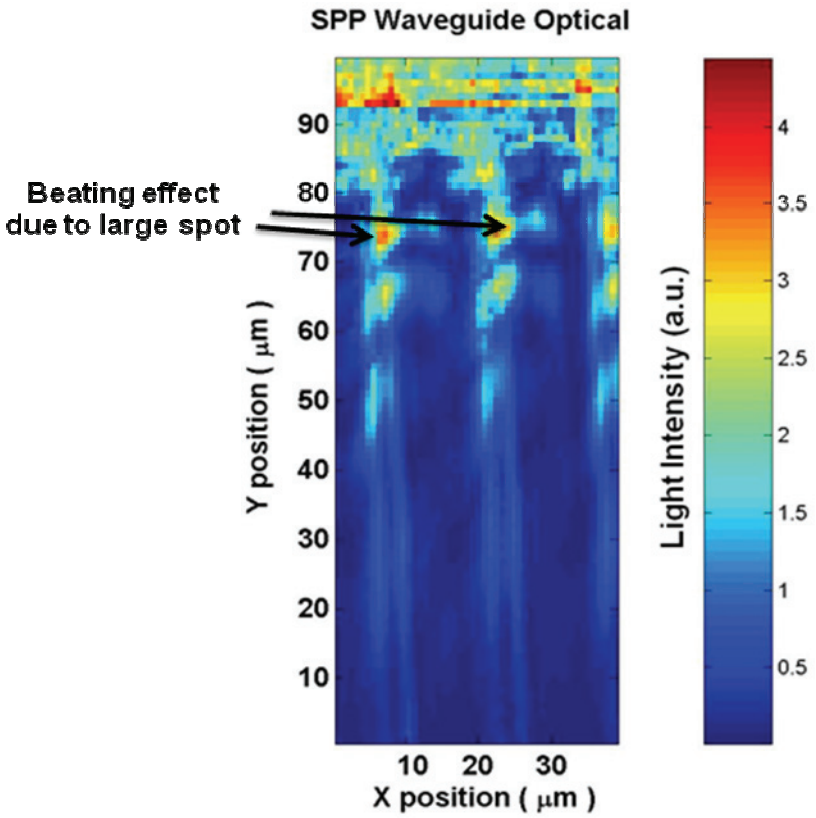

Figure 5.10: Time averaged NSOM scan of SPP metallic waveguides. The scan range is 40 μm x 100 μm.

One reasonable solution for large spot size can be using grating coupling instead of prism coupling to excite the ultrafast SPPs. For thin extended film characterizations we didn't need to modify the set-up, therefore we maintained prism coupling excitation. However, for SPP waveguide studies it will be more efficient to modify the set-up and use grating coupling.

5.3 Time-Resolved Measurements to Visualize Ultrafast Surface Plasmon Pulses Using 50 fs Laser Pulses

5.3.1 Extended Thin Film Characterizations

For time resolved experiments, heterodyne detection scheme is performed with acousto-optic modulation in both arms by using two channel lock-in amplifier (Fig. 5.11). The signal arm (50 fs laser pulses) excites the ultrafast surface plasmon polaritons (SPPs) on the extended thin gold film (~ 50 nm thick), and the sub wavelength fiber probe picks up the evanescent field of propagating surface plasmon wave. The mechanical delay stage in the reference arm is used to capture the interference between two arms.

In the case of a pulsed laser source, interference only occurs when the reference and signal pulse temporally overlap (Fig. 5.11). Seeing the interference is one of the hardest steps in this experiment. Especially, working with 50 fs pulses and using bulk optics makes the experiment much more challenging. In the building part of the experiment, we have tried to use wide band coupler to increase the interference efficiency of the set-up. However the extreme sensitivity of the wide band coupler made experiment much more difficult. A slight touch of the fiber was changing the phase and intensity coupled to the fiber drastically. Since for this experiment, controlling the phase is one of the trickiest jobs, we decided to use beam splitter plate to interfere the both arms (*75*) (Fig. 5.11).

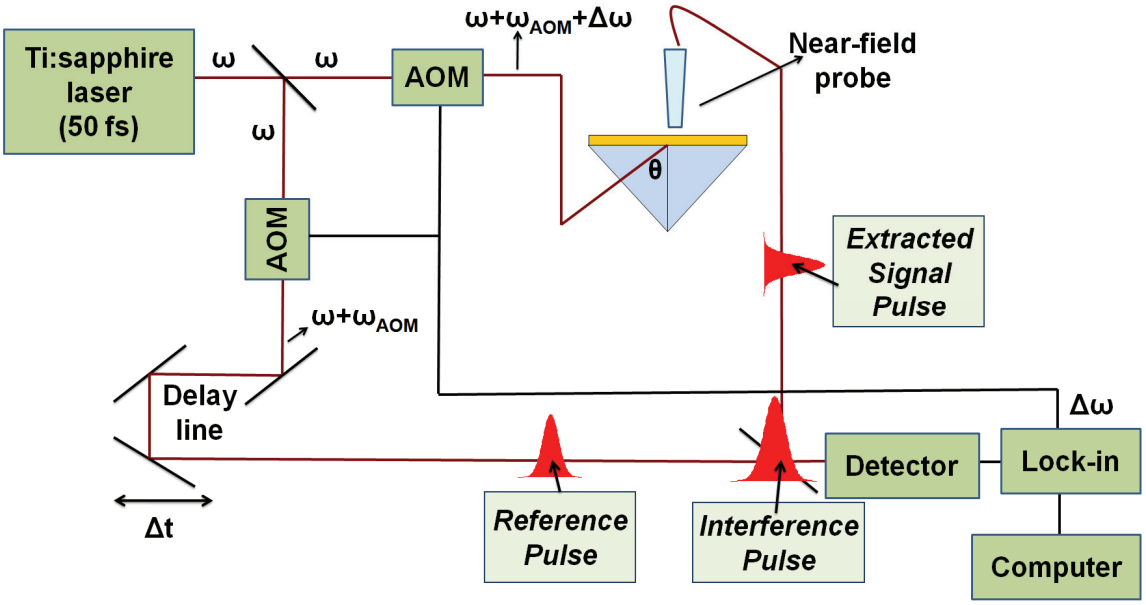

Figure 5.11: Schematic of the heterodyne detection system that shows the interference of reference and signal pulse.

The overlap of the two pulses (reference and signal pulse) can be arranged using the delay line incorporated in the reference arm. The interference signal is captured in the following way:

The signal arm is used to excite the ultrafast SPPs on the thin extended gold film and the evanescent wave of SPPs is coupled to near-field tip. In that case the probe is kept fixed on the sample and the delay line is moved to arrange the time overlap of the reference and signal pulses. Once the two pulses from reference and signal arm overlaps temporally, the lock-in shows a pick in the amplitude data which is the signature of interference signal. In Fig. 5.12, we have shown the captured interference signal (red dotted line) in our experiment. The gaussian fit to the data gives us the FWHM of the interference signal which is ~

22.6 μm. This FWHM corresponds to 75 fs pulse duration in the time domain due to finite speed of light.

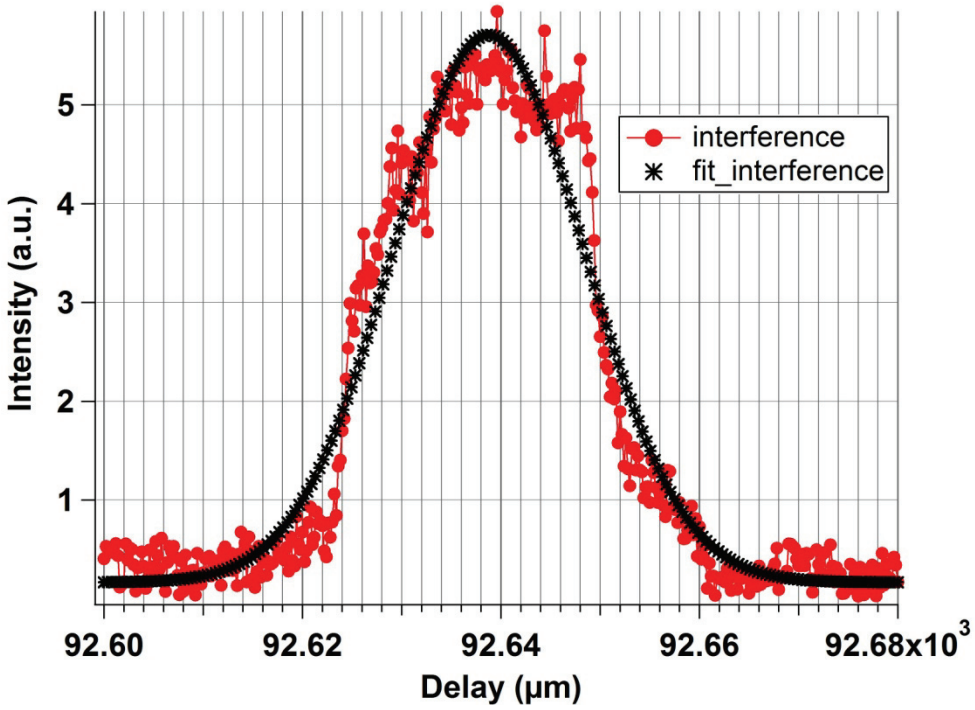

Figure 5.12: Interference signal that corresponds to the temporal overlap of the reference and the signal arms. Delay (μm) corresponds to the length difference between the reference and signal arms.

Fig. 5.12 is also known as temporal cross-correlation of two independent optical pulse in the signal and reference branches (*55, 76*). We have also taken our Ti:Sapphire laser spectrum in the same day that we have seen interference of both arms (Fig. 5.13). The FWHM of the laser spectrum is 25.8 nm and using the time bandwidth product of 0.44 in the pulse width calculation, we get ~ 39 fs pulse duration and 55 fs auto-correlation pulse duration as a lowest limit in the case of no dispersion effect. However, we know that laser pulse has some dispersion effects itself due to the possible deviations from perfect alignment.

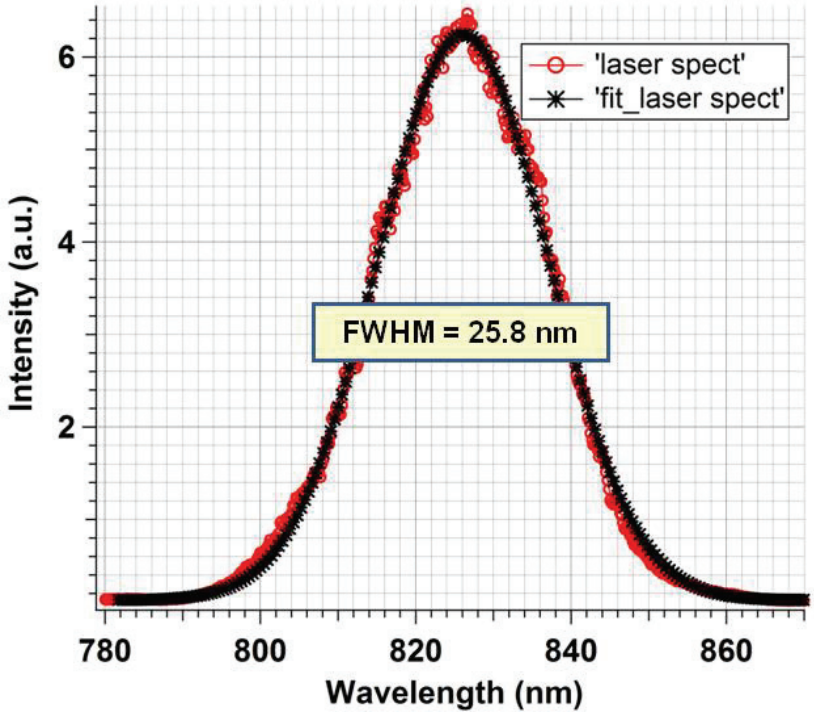

Figure 5.13: Optical spectrum of Ti:Sapphire oscillator. The FWHM of 25.8 nm spectral bandwidth corresponds to ~ 39 fs pulse duration in the case of no dispersion.

Another measurement scheme is fixing the delay stage and performing near-field point by point raster scan over the sample surface. Since we have determined the interference between the reference and signal arm using the delay line, the stage is adjusted to that position and the tip is scanned over the surface of thin extended gold film. In this measurement scheme, the tip is scanned at a fixed time delay to map the position of plasmon pulses in the gold film.

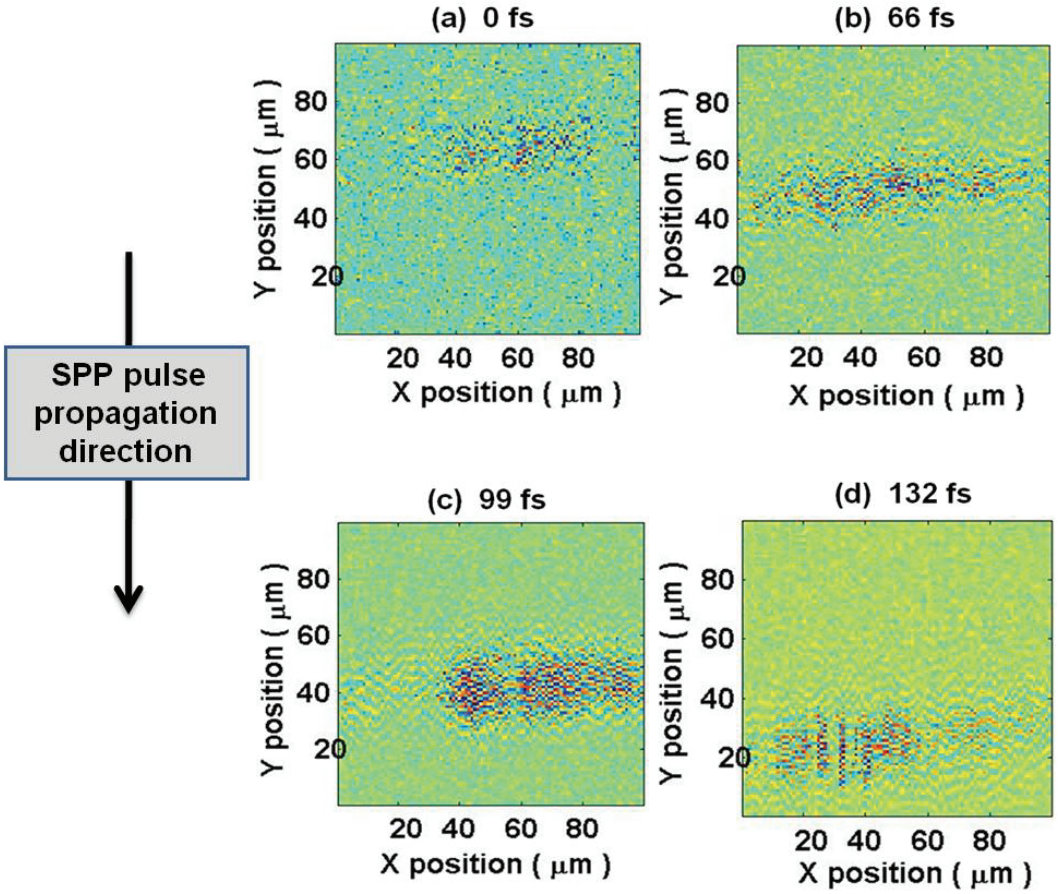

Figure 5.14: Snapshots of femtosecond surface plasmon pulse propagation on a thin extended gold film (X data). SPP pulse is propagating along the –y direction. Reference arm is increased 10 μm in between each frames of (b)-(c)-(d). From (a) to (b) reference arms is increase 20 μm. Scan frame is 100 μm x 100 μm.

Then the path length of reference arm is increased and the tip is scanned over gold film surface to observe the surface plasmon pulse evolution in space and time (see Fig. 5.14 and Fig. 5.15). Since we are increasing the reference arm using delay line, the signal arm should also increase to satisfy the temporal overlap of both pulses. Additionally, in the signal arm, SPPs are propagating over the surface of the gold film. Therefore, heterodyne detection scheme allows us to

track phase and time evolution of ultrafast SPP pulses. In our experiments, near-field scans for different time delays are done in a100 μm x 100 μm area.

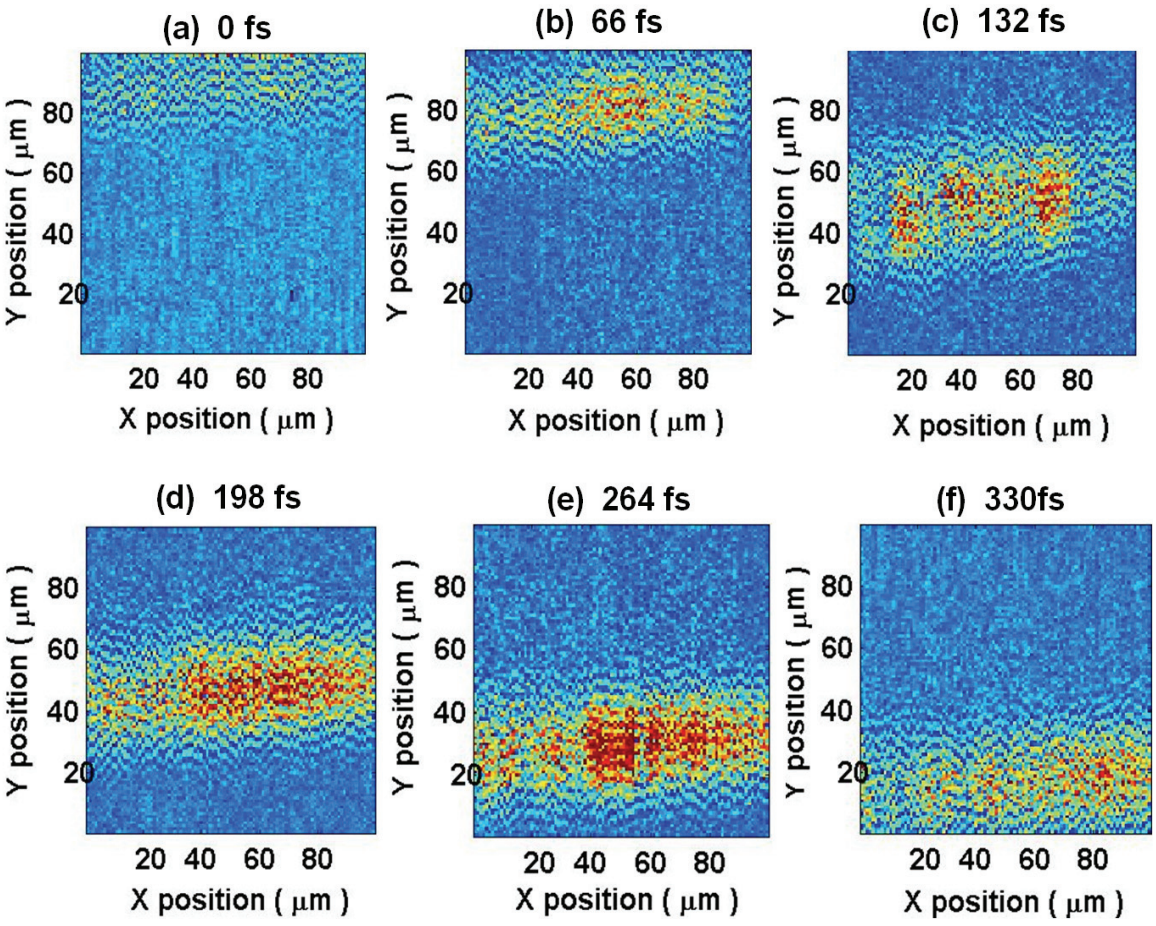

Figure 5.15: Snapshots of femtosecond surface plasmon pulse propagation on a thin extended gold film (Amplitude data). Scan frame is 100 μm x 100 μm and scan is line scan is taken along the y direction. Reference arm is increased 20 μm in between the each frames.

Fig. 5.14 corresponds to the $A\cos(\Phi_{rel})$ where A is the amplitude of intensity signal detected by lock-in and Φ_{rel} is the relative phase between reference and signal arm. Fig. 5.15 corresponds to amplitude of the detected

signal. When pulsed lasers are used in heterodyne detection system with fsPSTM, the time resolved measurements represents the pulse evolution in space and time (*55*). Therefore, Fig. 5.14 and Fig. 5.15 correspond to SPP pulse evolution in different time delays on thin extended gold film. SPP pulses are propagating along the –y direction.

To see the evolution of the envelope of the SPP pulse, we need to define the position of the pulse envelope along the propagation direction for different delay times. Therefore, 10 data columns at the center of the pulse envelope were averaged and plotted for every delay time (See Fig. 5.16).

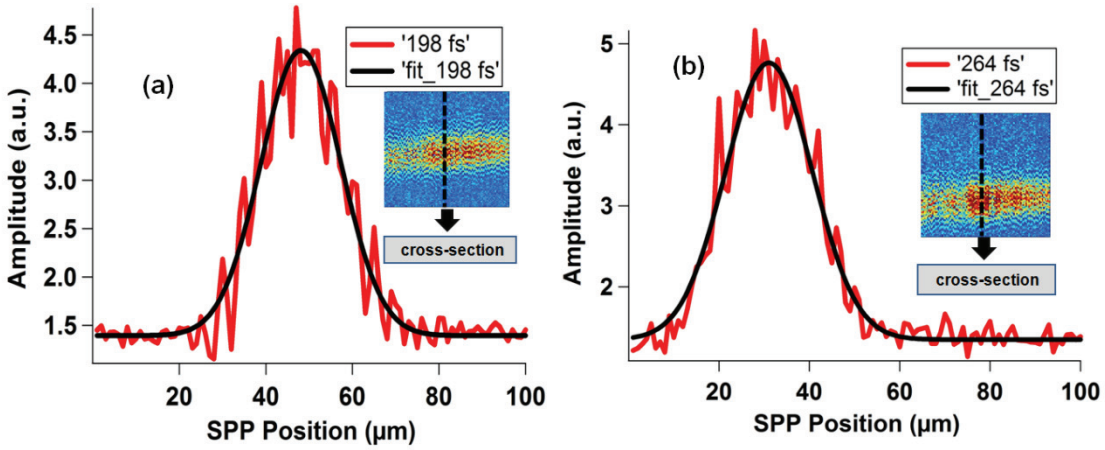

Figure 5.16: The average cross-section of Amplitude data (red line) and gaussian fit (black line) to amplitude data of the interference signal for **(a)** 198 fs and **(b)** 264 fs. The FWHM of the gaussian fits are ~ 72 fs and 75 fs respectively.

The gaussian fits to the amplitude data gives us the position of the pulse envelope. Repeating the same fitting procedure to the amplitude data for different delay time gives us the pulse evolution. To see the evolution of SPP pulse envelope, the gaussian fits for different time delays were plotted in the same

graph (See Fig. 5.17). As we can see from Fig. 5.17, SPP pulse is moving with a constant group velocity. However, the possible reason of the increased group velocity for the data point that corresponds to 132 fs, can be a backlash from the delay line.

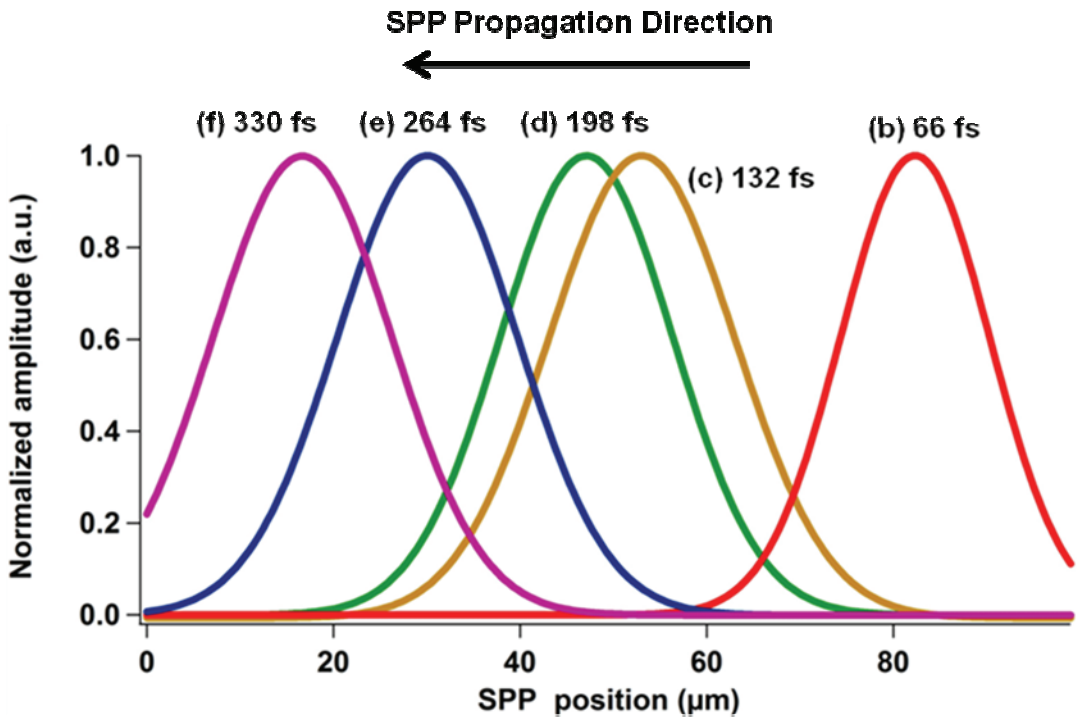

Figure 5.17: The Gaussian fit to the time-resolved Amplitude data. SPP pulse propagation is for different delay lines. Reference arm is increased 20 μm in between the each frames.

Comparing the FWHM of the temporal cross-correlation (~ 75 fs) and auto-correlation spectrum (~ 55 fs) reveals the broadening ~ 27 % due to dispersion effects because of using AOMs and optical waveguide in our set-up. Recently this concept has also been discussed by Yeshaiahu Fainman group using CW broad band optical sources (*76*).

On the other hand, the advantage of symmetric AOM and optical waveguide configuration in the heterodyne fsPSTM system is the balanced dispersion effect in both (reference and signal) arms of the Mach-Zehnder interferometer. We confirmed this analogy by comparing the FWHMs of the time-resolved amplitude data (fixed delay stage, scanning probe; see Fig. 5.17) and the FWHM of temporal cross-correlated data (fixed probe, scanning delay stage; see Fig. 5.12). The FWHMs of the time-resolved amplitude data for different delay lines are ~ 75 fs. This result matches very well with the FWHM of the temporal cross-correlation spectrum which is ~ 75 fs, confirming the balanced dispersion in our heterodyne detection system between reference and signal arms due to symmetric AOM and optical fiber configurations (see Fig. 5.11). This ~ 75 fs cross-correlated pulse width gives us ~ 53 fs laser and SPP pulse width in both arms, thus confirming that we are tracking ~ 50 fs SPP pulses in our heterodyne fsPSTM system.

One another possible and useful calculation is extracting the group velocity of ultrafast SPP envelope during the propagation over thin extended gold film. Since the position of the SPP pulse envelope is defined in Fig. 5.17, SPP pulse propagation is plotted as a function of delay (See Fig. 5.18). The error bars are included. Since the position of the pulse is partly in the scan area for the first data (0 fs) in Fig. 5.14 (a), the error bar is much bigger for this data point. The slope of the fitted line in Fig. 5.18 gives us the group velocity of the SPP pulse on the gold extended film of ~ 2.831±0.034 x 10^8 m/s.

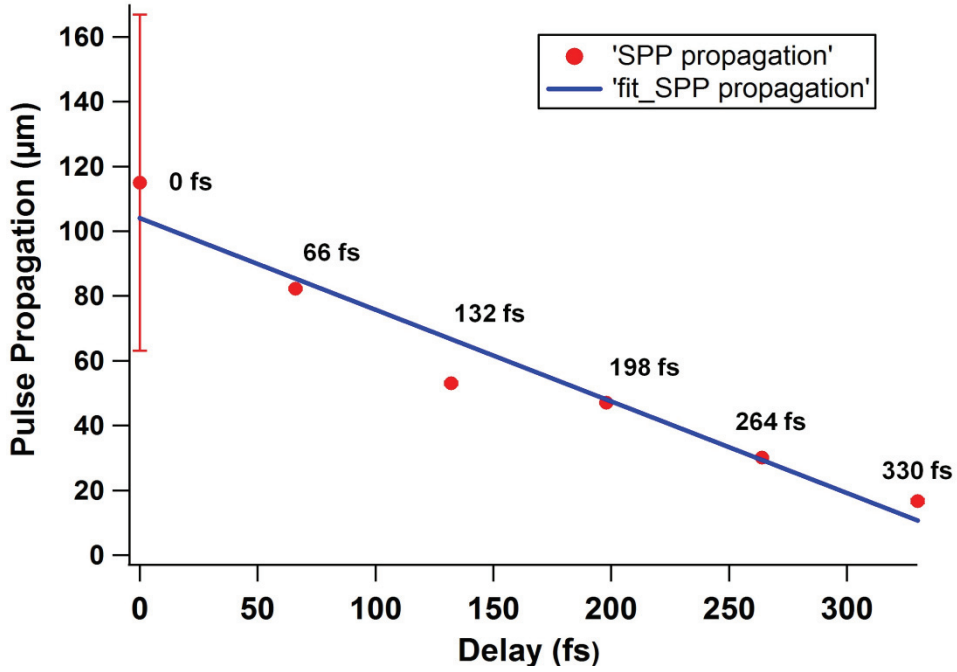

Figure 5.18: SPP pulse position as a function of the position of the delay line (red dots) and the line fit to the data (blue line).

This value shows good agreement with the theoretical value of SPP group velocity for $\lambda_{incident}$=826nm and ε_{gold}(826nm)= -26.2447-i1.6477 (*1*) and using SPP dispersion relation (see eqn (2)).

$$\frac{d\omega}{dk_{SPP}} = \frac{d\omega}{dk_0}\sqrt{\frac{\varepsilon_d + Re(\varepsilon_m)}{\varepsilon_d\, Re(\varepsilon_m)}} \quad (25)$$

Where ε_d=1 and and we get V_{grSPP}=0.94c=2.82 x 10^8 m/s (*78, 79*).

The beauty of the heterodyne detection scheme is allowing us to track phase and time evolution of SPP pulse at the same time. Using Fig. 5.14, which is the combination of amplitude and phase information, we were able to extract

the wavelength of the SPPs and the corresponding phase velocity in the gold extended film.

One column line of the phase data for Fig. 5.14 is taken and plotted along the SPP propagation direction (red line in Fig. 5.19). The fit to the data (black line) gives us the measured SPP wavevector, $k_{SPP\_measured}$= 1.457 ± 0.01 μm^{-1}.

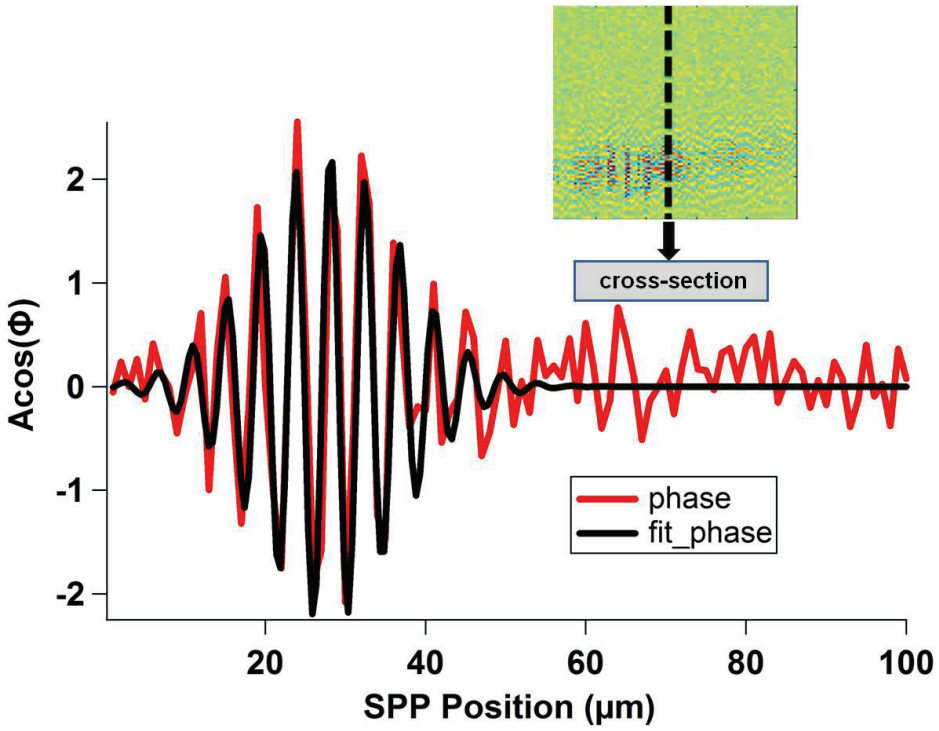

Figure 5.19: Amplitude times the cosine of the phase of SPP pulse for Figure 5.14 (d).

Since SPPs have periodicity around 0.8 μm and the data is taken for every 1 μm, we need to find k_{SPP} using the eqn. (26):

$$\frac{1}{\lambda_{SPP}} - \frac{1}{\lambda_{SPP\_measured}} = \frac{1}{\Delta x} \quad (26)$$

Where Δx is the step between two following data point and in our case it is 1 μm.

Multiplying both side of eqn. (26) gives us the relation between the measured and expected SPP wavevector:

$$k_{SPP} - k_{SPP\_measured} = 2\pi \quad (27)$$

Using $k_{SPP\_measured}$= 1.457 ± 0.01 μm^{-1}, we calculate k_{SPP}= 7.74 ± 0.05 μm^{-1} which corresponds to λ_{SPP} = 812 ± 5 nm. We have extracted the corresponding phase velocity from Fig. 5.19, using eqn. (28):

$$\frac{\omega}{k_{SPP}} = \frac{ck_0}{k_{SPP}} \quad (28)$$

Where c is the speed of light and k_0 is the free space wavevector and for our $\lambda_{incident}$= 826 ± 10 nm laser light, k_0= 7.61 ± 0.09 μm^{-1} is calculated. Finally our measurements show the phase velocity of the central wavelength on thin extended gold film is ~ 2.95 ±0.03 x 10^8 m/s. The calculated theoretical results on thin extended gold film for $\lambda_{incident}$= 826 nm shows the phase velocity V_{phSPP}=0.98c=2.94 x 10^8 m/s (*78, 79*).

Our analysis indicates the good agreement between the measured and calculated phase and group velocity of ultrafast SPP pulses on thin extended gold film.

5.3.2 Metallic SPP Waveguide Characterizations

SPP waveguides are important for plasmonic device applications because of allowing electromagnetic energy transfer from one component to another component in nanometer scale at optical frequencies (*28*). Up to date, mostly

metallic SP waveguides are characterized extensively because of supporting long range SPP modes. That makes them an attractive component for chip-scale data processing technologies (*80*).

We have also done characterizations on metallic SPP waveguide structures (See Fig. 5.7 for topography image and Fig 5.20 for optical image). We have started to SPP waveguide characterizations for ~6 μm wide waveguide width because we were interested in multi mode interference effects. Theoretical studies on SPP waveguides showed that, the number of guided modes in the waveguide is dependent to waveguide lateral width (*81*). According to theoretical predictions for 6 μm waveguide width and the wavelength λ=826 nm, we expect to see two excited modes (multi mode excitation) in the waveguide. Our time integrated SPP waveguide images revealed multi mode excitation clearly in the waveguides (Fig. 5.20 and Fig. 5.21). One main mode at the center and the side modes at the edge of the waveguide are clearly seen.

SPP pulse tracking experiments are also performed on metallic SPP waveguides using our heterodyne fsPSTM microscope. However, having a large spot size (~ 100 μm) in our system due to limited working distance of prism excitation geometry (See Fig. 5.9) has made time-resolved experiments extremely challenging for SPP waveguides. Since the most important step in SPP waveguide studies is to have the light launched at the extended part of the film and outside of the funnels so that the SPP can be excited and guided through the funnels to waveguides. The required spot size to succeed these experiments is ~ 10 or 20 μm. Therefore, we have done time integrated NSOM

characterizations of ultrafast SPPs in metallic waveguides. The best solution to get time-resolved data in our system for SPP waveguides can be using grating coupling instead of prism coupling.

Time integrated SPP waveguide images are taken using the signal arm of the heterodyne fsPSTM system with a chopper which is used to modulate the signal that goes to lock-in amplifier (the reference arm is blocked and AOMs are not used).

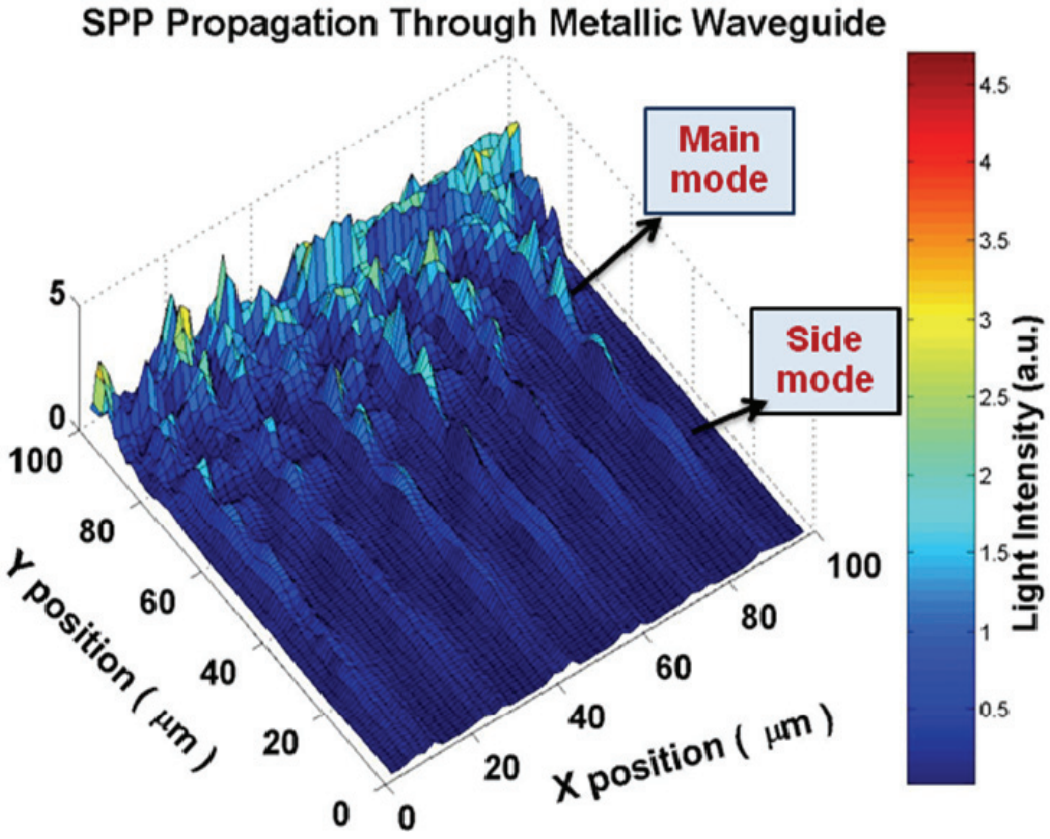

Figure 5.20: 3-dimensional time integrated optical image of metallic (Au) SPP waveguide structures by fsPSTM. The scan range is 100 μm x 100 μm.

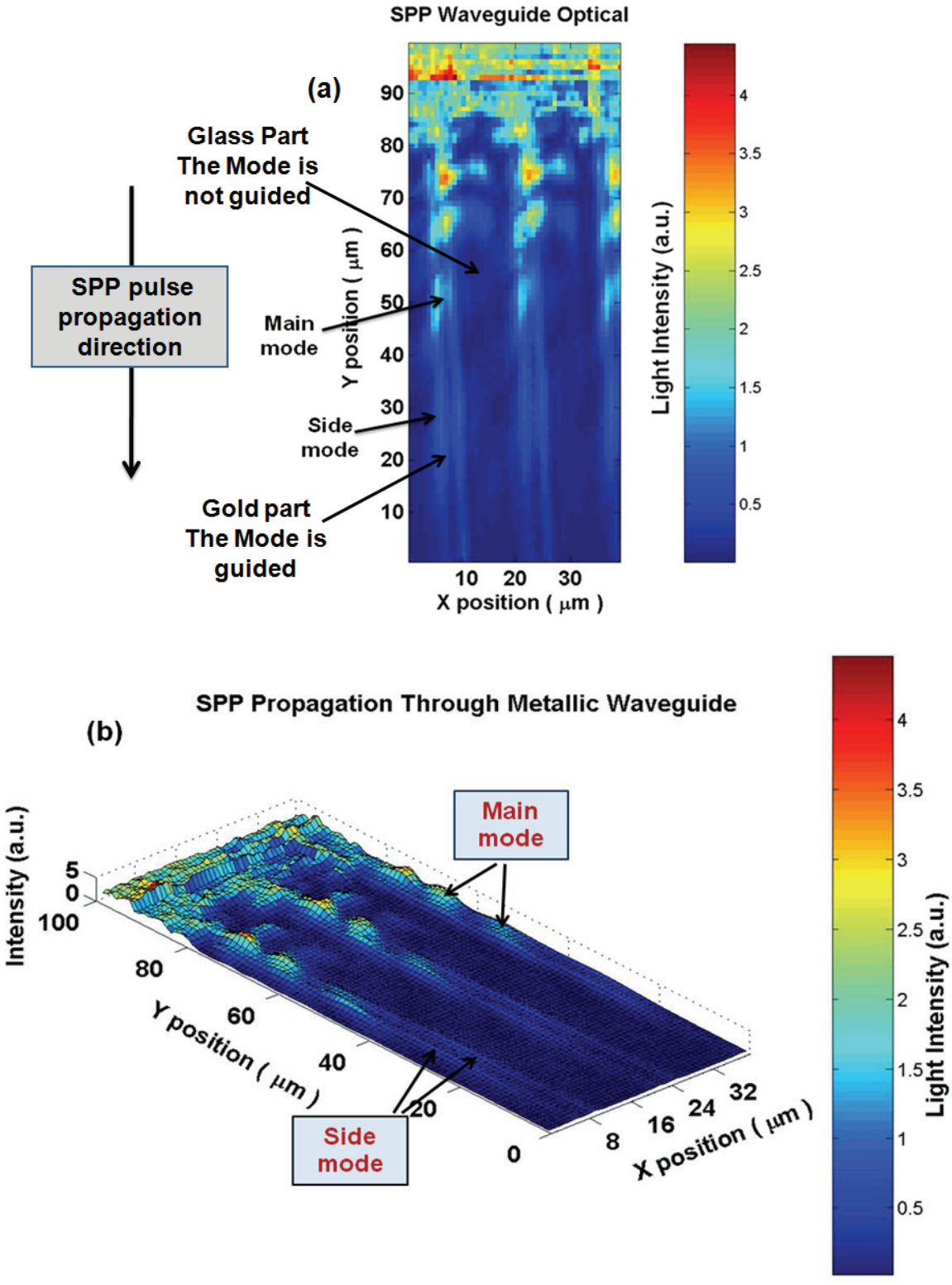

Figure 5.21: (a) Top-view (2-dimensional) and **(b)** 3-dimensional time integrated optical image of metallic (Au) SPP waveguide structures by fsPSTM.

First scans are taken by 100 μm x 100 μm range (see Fig. 5.20). Then the scan range is focused to 40 μm x 100 μm and time-integrated data is recorded (Fig. 5.21 (a) and (b)). To analyze the data, three waveguides in Fig. 5.21 are chosen and column averaged along the SPP propagation direction. The remaining values are plotted with respect to the position along the SPP waveguide (See Fig. 5.22).

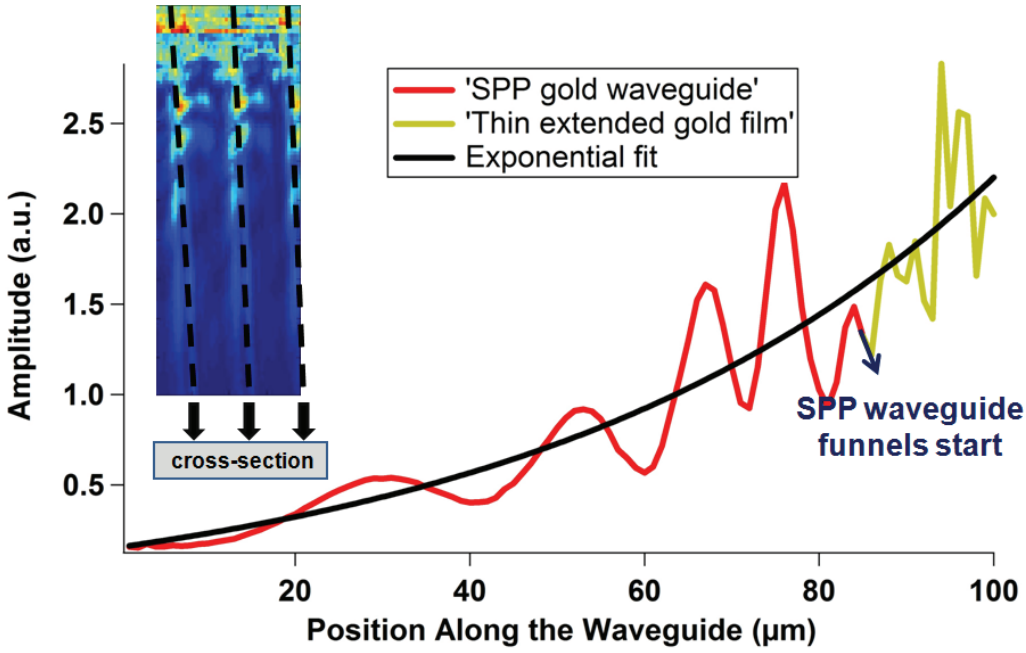

Figure 5.22: Average amplitude of time integrated signal over three waveguides in the Fig. 5.21 (a).

Thin extended gold film which is used to excite SPPs takes place between 84-100 μm in Fig. 5.22. From 84 μm SPP waveguide funnels start where SPP propagates through. SPP is supported at the gold waveguides but not at the glass substrate (Fig. 5.21 (a) and (b)). Decay length of the surface plasmon is defined with the imaginary wavevector of the field and It goes $L=1/2\kappa$ where L is

the decay length of the SPP field and κ is the imaginary wave vector of the surface plasmon when k=k'+iκ (*15*). The exponential plot to Fig. 5.22 gives us the decay length of the SPPs which is ~ 52.63 μm. The decay length calculation is valid for two excited mode interference in the SPP waveguide. The calculated SPP decay length for ~ 826 nm wavelength is ~ 52.58 μm. Our experimental SPP decay length shows good agreement with the theoretical expected values for 826 nm laser light.

5.4 Summary

After building fsPSTM and heterodyne detection system, many topography and optical test scans were performed to calibrate the microscope. Finally, we moved on to time-resolved measurements.

We have shown successful tracking and imaging of 50 fs SPP pulse propagation on thin extended gold film by using home built fsPSTM (Fig. 5.14 and 5.15). The analysis results, performed on time resolved data revealed that SPP pulse envelope propagates with a group velocity ~ 2.831±0.034 x 10^8 m/s (Fig. 5.18) which shows perfect agreement with the theory results of 2.82 x 10^8 m/s for ~ 826 nm incident light. We have also extracted the wavelength of the SPPs ~ 812 nm and the corresponding phase velocity of ~ 2.95 ±0.03 x 10^8 m/s in the gold extended film. The theoretical calculations for ~ 826 nm incident light pointed out the phase velocity V_{phSPP}=0.98c=2.94 x 10^8 m/s. Our group and phase velocity measurements show good agreement with the theoretical results.

We have also done near-field characterizations on SPP gold waveguide structures. Our time integrated images showed harmony with the theoretical predictions about multi mode excitations in SPP waveguides for ~ 6 μm lateral width and $\lambda_{incident}$=826 nm laser excitation.

The analysis on SPP waveguide structures revealed SPP decay length which is ~ 52.63 μm (Fig. 5.22). The calculated theoretical SPP decay length for 826 nm incident light is ~ 52.58 μm. Having a large spot size ~ 100 μm in our set-up, made time resolved experiments on SPP waveguides quite challenging (Fig. 5.8 and Fig. 5.9). Since SPP propagation length is ~ 50 μm, having 100 μm spot makes the experiment especially difficult. The best spot size for SPP time resolved experiments is ~ 10-20 μm so that the light can be launched on the extended gold part to excite the SPPs then, only SPPs are guided through the waveguide.

Our near-field time-averaged and near-field time-resolved experiments show that important insight into dispersion properties of plasmonic devices can be gained.

CONCLUSIONS

In this thesis we have discussed three studies:

1. Understanding Excitation Properties of Ultrafast SPPs (Chapter 2)
2. Understanding Interactions Between Localized and Propagating SPs (Chapter 3)
3. Building a New Form of Near-Field Optical Microscope To Study Propagation Properties of Ultrafast Surface Plasmon Polaritons (Chapter 4-5)

These studies are all important to implement ultrafast SPPs into high speed photonic circuits, time-resolved SPP sensors, and future optoelectronic and telecommunication technologies.

For the excitation studies, we have done characterizations on thin extended metal films by using a sub 25 fs laser pulses from Ti:Sapphire oscillator (KM Labs). SPP excitation is performed with prism coupling technique. We have shown that the excitation of ultrafast SPP is strongly affected by the conventionally used prism coupling technique. This resonant excitation process causes spectral narrowing and phase shift and leads to temporally broadened SPP pulses. Our discussion here is not restricted to the prism coupling technique, but is common to any SPP excitation process that uses resonant coupling between photons and surface plasmons. It has to be noted that both spectral narrowing and spectral phase shifts can, in principle, be compensated. The former effect can be avoided by using an excitation pulse with appropriate angle dispersion, and the latter effect by modulating the phase of the incident

field using pulse shaping techniques. Such techniques have been previously suggested to manipulate plasmon fields in metal nanostructures (*32*).

To understand the interactions between localized and propagating surface plasmons, we have used diblock-copolymer self assembly techniques to deposit long range ordered gold nanoparticles on thin extended silver film. We have reflectivity measurements and extracted surface plasmon dispersion relations for this geometry. Gold nanoparticle arrays revealed substantial increase of the SPP wavevector, indicating strong field localizations. By changing the spacer layer between the gold nanoparticles and silver film, it was also possible to modify the interactions between localized and propagating SPs. These results are promising for future plasmonic device applications.

For the propagation studies of ultrafast SPPs, we have built our own femtosecond photon scanning tunneling microscope (fsPSTM) to visualize ultrafast 50 fs SP pulses in space and time. Incorporating the fsPSTM into a Mach-Zehnder interferometer, allowing heterodyne detection system, we are able to get amplitude information of SPP pulses in space and time.

Despite the beauty of the experiment and the valued information that can be obtained by it, there are only a few time-resolved PSTMs in operation worldwide (*55, 56*). Our fsPSTM and heterodyne detection system is one of a few time-resolved PSTMs that has been built and used in the plasmonics research field to visualize ultrafast surface plasmon pulses in photonic nanostructures. We have performed time resolved experiments on thin extended gold film to track 50 fs SPP pulses in space and time. Our time-resolved results revealed that SPPs

propagate with a group velocity of ~ 2.831±0.034 x 10^8 m/s on gold-air interface (Fig. 5.18). This value shows good agreement with the theoretical value of SPP group velocity V_{grSPP}=0.94c=2.82 x 10^8 m/s. SPP wavelength of ~ 812 nm and the corresponding phase velocity of ~ 2.95 ±0.03 x 10^8 m/s in the gold extended film is extracted using time resolved phase data (Fig. 5.19). The theoretical calculations for ~ 826 nm incident light revealed that the phase velocity should be around V_{phSPP}=0.98c=2.94 x 10^8 m/s. As a conclusion, our group and phase velocity measurements show good agreement with the theoretical results.

We have also performed near-field characterizations on SPP gold waveguide structures. Time averaged experiments on SPP waveguide structures showed harmony with the theoretical predictions about multi mode excitations at 826 nm incident light and for ~6 μm lateral waveguide width.

The calculated SPP decay length (~ 52.63 μm) on SPP waveguide structures also showed excellent agreement with the expected theoretical values (~ 52.2 μm) for ~ 826 nm incident laser excitation.

Our near-field time-averaged and near-field time-resolved experiments show that important insight into dispersion properties of plasmonic devices can be gained.

BIBLIOGRAPHY

1. P. B. Johnson, R. W. Christy, *Physical Review B* **6**, 4370 (1972).

2. M. Paesler, P. Moyer, *Theory, Instrumentation, and Applications (Wiley, New York, 1996)*, 48.

3. M. Ohtsu, K. Kobayashi, T. Kawazoe, *Principles of nanophotonics*. (CRC Press, 2008).

4. *Nanophotonics: Accessibility and Applicability*. (National Research Council, 2008).

5. P. G. Kik, M. L. Brongersma. (Springer, 2007), vol. 131.

6. F. Wooten, *Optical properties of solids*. (Academic Press New York, 1972).

7. H. Raether, *Surface plasmons*. (Springer-Verlag New York, 1988).

8. W. L. Barnes, A. Dereux, T. W. Ebbesen, *Nature* **424**, 824 (Aug, 2003).

9. M. I. Stockman, *Physical Review Letters* **93**, 137404 (2004).

10. S. I. Bozhevolnyi, V. S. Volkov, E. Devaux, J. Y. Laluet, T. W. Ebbesen, *Nature* **440**, 508 (2006).

11. S. I. Bozhevolnyi, J. Erland, K. Leosson, P. M. W. Skovgaard, J. M. Hvam, *Physical Review Letters* **86**, 3008 (2001).

12. S. I. Bozhevolnyi, V. S. Volkov, E. Devaux, T. W. Ebbesen, *Physical Review Letters* **95**, 046802 (2005).

13. H. T. Miyazaki, Y. Kurokawa, *Physical Review Letters* **96**, 97401 (2006).

14. T. Ebbesen, C. Genet, S. Bozhevolnyi, *Physics Today* **61**, 44 (2008).

15. J. Homola, S. S. Yee, G. Gauglitz, *Sensors & Actuators: B. Chemical* **54**, 3 (1999).

16. J. Homola, *Chem. Rev* **108**, 462 (2008).

17. M. Piliarik, H. Vaisocherová, J. Homola, *Biosensors and Bioelectronics* **20**, 2104 (2005).

18. E. J. Sánchez, L. Novotny, X. S. Xie, *Physical Review Letters* **82**, 4014 (1999).

19. H. G. Frey, S. Witt, K. Felderer, R. Guckenberger, *Physical Review Letters* **93**, 200801 (2004).

20. J. M. Gerton, L. A. Wade, G. A. Lessard, Z. Ma, S. R. Quake, *Physical Review Letters* **93**, 180801 (2004).

21. T. Kalkbrenner *et al.*, *Physical Review Letters* **95**, 200801 (2005).

22. L. Novotny, B. Hecht, *Principles of nano-optics*. (Cambridge Univ Pr, 2006).

23. K. Aslan, J. R. Lakowicz, C. D. Geddes, *Current Opinion in Chemical Biology* **9**, 538 (2005).

24. C. Sonnichsen, B. M. Reinhard, J. Liphardt, A. P. Alivisatos, *Nat Biotech* **23**, 741 (2005).

25. N. Khlebtsov, *Quantum Electronics* **38**, 504 (2008).

26. X. Huang, P. Jain, I. El-Sayed, M. El-Sayed, *Lasers in Medical Science* **23**, 217 (2008).

27. S. Yalcin, Y. Wang, M. Achermann, *Applied Physics Letters* **93**, 101103 (2008).

28. R. Zia, J. A. Schuller, A. Chandran, M. L. Brongersma, *Materials Today* **9**, 20 (2006).

29. E. Kretschmann, *Z. Phys.* **241**, 313 (1971).

30. G. P. Wiederrecht, J. E. Hall, A. Bouhelier, *Physical Review Letters* **98**, 83001 (2007).

31. M. Takeda, H. Ina, S. Kobayashi, *J. Opt. Soc. Am* **72**, 156 (1982).

32. M. I. Stockman, S. V. Faleev, D. J. Bergman, *Physical Review Letters* **88**, 67402 (2002).

33. R. P. Van Duyne, *Science* **306**, 985 (2004).

34. J. Grandidier *et al.*, *Nano Lett* **9**, 2935 (2009).

35. M. I. Stockman, *Nat Photon* **2**, 327 (2008).

36. D. J. Bergman, M. I. Stockman, *Physical Review Letters* **90**, 027402 (2003).

37. J. B. Jackson, S. L. Westcott, L. R. Hirsch, J. L. West, N. J. Halas, *Applied Physics Letters* **82**, 257 (2003).

38. V. I. Klimov *et al.* (Science, 2000), vol. 290, pp. 314-317.

39. V. I. Klimov *et al.*, *Nature* **447**, 441 (2007).

40. R. D. Schaller, J. M. Pietryga, V. I. Klimov, *Nano Letters* **7**, 3469 (2007).

41. M. A. Noginov *et al.*, *Nature* **460**, 1110 (2009).

42. J. Seidel, S. Grafström, L. Eng, *Physical Review Letters* **94**, 177401 (2005).

43. P. A. Mistark, S. Park, S. E. Yalcin, et al., M. Achermann, *ACS Nano* **3**, 3987 (2009).

44. S. Park, J. Wang, B. Kim, T. Russell, *Nano Letters* **8**, 1667 (2008).

45. S. Park, B. Kim, J. Wang, T. Russell, *Advanced Materials* **20**, 681 (2008).

46. M. Aizawa, J. Buriak, *Chem. Mater* **19**, 5090 (2007).

47. T. Lohmueller, E. Bock, J. Spatz, *Advanced Materials* **20**, 2297 (2008).

48. M. Möller, J. Spatz, A. Roescher, *Advanced Materials* **8**, 337 (2004).

49. J. Zhang, Y. Gao, R. Alvarez-Puebla, J. Buriak, H. Fenniri, *Advanced Materials* **18**, 3233 (2006).

50. S. Goy-Lopez, E. Castro, P. Taboada, V. Mosquera, *Langmuir: the ACS journal of surfaces and colloids* **24**, 13186 (2008).

51. T. Thurn-Albrecht *et al.*, *Science* **290**, 2126 (December 15, 2000, 2000).

52. T. Choy, *Effective medium theory: principles and applications*. (Oxford University Press, USA, 1999).

53. B. Sareni, L. Krähenbühl, A. Beroual, C. Brosseau, *Journal of Applied Physics* **80**, 1688 (1996).

54. H. van de Hulst, *Light scattering by small particles*. (Wiley New York, 1957).

55. M. L. M. Balistreri, H. Gersen, J. P. Korterik, L. Kuipers, N. F. van Hulst, *Science* **294**, 1080 (November 2, 2001, 2001).

56. M. Sandtke *et al.*, *Review of scientific instruments* **79**, 013704 (2008).

57. A. Zayats, D. Richards, *Nano-optics and Near-field Optical Microscopy*. (Artech House Publishers, 2008).

58. E. Synge, *Philosophical Magazine Series 7* **6**, 356 (1928).

59. D. Pohl, W. Denk, M. Lanz, *Applied Physics Letters* **44**, 651 (1984).

60. A. Lewis, M. Isaacson, A. Harootunian, A. Muray, *Ultramicroscopy* **13**, 227 (1984).

61. M. Achermann, U. Siegner, U. Keller, 2002.

62. M. Ohtsu, H. Hori, *Near-field nano-optics: From Basic Principles to Nano-Fabrication and Nano-Photonics*. (1999).

63. R. C. Reddick, R. J. Warmack, T. L. Ferrell, *Physical Review B* **39**, 767 (1989).

64. D. Brosnan, M. Achermann, *"Photon Scanning Tunneling Microscopy: Instrument, Design, and Development", Capstone Undergraduate Thesis*

65. P. Barbara, D. Adams, D. O'Connor, *Annual Review of Materials Science* **29**, 433 (1999).

66. D. Oullette, M. Achermann, *"Photon Scanning Tunneling Microscopy: Instrument Development", Capstone Undergraduate Thesis*

67. *Mad City Labs., Nano-T 222 Installation and Operation Manual*

68. *National Instruments, PCI-6010 Data Acquisition Card (DAQ) Manual*

69. H. Gersen *et al.*, *Physical Review Letters* **94**, 073903 (2005).

70. H. Gersen *et al.*, *Physical Review Letters* **94**, 123901 (2005).

71. H. Gersen, E. M. H. P. van Dijk, J. P. Korterik, N. F. van Hulst, L. Kuipers, *Physical Review E* **70**, 066609 (2004).

72. L. Gomez *et al.*, *J. Opt. Soc. Am. B* **23**, 823 (2006).

73. J. E. Hall *et al.*, *Opt. Express* **15**, 4098 (2007).

74. R. Fork, O. Martinez, J. Gordon, *Optics letters* **9**, 150 (1984).

75. K. Meyer, M. Achermann, *Setting up the optical part of heterodyne detection system-Independent Study* (2008).

76. M. Abashin, K. Ikeda, R. Saperstein, Y. Fainman, *Optics letters* **34**, 1327 (2009).

77. M. Balistreri, J. Korterik, L. Kuipers, N. Hulst, *Journal of Lightwave Technology* **19**, 1169 (2001).

78. V. Temnov, U. Woggon, J. Dintinger, E. Devaux, T. Ebbesen, *Optics letters* **32**, 1235 (2007).

79. M. Bai *et al.*, *Physical Review B* **69**, 115416 (2004).

80. V. Shalaev, S. Kawata, *Nanophotonics with surface plasmons*. (Elsevier Science Ltd, 2007).

81. R. Zia, M. Selker, M. Brongersma, *Physical Review B* **71**, 165431 (2005).